

**AFRL-IF-RS-TR-2003-78**  
**Final Technical Report**  
**April 2003**



# **MULTI-LAYER WORM DISK WITH PARALLEL RECORDING AND READ-OUT FOR HIGH CAPACITY OPTICAL STORAGE**

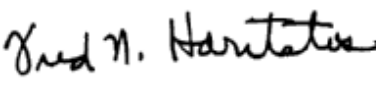
**Call/Recall, Incorporated**


*APPROVED FOR PUBLIC RELEASE; DISTRIBUTION UNLIMITED.*

**AIR FORCE RESEARCH LABORATORY  
INFORMATION DIRECTORATE  
ROME RESEARCH SITE  
ROME, NEW YORK**

This report has been reviewed by the Air Force Research Laboratory, Information Directorate, Public Affairs Office (IFOIPA) and is releasable to the National Technical Information Service (NTIS). At NTIS it will be releasable to the general public, including foreign nations.

AFRL-IF-RS-TR-2003-78 has been reviewed and is approved for publication.

APPROVED:   
FRED N. HARITATOS  
Project Engineer

FOR THE DIRECTOR:   
JOSEPH CAMERA, Chief  
Information & Intelligence Exploitation Division  
Information Directorate

<b>REPORT DOCUMENTATION PAGE</b>			<i>Form Approved</i> <b>OMB No. 074-0188</b>	
Public reporting burden for this collection of information is estimated to average 1 hour per response, including the time for reviewing instructions, searching existing data sources, gathering and maintaining the data needed, and completing and reviewing this collection of information. Send comments regarding this burden estimate or any other aspect of this collection of information, including suggestions for reducing this burden to Washington Headquarters Services, Directorate for Information Operations and Reports, 1215 Jefferson Davis Highway, Suite 1204, Arlington, VA 22202-4302, and to the Office of Management and Budget, Paperwork Reduction Project (0704-0188), Washington, DC 20503				
<b>1. AGENCY USE ONLY (Leave blank)</b>		<b>2. REPORT DATE</b> APRIL 2003	<b>3. REPORT TYPE AND DATES COVERED</b> Final Aug 98 – Jan 03	
<b>4. TITLE AND SUBTITLE</b> MULTI-LAYER WORM DISK WITH PARALLEL RECORDING AND READ-OUT FOR HIGH CAPACITY OPTICAL STORAGE			<b>5. FUNDING NUMBERS</b> C - F30602-98-C-0240 PE - 63726F PR - 2810 TA - 01 WU - 68	
<b>6. AUTHOR(S)</b> D. Dvornikov, E. Walker, P. Rentzepis, and S. Esener				
<b>7. PERFORMING ORGANIZATION NAME(S) AND ADDRESS(ES)</b> Call/Recall, Incorporated 6160 Lusk Boulevard, Suite C206 San Diego California 92121			<b>8. PERFORMING ORGANIZATION REPORT NUMBER</b>	
<b>9. SPONSORING / MONITORING AGENCY NAME(S) AND ADDRESS(ES)</b> Air Force Research Laboratory/IFEB 32 Brooks Road Rome New York 13441-4114			<b>10. SPONSORING / MONITORING AGENCY REPORT NUMBER</b>  AFRL-IF-RS-TR-2003-78	
<b>11. SUPPLEMENTARY NOTES</b>  AFRL Project Engineer: Fred N. Haritatos/IFEB/(315) 330-1638/ Fred.Haritatos@rl.af.mil				
<b>12a. DISTRIBUTION / AVAILABILITY STATEMENT</b> APPROVED FOR PUBLIC RELEASE; DISTRIBUTION UNLIMITED.				<b>12b. DISTRIBUTION CODE</b>
<b>13. ABSTRACT (Maximum 200 Words)</b> Technology has been developed to enable recording and reading of optical disks having many layers. The approach selected relies on recording bits in a volume by using single beam two-photon recording. A volumetric bit is written in the volume of a molded photochromic dispersed organic polymer only at spatial locations where the recording beam has sufficient photon energy. Data recording is based on two-photon absorption, by which one molecule is excited into a higher state by absorbing the combined energy of two photons. Under this program, the following key sub-system components were developed: (a) Materials with high sensitivity and transparency that can be fabricated into a disk form. (b) Recording and read-out heads that are capable of parallel operation while minimizing interlayer cross-talk. (c) Focus and tracking servo systems that position the heads over the desired data track and layer.				
<b>14. SUBJECT TERMS</b> Computer Storage, Optical Memory, Parallel Operation, Photochromic Material			<b>15. NUMBER OF PAGES</b> 81	
			<b>16. PRICE CODE</b>	
<b>17. SECURITY CLASSIFICATION OF REPORT</b>  UNCLASSIFIED	<b>18. SECURITY CLASSIFICATION OF THIS PAGE</b>  UNCLASSIFIED	<b>19. SECURITY CLASSIFICATION OF ABSTRACT</b>  UNCLASSIFIED	<b>20. LIMITATION OF ABSTRACT</b>  UL	

## TABLE OF CONTENTS

<b>1</b>	<b>PROGRAM OBJECTIVES AND SUMMARY OF RESULTS .....</b>	<b>1</b>
1.1	GENERAL CONCEPT .....	1
1.2	SCOPE OF THE PROGRAM: .....	2
1.3	KEY ACCOMPLISHMENTS AND DEMONSTRATIONS: .....	3
<b>2</b>	<b>DETAILED PROGRESS MADE DURING THE PROGRAM.....</b>	<b>5</b>
2.1	STORAGE MEDIA .....	5
2.1.1	<i>Acid generators.....</i>	<i>7</i>
2.1.2	<i>Dye precursor .....</i>	<i>10</i>
2.1.3	<i>Plasticizers.....</i>	<i>11</i>
2.1.4	<i>Background coloration. ....</i>	<i>15</i>
2.1.5	<i>Fatigue.....</i>	<i>18</i>
2.1.6	<i>Writing efficiency.....</i>	<i>20</i>
2.1.7	<i>Fabrication of WORM disks. ....</i>	<i>24</i>
2.1.8	<i>Optical quality .....</i>	<i>27</i>
2.1.9	<i>Temperature stability.....</i>	<i>28</i>
2.2	RECORDING OPTICS.....	30
2.2.1	<i>Analysis Model for Recording Speed and Experimental Validation .....</i>	<i>31</i>
2.2.2	<i>Disk test-stand .....</i>	<i>33</i>
2.2.3	<i>Spherical aberration compensation.....</i>	<i>34</i>
2.2.4	<i>Recording experiment .....</i>	<i>38</i>
2.2.5	<i>Recording laser power dependence on NA .....</i>	<i>44</i>
2.2.6	<i>Fluorescence collection efficiency .....</i>	<i>45</i>
2.2.7	<i>Data formatting, readout and signal processing .....</i>	<i>46</i>
2.2.8	<i>System integration .....</i>	<i>47</i>
2.3	READOUT OPTICS .....	48
2.3.1	<i>Numerical aperture tradeoffs.....</i>	<i>49</i>
2.3.2	<i>Linear spot array illumination and experiments.....</i>	<i>50</i>
2.3.3	<i>In-plane parallel readout experiment .....</i>	<i>52</i>
2.4	SERVO .....	54
2.4.1	<i>Outline of problem.....</i>	<i>54</i>
2.4.2	<i>Review of relevant servo techniques .....</i>	<i>55</i>
2.4.3	<i>Servo error signal generation for 2-photon recorded monolithic multilayer optical data storage .....</i>	<i>57</i>
2.4.4	<i>Spindle rotation speed .....</i>	<i>64</i>
2.4.5	<i>Readout addressing system.....</i>	<i>65</i>
2.4.6	<i>Spindle Selection.....</i>	<i>65</i>
2.4.7	<i>Servo while writing architecture.....</i>	<i>66</i>
<b>3</b>	<b>WORM DEMONSTRATOR .....</b>	<b>67</b>
3.1	WORM PORTABLE READOUT SYSTEM .....	67
3.1.1	<i>Optical system.....</i>	<i>67</i>
3.1.2	<i>Disk format .....</i>	<i>70</i>
3.1.3	<i>Spindle and seek control.....</i>	<i>70</i>
3.1.4	<i>Read channel signal processing.....</i>	<i>71</i>
3.1.5	<i>Lessons learned .....</i>	<i>72</i>
	<i>References .....</i>	<i>72</i>

## LIST OF FIGURES

<i>Figure 1.1.1(a) Two-photon WORM media recording and readout, (b) absorption spectra of the unwritten and written forms of the material and the fluorescence spectrum of the excited written form.</i>	1
<i>Figure 2.1.1 Absorption spectra of onium salts.</i>	7
<i>Figure 2.1.2 Absorption spectra and extinction coefficients of original and modified onium salt.</i>	9
<i>Figure 2.1.3 Absorption spectrum of the WORM material written form.</i>	10
<i>Figure 2.1.4 Written form accumulation kinetics.</i>	11
<i>Figure 2.1.5 Written form accumulation in a) original; b) plasticized material.</i>	13
<i>Figure 2.1.6 Effect of DBP plasticizer concentration on molding temperature.</i>	14
<i>Figure 2.1.7 Effect of plasticizer on writing efficiency: 1 - ethylacetoacetate, 2 – tetrahydrofurfuryl alcohol, 3 – methyl pyrrolidinone.</i>	15
<i>Figure 2.1.8 Dependence of optical density on molding temperature for nonplasticized (●) and plasticized (■) by 10% PC materials. OD after polymerization=0.113 cm<sup>-1</sup> and 0.169 for nonplasticized and plasticized materials respectively, pressure = 3800 lbs/in<sup>2</sup>, dwell time = 5 min.</i>	16
<i>Figure 2.1.9 Dependence of optical density on molding temperature for WORM material prepared with 5% DBP. The optical density before molding was 0.067 cm<sup>-1</sup>.</i>	17
<i>Figure 2.1.10 Dependence of optical density on molding temperature for WORM material prepared with 10% DBP. The optical density before molding was 0.101 cm<sup>-1</sup>.</i>	18
<i>Figure 2.1.11 OD vs. time at 20°C and 95% rel.humidity for RBb containing WORM disk.</i>	18
<i>Figure 2.1.12 OD vs. time at 20°C and 95% rel.humidity for RDP containing WORM disk.</i>	18
<i>Figure 2.1.13 Written form fatigue measurements for: a) RWORM; and b) GWORM materials.</i>	20
<i>Figure 2.1.14 Experimental system for damage threshold and writing intensity.</i>	21
<i>Figure 2.1.15 Written form fluorescence intensity vs. writing light intensity: a) GWORM; b) RWORM. Information written by 527 nm light.</i>	22
<i>Figure 2.1.16 Written plane fluorescence intensity vs. writing time</i>	23
<i>Figure 2.1.17 Writing efficiency measurements: a – original material; b – modified material.</i>	24
<i>Figure 2.1.18 Fatigue measurements: a – original material; b – modified material.</i>	24
<i>Figure 2.1.19 Writing efficiency of original and modified WORM materials.</i>	25
<i>Figure 2.1.20 Written form accumulation kinetics: a – without plasticizer; b- 10% plasticizer.</i>	26
<i>Figure 2.1.21 Sensitivity (a) and fatigue (b) measurements for WORM and WORM3x</i>	26
<i>Figure 2.1.22 Polymerization cell with teflon spacer (left) and 3.5" WORM disks (right).</i>	27
<i>Figure 2.1.23 Comparison of polished and molded surfaces.</i>	27
<i>Figure 2.1.24 Interferogram of a)3.5" mold; b)molded 3.5" disk; c) commercial optical CD.</i>	28
<i>Figure 2.1.25. Temperature stability of various plasticizers and their effect on background coloration of the molded disks: 1 – methyl-cyanoacetate; 2 – sulfolane; 3- ethyl-acetoacetate.</i>	29
<i>Figure 2.1.26. Effect of temperature on dye precursor write-read form transformation ability.</i>	30
<i>Figure 2.2.1 The two-photon recording analysis model.</i>	31
<i>Figure 2.2.2 Fluorescent confocal microscope image of data tracks recorded at different speeds with 2x2um<sup>2</sup> fluorescence bits.</i>	33
<i>Figure 2.2.3 Single-beam two-photon recording system diagram</i>	34

Figure 2.2.4 Optical system layout for two-photon recording and readout using a Keplerian conjugate compensation system to offset the spherical aberration introduced by the disk during layer addressing having layer separation $\Delta t$ .....	35
Figure 2.2.5 Video microscope images and ccd profiles of the focused spot through a) 1mm of material, b) 2mm of material, c) 3mm of material, and d) 4mm of material.....	37
Figure 2.2.6 compact compensation system, using 0.5NA optics.....	38
Figure 2.2.7. (a) physical optics simulation of 0.5NA axial PSF Irradiance <sup>2</sup> : 460nm@ 0.5NA, bit size: 0.6*0.6*6 $\mu$ m <sup>3</sup> ; (b) Recorded bit: 460nm@ 0.5NA, bit size: 0.6*0.6*6.5 $\mu$ m <sup>3</sup> ; (c) Recorded bit: 532nm@0.5NA, bit size: 0.7*0.7*7 $\mu$ m <sup>3</sup> ; (d) Recorded bit: 532nm@0.75NA, bit size: 0.5*0.5*4.5 $\mu$ m <sup>3</sup> wavelength blue laser is also ~10 times more sensitive than the 532nm green laser based on the absorption spectra of the unwritten form. However, for all upcoming system demonstrations the 532nm recording laser will be used as it has sufficient power to be able to record at 1Mb/s.....	40
Figure 2.2.8. Blue(460nm) laser multi-layer recording.....	41
Figure 2.2.9.(a) Simulation of the tracks cross talk: recording $\lambda$ =532nm, NA=0.5; readout $\lambda$ =635nm, NA=0.5; (b) Experimental result.....	42
Figure 2.2.10. (a) Layer separation vs. NA (b) Experiment result.....	42
Figure 2.2.11. Capacity vs. NA.....	43
Figure 2.2.12. Normalized recording power vs. NA.....	44
Figure 2.2.13 Fluorescence collection.....	45
Figure 2.2.14 The readout channel function diagram.....	46
Figure 2.2.15. CNR and BER measurement results.....	47
Figure 2.2.16. Block diagram of WORM system.....	47
Figure 2.3.1 Zemax layout of experimental linear spot array illumination system.....	50
Figure 2.3.2. Illumination spots at different diffraction orders.....	51
Figure 2.3.3. Readout signals at different diffraction orders.....	51
Figure 2.3.4(a) Schematic drawing of in-plane parallel illumination showing experimental CCD image of 1 x 16 illumination spot array (b) a parallel readout system based on in-plane illumination and a PMT array.....	52
Figure 2.3.5(a) In-plane illumination module and (b) its schematic drawing.....	53
Figure 2.3.6. (a) 1x 16 fluorescent spot array at the detector plane as imaged by a CCD camera (b) 4 typical signal outputs from the 1 x 16 pmt detector array.....	53
Figure 2.4.1 Optical system showing the objective lens collecting the light and lens focusing to a segmented detector(typically a quadrant detector) that provides signals that may be algebraically combined to form an error signal for controlling the position of the objective lens.....	55
Figure 2.4.2 Outline of astigmatic focus and push-pull tracking. The light distribution on the quad detector is shown when the lens is in focus and on either side of focus. The focus error signal (FES) is obtained by subtracting the diagonal sums and the tracking error signal (TES) is obtained by subtracting the left and right halves.....	56
Figure 2.4.3. Outline of wax-wane focus and push-pull tracking. The light distribution on the quad detector is shown when the lens is in focus and on either side of focus. The focus error	

signal (FES) is obtained by subtracting the upper and lower halves and the tracking error signal (TES) is obtained by subtracting the left and right halves.....	56
Figure 2.4.4. Two-Photon-recorded monolithic multilayer disk concept.....	57
Figure 2.4.5 Outline of push-pull (out-rigger) focus and push-pull tracking error signal generation. Fluorescent light distribution on two detectors shown when lens in focus and on either side of focus. Focus error signal (FES) obtained by subtracting two individual detector signals, tracking error signal (TES) obtained by subtracting left and right halves of bi-cell detector. ....	58
Figure 2.4.6. Block diagram of the closed-loop focus servo system.....	59
Figure 2.4.7. Typical lead-lag circuit used for phase shift at crossover point.....	60
Figure 2.4.8 Experimental system for testing push-pull focus and push-pull tracking with collinear illumination.....	61
Figure 2.4.9 (a) Experimental focus error signal (FES) using collinear illumination, (b) Experimental tracking error signal (TES) using collinear illumination. ....	62
Figure 2.4.10. Carrier-to-noise-ratio (CNR) of about 35dB from a single tone data track with bit dimensions $1.5\mu\text{m}(\text{radial}) \times 1.5\mu\text{m}(\text{in track}) \times 15\mu\text{m}(\text{in depth})$ with both tracking and focus servo loops closed, and the electronic noise floor of the transimpedance amplifier/detector combination with no light incident upon the detector. ....	62
Figure 2.4.11. Experimental system for testing push-pull focus and push-pull tracking. ....	63
Figure 2.4.12. Experimentally obtained tracking servo loop limit. Below the line the tracking loop can close successfully and follow a track with a given eccentricity and spindle speed. Above the line the tracking loop cannot be closed. ....	64
Figure 2.4.13. Top view of disk showing servo tracks and write and read lasers separated radially by one track pitch. ....	66
Figure 3.1.1 Fully assembled system with laptop computer interface. ....	67
Figure 3.1.2 Photograph of the optical bench with illumination and readout paths. ....	68
Figure 3.1.3(a) Schematic drawing of in-plane parallel illumination showing experimental CCD image of $1 \times 16$ illumination spot array (b) schematic of experimental system of Figure 3.1.2 parallel readout system based on in-plane illumination and a PMT array.....	69
Figure 3.1.4 (a) In-plane illumination module and (b) its schematic drawing .....	69
Figure 3.1.5 Flowchart of data formatting during recording. ....	70
Figure 3.1.6. Flowchart of data formatting during readout.....	70
Figure 3.1.7. confocal microscope images (a) shows 3 groups of 16 data tracks where each group of sixteen contains one of the jpeg images to be displayed, (b) shows the effect of a surface defect on the disk (such as a scratch) and the resultant loss of data.....	71

## LIST OF TABLES

<i>Table 1 Plasticizers for WORM materials.</i>	<i>12</i>
<i>Table 2. Effect of plasticizer.</i>	<i>19</i>
<i>Table 3: Table of material thickness and knife-edge measurements of <math>1/e^2</math> spot size diameters as measured with the BeamMap® spot scanner.</i>	<i>36</i>
<i>Table 4: Material thickness and readout signal levels with and without spherical aberration correction.</i>	<i>37</i>
<i>Table 5</i>	<i>50</i>
<i>Table 6. Channel numbers achieved with different system parameters.</i>	<i>51</i>



# 1 PROGRAM OBJECTIVES AND SUMMARY OF RESULTS

## 1.1 General Concept

Call/Recall is developing a technology to enable the recording and reading of disks having many layers. The approach used by C/R relies on recording bits in a volume by using single beam two-photon recording.<sup>1</sup> A volumetric bit is written in the volume of a molded photochromic dispersed organic polymer only at spatial locations where the recording beam has sufficient photon energy. Two-photon recording is based on two-photon absorption, by which one molecule is excited into a higher state by absorbing the combined energy of two photons as shown in Figure 1.1.1(a). The two photons can be at different wavelengths, suitable for two-beam recording method, or at the same wavelength using single-beam recording as implemented in this program. The excited molecule combines with another type of dye molecule to become a new stable written form, which emits broadband fluorescence when excited with the readout laser beam as shown in Figure 1.1.1 (b). Figure 1.1.1 (b) shows typical absorption spectra of the unwritten and written forms of the material. The written form of the material has an absorption band created in the wavelength region of red laser diodes such as 635nm edge emitting laser diodes.

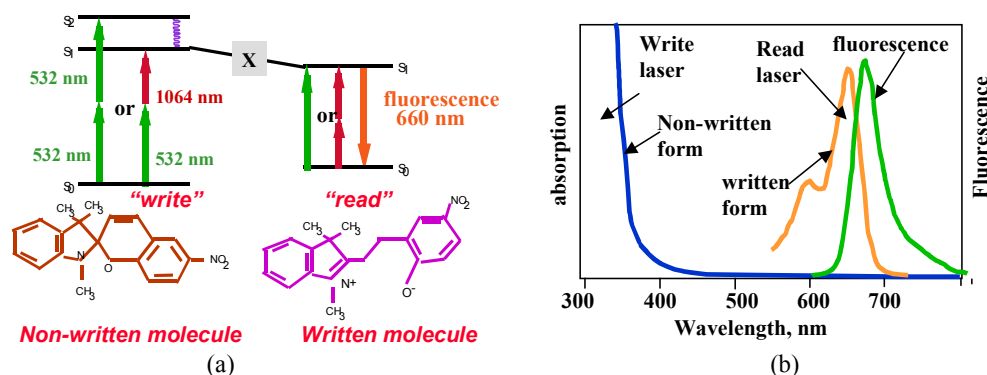


Figure 1.1.1(a) Two-photon WORM media recording and readout, (b) absorption spectra of the unwritten and written forms of the material and the fluorescence spectrum of the excited written form.

The recorded bits are read by fluorescence that is excited by single-photon absorption of the read laser within the written spot volume. Using this method, C/R has previously demonstrated multiple digital jpeg image storage in a mini-disk-ROM configuration with a portable readout unit. The results indicated small crosstalk between layers and excellent stability of the written bits at room temperature. The recorded photochromic data layers are non-reflective and can be recorded very closely together. The approach promises low-cost, high-volumetric-density WORM disk media with hundreds of layers for data storage, and low-cost compact disk player drives employing semiconductor red lasers.

## 1.2 Scope of the program:

The objective of this program was to develop the key sub-system components of a volumetric WORM disk recording system enabled by two photon absorption for recording and fluorescence of recorded bits for readout. Key enabling components of such a system include:

- 1) materials with high sensitivity and transparency even after hundreds of layer recording that can be easily fabricated in disk shape;
- 2) recording and read-out heads that are capable of recording and reading out in parallel to and from an arbitrary layer while minimizing interlayer cross-talk; and
- 3) focus and tracking servo systems that are necessary to position the heads over the desired data track and layer and to compensate for the disk movements.

Several novel approaches needed to be developed and integrated to realize the demonstration of a functional multi-layer WORM system capable of

- 1) 9 GB WORM disk capacity with a stretch goal of 20GB;
- 2) 1Mb/s recording and
- 3) 10 Mb/s read-out rates by addressing 10 to 20 bits simultaneously.

To reach these goals the recording medium must have high 2-photon absorption cross-section for efficient recording of the data. To achieve fast recording rates, given the 2-photon absorption cross-section, the pulse repetition rate and the intensity of the recording laser must be sufficiently large. Alternatively a lower repetition rate laser with significantly higher intensity can be considered together with a light modulator array to perform parallel recording. In order to achieve small bit sizes and therefore high capacity, the recording system needs to be capable of delivering and focusing short pulses at the desired layer and locations inside the storage medium. Thus the 2-photon medium should allow the recording of hundreds of layers of data without losing transparency and without increased cross-talk. The read-out system needs to provide efficient detection of the emitted fluorescence from recorded spots, at the desired layer with a minimum interlayer cross-talk. Since the fluorescence per recorded bit is typically weak, a parallel readout system is needed to boost the aggregate data rates to the desired levels. For robust and reliable recording and read-out from a rotating disk, parallel tracking and focus servo systems need to be integrated with the recording and read-out heads to eliminate the effects of disk run-off and wobble.

The scope of the program was therefore the development and demonstration of four key sub-systems for the realization of two-photon absorption based WORM disk storage systems:

- 1) Development of large diameter disk media with optimized WORM materials
- 2) Development of suitable recording optical head
- 3) Development of a suitable Parallel read-out head
- 4) Development of Focusing and tracking servo system

- 5) To establish a benchmark the ultimate goal was set to be the demonstration of the operation of a WORM disk system prototype. To this end, the media and read-out heads, and tracking/focus servo needed to be integrated in a compact package to form a WORM readout prototype that could be easily interfaced with a table top recording prototype.

### 1.3 Key accomplishments and demonstrations:

**Media related accomplishments:** A means for the synthesis of a dye precursor and advanced acid generator that enables fabrication of high sensitivity WORM optical disks has been developed. Fabrication 3.5inch diameter WORM media have been shown. The new media exhibit higher sensitivity and significantly better stability than previous materials. The thermal stability of the WORM material components and the effect of various additives on the photochemical and optical properties of the fabricated WORM disks were evaluated. In summary, during the course of this program we have demonstrated

- 3X Higher writing efficiency
- 10X Lower background noise
- 3X Higher readout fatigue resistance
- Higher temperature stability

**Recording system related accomplishments:** A recording speed model has been developed and experimentally verified. Recording experiments to examine bit size have been performed, and compared to simulation. Influence of numerical aperture (NA) on system performance has been analyzed. Theoretical analysis of recorded bit size and cross-talk has been performed and experimentally verified. This analysis has been further extended to include data storage capacity. Our results indicate that by controlling the cross talk between tracks and layers, the capacity of a 5.25" diameter 3mm thick disk can be 140GB for 532nm at 0.5NA, however for the 3.5" diameter disks that are being fabricated the total possible capacity is 22GB. For larger NA and blue recording the capacity can be made to exceed a terabyte per disk.

A survey of existing laser systems has been conducted and it was found that for the WORM demonstrator a serial recorder that used 532 nm wavelength short pulse (6ps) fast repetition rate (75MHz) laser would be most optimal to satisfy the program requirements given the media characteristics. Such a recording system was built around a HighQ brand laser system where 1Mb/s recording data rate has been demonstrated using 1.5W of average power or equivalently ~10KW of peak power with the pulse width and repetition rate characteristics of the HighQ laser system just described. We have also used a blue laser, using a frequency doubled (MIRA Ti:Sapphire laser system at 460nm wavelength, 200fs pulsewidth, and 76MHz repetition rate) to take advantage of the higher sensitivity of our media in the blue.

In summary during the course of this program we have demonstrated the recording of 3 dimensional bits having a 1.2um diameter by 15um bits recorded at a bit rate of 1Mb/s with a

green laser with 1.5W average power having a peak power of 10kW with a rep rate of 75KHz and pulse width of 6ps. Also recorded were 0.7um diameter by 10um bits using a blue laser at an average power of 5mW and a rep rate of 76MHz and a pulse width of 200fs (at a recording data rate of 1bit/s due to lack of laser power at this wavelength).

**Readout system related accomplishments:**

- Typically a 1.2um diameter, 15um thick bit provides ~nW fluorescence power delivered to the detector when radiated by 200μW of illumination power. The fluorescent signal readout requires high sensitivity detectors such as standard Hamamatsu photomultiplier tubes. Readout signal quality is acceptable for channel speeds at ~1Mb/Sec/channel.

We have also used an FPGA encoding/decoding system for 16channel readout employing 2,7 encoding/decoding with 8,15 ECC to alleviate the effects of media defects and channel SNR.

- Track and layer crosstalk for given layer and track pitch have been shown to be < 30db.
- Serial Channel readout speeds of 2Mb/Sec have been demonstrated

In addition, closed-loop focus and tracking control using fluorescent signal power has been demonstrated on 2-photon recorded data tracks. A standard CD voice-coil actuator follows a fluorescent track. The disk does not need to be preformatted or the data layers do not need any special groove structures.

**Demonstrator accomplishments:** An integrated 16-channel readout and recording system together with FPGA based signal-processing unit was demonstrated. The system is a table demo capable of a 1Mb/s recording rate and a 16Mb/s readout rate. An experimental evaluation of a 1 x 16 parallel readout system is demonstrated. On a 3.5” diameter disk that is 5mm disk, we have demonstrated the feasibility of a total storage capacity of 22GB/disk.

**LESSONS LEARNED**

- 1) At 1Mb/s the recording speed is still too slow due to suitable laser availability and the two-photon absorption cross-section.
- 2) Media defects need to be improved in order to increase reliability. Also a new media needs to be developed that is suitable for mass manufacture capability that can withstand the injection molding environment.
- 3) Using a faster layer and track addressing stage controller we could make layer and radial addressing faster. Integrating the focus/tracking servo into all table-top demos would also allow faster access time along with improved stage motor controller and improved system reliability.
- 4) There is significant more room to increase the readout speed by using more data channels.

## 2 DETAILED PROGRESS MADE DURING THE PROGRAM

---

### 2.1 Storage Media

To realize a high density multi-layer WORM system the recording media must have high 2-photon absorption sensitivity to achieve efficient recording of the data, so that the data can be written in real-time and by compact light sources. In addition, to extend to the third dimension, the recording disks must be much thicker than today's disks, e.g. 5-10 mm compared to 1.2 mm, while maintaining very good uniformity and homogeneity to allow the recording of hundreds of layers of data without losing transparency and without increasing cross-talk. These materials also should have fluorescence efficiencies of  $> 80\%$  to achieve high readout signal levels. To be suitable for utilizing in practical memory devices, it is important that such memory materials will be thermally stable between  $+55$  and  $-55$  deg. C and will have photostability to perform at least  $10^6$  read-out cycles.

The two photon material that was studied and developed for this project is composed of light sensitive photochromic molecules homogeneously dispersed in rigid polymer hosts. Photochromic molecules are capable of changing their chemical structure when illuminated with light and this structure change results in changing the spectroscopic properties of the new form of the material, including the absorption and emission spectra. The difference in the absorption and emission properties of the non-irradiated and irradiated areas, thus, can be used to store, optically information. The two forms of the material, the original, write, and photo induced, read forms will represent 0 and 1 in a binary code, respectively. The write form of the memory material usually has its long wavelength absorption band in the UV, while the absorption spectrum of the read form is red shifted to the visible region. The read form should emit strong fluorescence, when excited. Access, of the stored information in this case, may be achieved by the detection of the fluorescence emitted by the written bits and processed as 1 in the binary code. The reading light wavelength must correspond to the absorption of the written form.

This electronic transition may be achieved by one or multiphoton process. A one photon process will result, preferentially, in the excitation of the molecules residing on the surface of the device. Multiphoton process will promote excitation preferentially in the volume where the two beams overlap. Two photon process is used because its transition probability is 20-30 orders,  $10^{20}$  to  $10^{30}$ , higher than a three photon process.

The advantages of the two-photon absorption process are based upon its ability to excite selectively molecules inside a volume without populating molecules on the surface of the device. This, may be achieved because the wavelength of each beam is longer, has less energy, than the energy gap between the ground state and first allowed electronic level. Therefore it propagates through the medium without being absorbed by a one-photon process. However, if two beams are used for excitation and the energy sum of the two interacting photons is equal to or larger than the energy between the ground and first excited state ( $S_0 \rightarrow S_1$ ) absorption will occur. It is also important to note that there is no real level at the wavelength of either beam, therefore neither beam can be absorbed alone by a one-photon mechanism. When the two photons collide

within the volume, absorption occurs only within the volume of interaction and the size of the written bit is defined by the width of the two beams.

The transition probability of a two-photon absorption process, among other parameters, depends upon the product of the two writing beam intensities. Therefore it is important to utilize lasers emitting high intensity light i.e. picosecond and subpicosecond pulses.

In order to be able to use low intensity/energy compact, high repetition rate pulsed lasers for recording, WORM materials should have high recording efficiency and possess following characteristics.

The original, write form, should:

- 1) have high two-photon absorption cross-section;
- 2) do not fluoresce;
- 3) absorb in an easily accessible wavelength;
- 4) have high conversion quantum yield to the read form;
- 5) have high rate for conversion to read form;
- 6) be stable between  $-55^{\circ}\text{C}$  to  $55^{\circ}\text{C}$ .

The read form should:

- 1) absorb frequencies of available lasers;
- 2) have high one photon cross-section;
- 3) fluoresce with high quantum efficiency;
- 4) be stable between  $-55^{\circ}\text{C}$  to  $55^{\circ}\text{C}$ ;
- 5) fluoresce in region where solid state detectors are commercially available;
- 6) have emission lifetime in the nsec range;
- 7) be capable of more than  $10^6$  reading cycles (100  $\mu\text{sec}$ /cycle illumination) in with less than 15% decrease in intensity.

These materials should also enable the placement of special tracking and focus servo signal marks by pre-formatting. To achieve such a WORM material we successfully realized the following approaches in the development of materials:

- 1) The required recording efficiency was achieved by the use of more sensitive acid generators, capable of producing stronger acids. We have developed and synthesized effective acid photo-generators based on onium salts, which dissociate with formation of strong inorganic acid. The photo-dissociation efficiency was found very high, 70%. The kinetics and mechanism of the writing process were studied. It was found that strong acids also react faster with the dye precursor, resulting in a high rate of written form production.
- 2) The recording process was accelerated by modification of the polymer matrix and increasing the rate of diffusion controlled reactions.

- 3) We designed and synthesized the novel dye precursor, which is capable of producing stable, highly fluorescent dye with absorption maximum at 650 nm. This dye precursor was successfully utilized in fabrication of WORM materials.
- 4) The memory materials were embedded in a polymer host which can be shaped to any size disk desired with integrated structures for alignment and mounting. We have design and synthesize modified polymer matrices, which accelerate the writing rate and increase the S/N ratio for the reading process of the WORM materials. Polymerization molding, compression molding and polishing have been utilized to produce the desirable optical quality 1" diameter WORM disks and the technique was extended to the successful fabrication of larger diameter, 3.5"x 0.4" disks.

### 2.1.1 Acid generators

To increase the light sensitivity of the 2-photon memory material and make it suitable for WORM applications, we have utilized a new more effective acid photogenerator based on the photodissociation reaction of onium salts. The strong inorganic acid, generated as a result of the photoreaction, rapidly reacts with the dye precursor (DP) to form the colored, written form of the material. Unlike previously utilized NNA materials, which generate relatively weak organic acids, onium salts generate extremely strong acids capable of reacting with the dye precursor almost quantitatively and shift the equilibrium between DP + acid pair and dye molecule completely to the formation of the dye molecule. As a result, utilization of salts allows us to increase significantly the light sensitivity of the memory device because in this case practically each generated molecule of acid will be transferred to a written molecule.

The onium salts utilized as acid generators for WORM media have absorption maximum at the 230 nm region, as shown in Figure 2.1.1. Excitation of these salts by two-photon absorption of 532 nm light corresponds to the single photon absorption at 266 nm, where the absorption crosssection is about 5 times lower than the maximum. We have synthesized several modified molecules, which were designed to increase their absorption at the region of 266 nm.

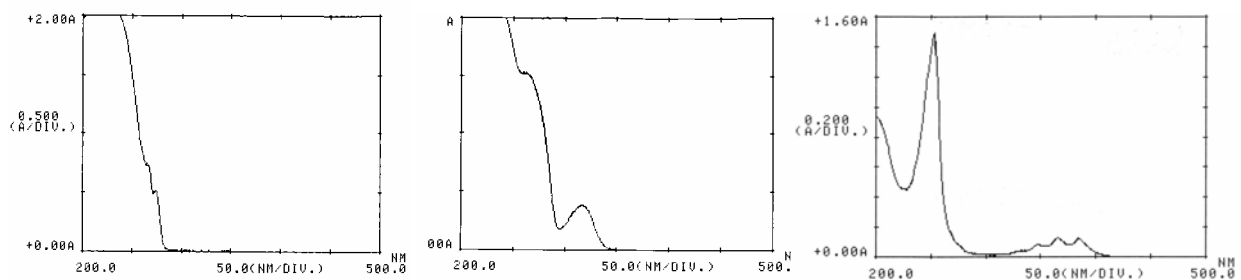
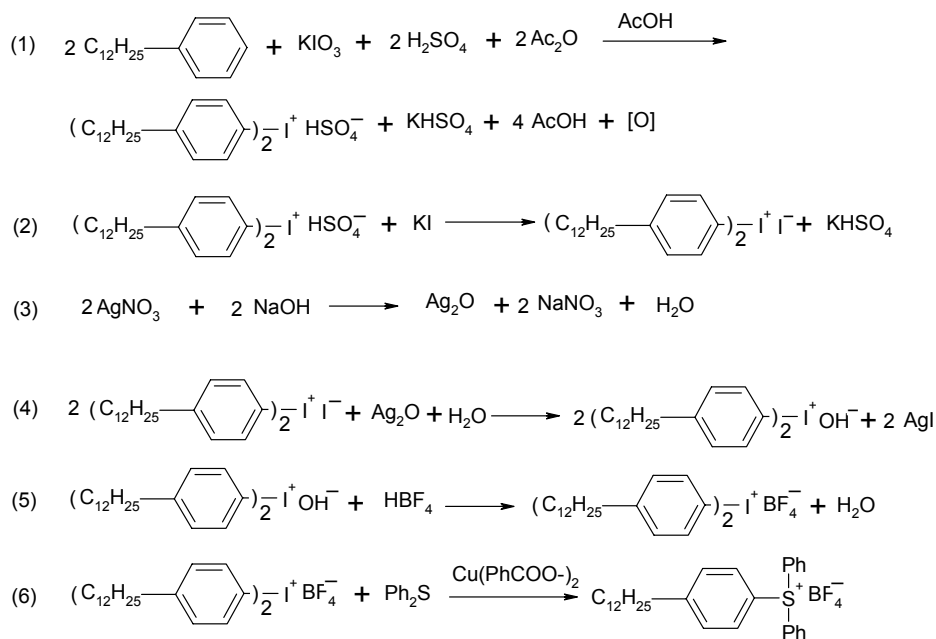


*Figure 2.1.1 Absorption spectra of onium salts.*

Low solubility of onium salts in nonpolar media is the major factor that limits the writing efficiency of the WORM material. To increase the concentration of the salt to the required

level, we had to add 15% of polar plasticizer compound to PMMA matrix. A large amount of plasticizer, however, may affect the mechanical and optical properties of the polymer matrix, such as hardness, scratch resistance and flatness. To eliminate this deficiency, we have synthesized modified salts which have long aliphatic chain attached to the phenyl ring of the molecule. The synthetic steps of this acid generator are shown below:



As we expected, this new acid generator material has superior solubility not only in polar media, but also in nonpolar solvents such as ethylacetate and methyl methacrylate monomer. The solubility of these molecules strongly depends on solution temperature and significantly increases with increase in temperature. We were able to dissolve, at room temperature, in pure methyl methacrylate monomer 30mg/ml of salt and then polymerize this solution to obtain optically clear solid polymer bulk. This is at least an order of magnitude higher in concentration than could be reached with original acid generator material without the use of polar plasticizer. Addition of small amounts of polar plasticizer, such as acetonitrile, and dissolving the salt at higher temperatures allows us to create even higher acid generator concentration.

Figure 2.1.2 shows the absorption spectra of the original and modified molecules in acetonitrile. We have measured the absorption crosssection for these salts. Our data indicate that at 266 nm the modified molecule has two times higher absorption crosssection value than the original one. This means that the writing process for WORM material contained the same concentration of the modified acid generator, therefore it should be two times more efficient than for original WORM material. A better solubility of the modified acid generator allows one



to make WORM materials with this higher concentration, which, in turn, will increase proportionally the writing efficiency of the media.

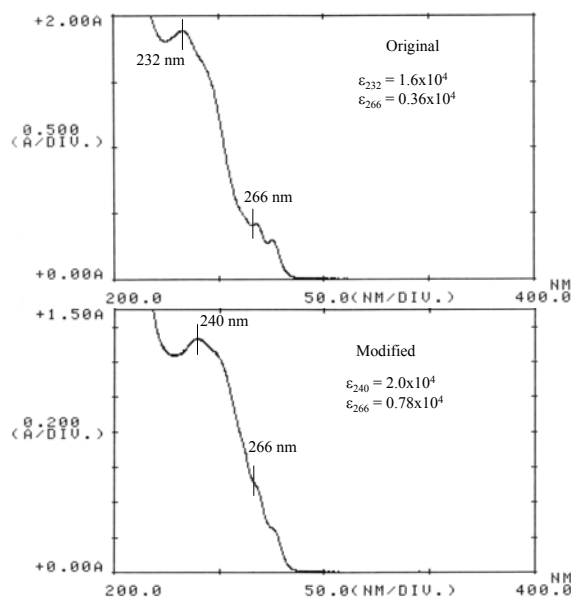


*Figure 2.1.2 Absorption spectra and extinction coefficients of original and modified onium salt.*

The aliphatic chain attached to the phenyl ring of the molecule significantly increases the solubility of the acid generator, therefore it is possible to disperse this molecules uniformly in a polymethyl methacrylate polymer host at concentrations up to  $7 \times 10^{-2}$  M. The concentration of the plasticizer was only 5% by volume and did not affect optical properties of the fabricated disks. The small amount of plasticizer is instrumental in increasing the concentration of the salt in nonpolar methyl methacrylate monomer, which in pure monomer at room temperature is limited to approximately  $2.5 \times 10^{-2}$  M. This also improves the material writing efficiency by accelerating the diffusion-controlled reaction between the dye precursor and the photogenerated acid molecules.

We have synthesized large quantity, 200g, of the advanced acid generator in order to satisfy the requirements for fabrication of 1" WORM disks and 3.5" disks. The synthesized compound was purified by means of column chromatography, followed by recrystallization from alcohol solutions. The high purity of the acid generator is important issue, because at high concentrations, impurities may also be accumulated at sufficient concentrations to absorb light at critical spectral regions and participate in photoreactions that affect the characteristics of the WORM disks, such as background color, writing efficiency, fatigue resistance and written bit size. The structure and purity of the advanced acid generator was confirmed by means of NMR, MS and UV-VIS spectroscopy.

### 2.1.2 Dye precursor

We have developed and synthesized the dye precursor molecules, which react with photogenerated acid molecules to produce colored written form of the WORM material. This dye precursor was synthesized by reaction of commercially available Rhodamine 700 laser dye with base. The dye precursor is colorless material with absorption spectrum in UV region. The information is written by two-photon excitation of WORM material with 532 nm laser light, which photogenerate acid followed by reaction with dye precursor and formation of strongly fluorescing Rhodamine 700 dye. This dye has its absorption maximum at 650 nm and the written information can be accessed by excitation of the written bits by red diode lasers. The absorption spectrum of the Rhodamine 700 dye is shown in Figure 2.1.3.

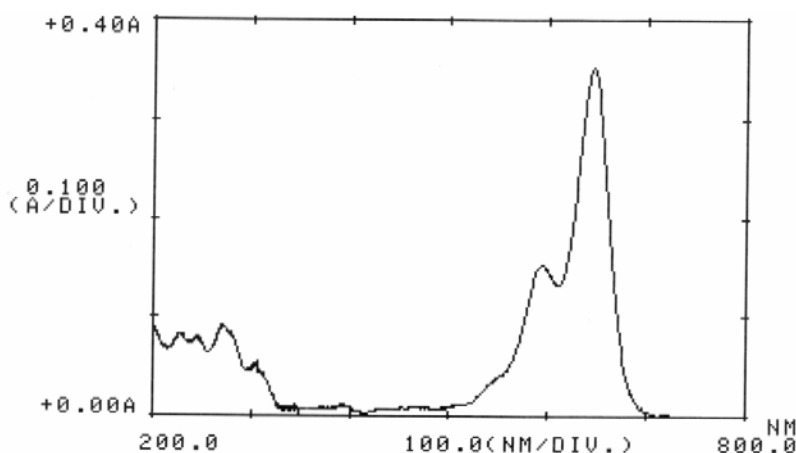


*Figure 2.1.3 Absorption spectrum of the WORM material written form.*

We have synthesized modified dye precursor, which was found possess superior properties compared to original H-substituted molecule. When this modified DP contains a methoxy group instead of the hydrogen atom its thermal stability increases, a low background coloration is observed, and it can be fabricated and purified by simpler methods.

Figure 2.1.4 shows the reaction kinetics of DP acetonitrile solution with the photogenerated acid after excitation with UV light. The accumulation of the written form, which has its absorption maximum at 650 nm, is observed immediately after UV excitation, then the increase in optical density continues for few more minutes until it reaches its maximum.

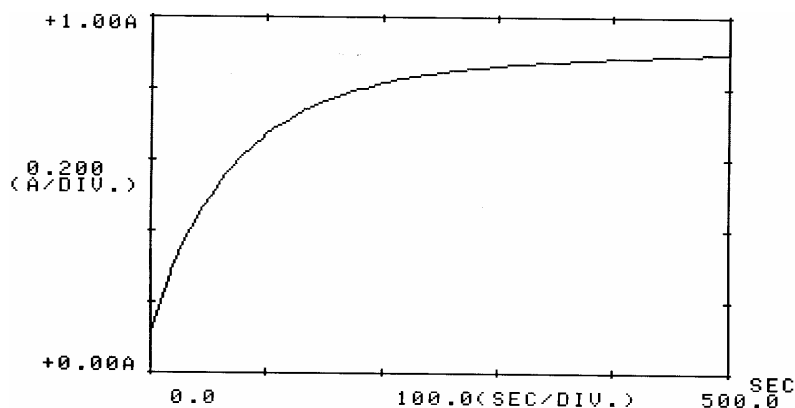


Figure 2.1.4 Written form accumulation kinetics.

### 2.1.3 Plasticizers

Our data showed that plasticizers embedded in polymer matrix may dramatically improve the WORM material characteristics, such as write/read efficiency, background coloration, and molding temperature. The molding temperature could be lowered using plasticizers, however, some of them are not suitable because they diffuse out of the polymer, while another cause an increase in the background coloration upon molding, even at lower temperatures.

*We have investigated the properties of about 50 different plasticisers and determined their effects on writing/reading efficiencies, background coloration, optical properties and thermal stability of the WORM disks. The plasticizers used in this research are listed in Table 1.*

We have studied the effect of plasticizer embedded in the polymer matrix on the kinetics and efficiency of the writing process. The speed of the writing process was determined by the reaction of the dye precursor with the photogenerated acid. The speed of this bimolecular reaction is controlled by diffusion, which in solid polymer matrices proceeds relatively slow. We expected that the addition of plasticizer to the polymer matrix will accelerate the writing process because it decreases the viscosity of the media and consequently increases the diffusion rate. At the same time, addition of polar plasticizer molecules to nonpolar polymethyl methacrylate polymer should increase the polarity of the matrix, which may have also increase the solubility and stability of the polar molecules of the written form. We found that WORM disks containing plasticizers had much better light sensitivity and faster development time than the standard disks without plasticizer. Figure 2.1.5 shows the change in absorption of WORM materials with and without added propylene carbonate as a plasticizer. The certain amount of written molecules is formed during the writing process, however concentration of the written form in the plasticizer containing material is few times higher. In addition the development of the written form absorption proceeds much faster and reaches higher intensity with the plasticized sample. The absorption intensity, after development, which characterizes the light sensitivity of the material, was also about 7 times higher for the plasticized material.

Table 1 Plasticizers for WORM materials.

plasticizer	b.p. °C	$\epsilon$	plasticizer	b.p. °C	$\epsilon$
benzaldehyde	179	17.85	hexanitrile	163.6	17.26
benzonitrile	191.1	25.9	hexylene glycol	197.1	23.4
benzil alcohol	205.3	11.92	hexyl methyl ketone	172.5	9.51
bis(2-chloroethyl)ether	178.5	21.20	isoquinoline	243.2	11.0
butanoic anhydride	200	12.8	methyl cyanoacetate	200.5	29.3
butyrolactone	204	39.0	cis-3-methylcyclohexanol	168	16.05
m-cresol	202.2	12.44	nitrobenzene	210.8	35.6
p-cresol	201.9	13.05	octanenitrile	205.2	13.90
cyclohexanol	160.8	16.4	1-octanol	195.1	10.30
diacetone alcohol	167.9	18.2	1,5-pentanediol	239	26.2
o-dichlorobenzene	180	10.12	1,2-propanediol	187.6	27.5
3,4-dichlorotoluene	208.9	9.39	1,3-propandiol	214.2	35.1
diethylene glycol	245.8	31.82	propanoic anhydride	170	18.30
diisobutyl ketone	169.4	9.91	propylene carbonate	242	66.14
DMSO	189	47.24	quinoline	237.1	9.16
ethyl acetoacetate	180.8	14.0	succinonitrile	266	62.6
ethyl cyanoacetate	205	31.62	tetraethylene glycol	328	20.44
ethylene carbonate	248	89.78	tetrahydrofurfuryl alcohol	178	13.48
ethylene glycol	197.3	41.4	thiodiethanol	282	28.61
ethylene glycol butyl ether	168.4	9.30	tolunitrile	233.5	17.87
2-ethyl-1,3-hexanediol	244	18.73	triethylene glycol	285	23.69
furfural (2-furaldehyde)	161.7	42.1	triethyl phosphate	215.5	13.20
furfuryl alcohol	171	16.85	trimethyl phosphate	197	20.6
glycerole	290	46.53	3,4-xlenol	227	9.02
1-heptanol	176.4	11.75	3,5-xlenol	221.7	9.06

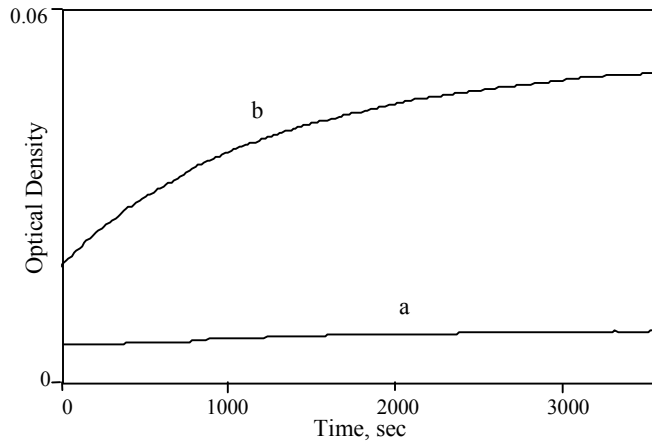


*Figure 2.1.5 Written form accumulation in a) original; b) plasticized material.*

It is known that plasticizers, such as DBP, decrease the glass transition temperature of the host plastic into which it is embedded. We have studied the effect of DBP concentration on the optical quality of molded PMMA disks, where few small pieces of plastic were molded together to obtain a uniform, optical quality disk. The molding temperature was varied from 100° to 200° C. The results of these experiments are shown in Figure 2.1.6, where the molding temperature at which the homogeneous molded disk was obtained, is plotted as a function of DBP concentration. The data show that the temperature of homogeneous fusion of the plastic pieces decreases with increase of DBP concentration.

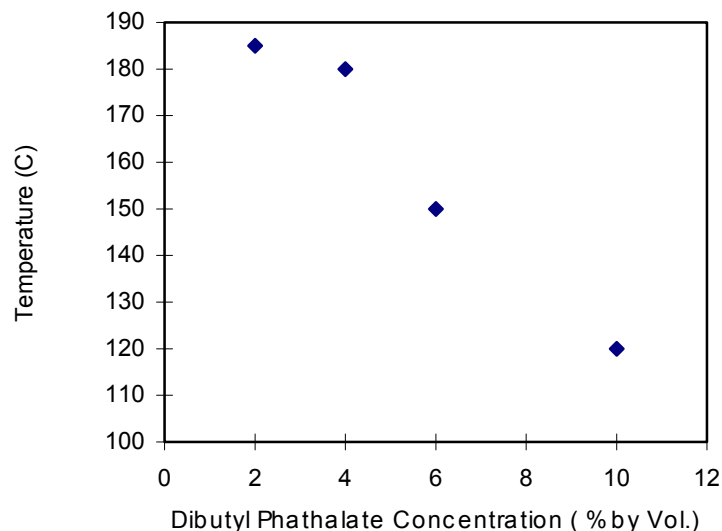


*Figure 2.1.6 Effect of DBP plasticizer concentration on molding temperature.*

To optimize the composition of the WORM material we have performed studies on effects of ingredients on various characteristics of the material, such as writing efficiency, polymerization reaction, optical and mechanical properties, background coloration and thermal stability.

We have found that introducing small amounts, 5%, of plasticizers, may further increase the concentration of the acid generator in nonpolar polymer host. The higher concentration of the acid photogenerator and the increase of the diffusion rate in the presence of plasticizers were found to increase the writing performance of the WORM disks. However, some of the commonly used plasticizers were found to be not compatible with the WORM material. The main problem was an increase in the background color of the fabricated WORM disks due to side reactions of the plasticizers with the dye precursor molecules. Other undesirable effects were the decrease in light sensitivity of the memory material and change of the WORM disk optical properties with time. Figure 2.1.7 shows the effect of various plasticizers on the writing process. The fluorescence intensity of the written bits was measured as a function of writing time. The slope of the curves corresponds to the relative writing efficiency of the material.

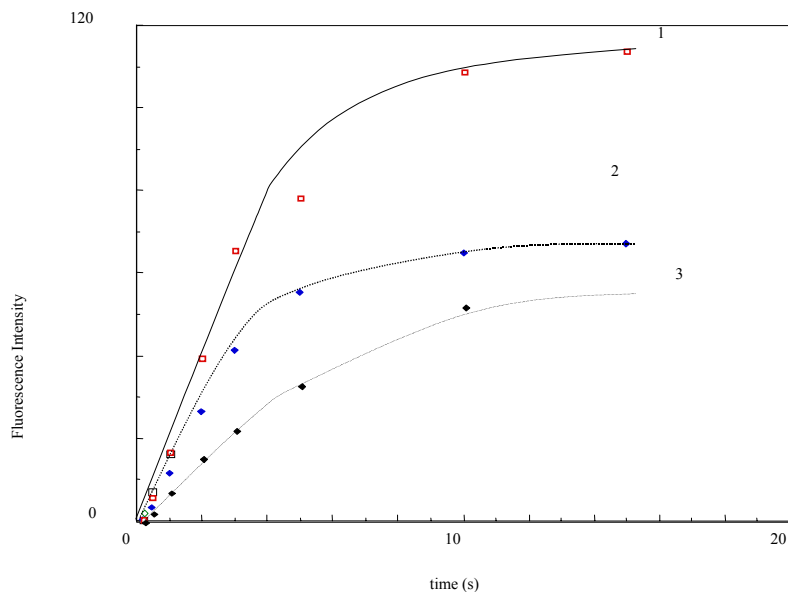


Figure 2.1.7 Effect of plasticizer on writing efficiency: 1 - ethylacetoacetate, 2 – tetrahydrofurfuryl alcohol, 3 – methyl pyrrolidinone.

Up to date we have found that the best fabricated WORM materials were based on ethylacetoacetate plasticizer. We were able to fabricate WORM disks with 3x writing efficiency and excellent thermal stability. The background coloration of the disks was also low compared to that other materials and the optical density at the 650 nm absorption maximum of the written form was less than 0.01.

#### 2.1.4 Background coloration.

Background coloration of the WORM material under elevated temperatures may complicate fabrication of the memory disks by molding. We have investigated the effects of plasticizers and molding conditions on background coloration of the molded WORM disks.

One potential plasticizer is propylene carbonate (PC), which reduces the molding temperature of 1" disks to 80 C. However, experiments indicated that PC also increases the background color. The results of the experiments with and without PC are shown in Figure 2.1.8. This figure shows the optical density vs. molding temperature for WORM disk without plasticizer and with 10% propylene carbonate. The dwell time and molding pressure were 5 minutes and 3800 lbs/in<sup>2</sup> respectively. It can be seen from this figure that PC does cause a considerable increase in background color relative to nonplasticized material at temperatures above 160 C and a smaller coloration increase at T<150 C. This increase in background color occurs, most probably, as a

result of partial decomposition of PC at elevated temperatures or reactions with possible impurities contained in the commercially available propylene carbonate.

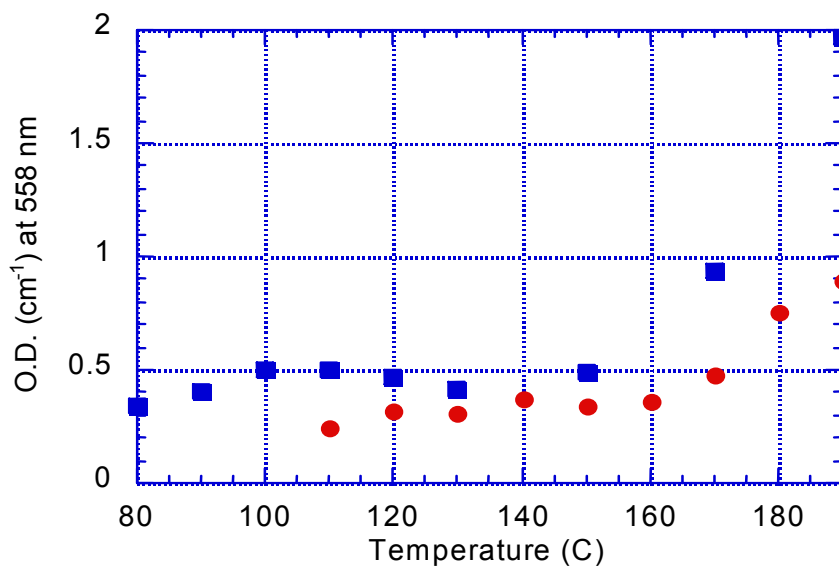


Figure 2.1.8 Dependence of optical density on molding temperature for nonplasticized (●) and plasticized (■) by 10% PC materials. OD after polymerization =  $0.113 \text{ cm}^{-1}$  and  $0.169$  for nonplasticized and plasticized materials respectively, pressure =  $3800 \text{ lbs/in}^2$ , dwell time =  $5 \text{ min}$ .

The effect of molding temperature on WORM materials prepared with 5% and 10% DBP is shown in Figure 2.1.9 and Figure 2.1.10, which display the optical density of the molded disk, measured at the maximum of absorption of the written form, plotted as a function of molding temperature. The optical density was normalized to disk thickness. In this experiment the dwell time, the time a disk remains in the mold under the T and P, was 1 minute and the pressure  $3800 \text{ lbs/in}^2$ . As can be seen, there is a slight increase in the background for molding at 70 and 80 C, background level increases as the molding temperature is increased.



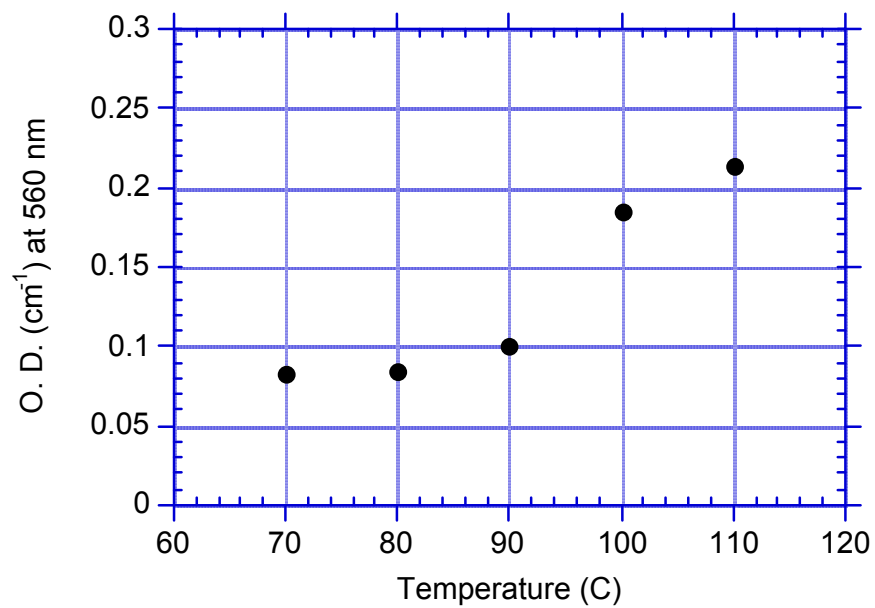
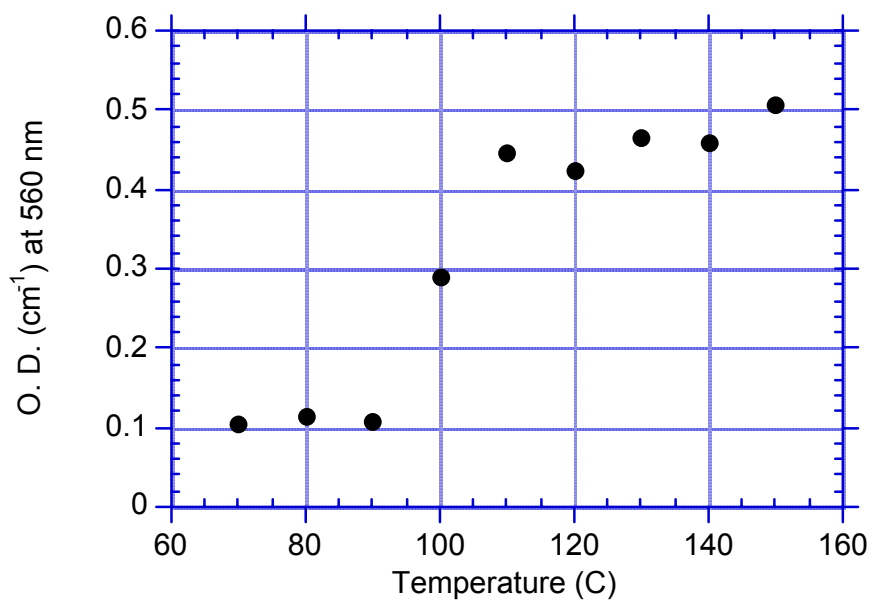
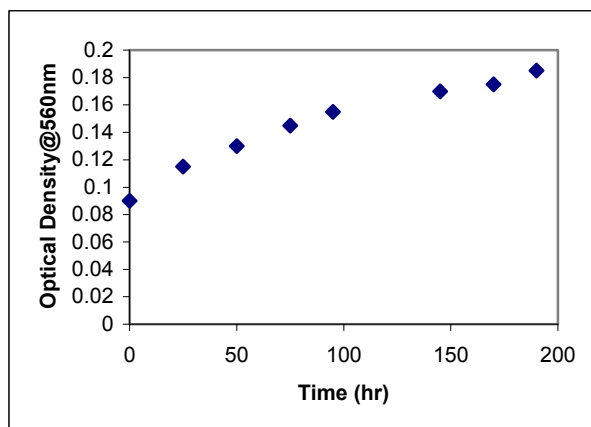


Figure 2.1.9 Dependence of optical density on molding temperature for WORM material prepared with 5% DBP. The optical density before molding was  $0.067 \text{ cm}^{-1}$ .



*Figure 2.1.10 Dependence of optical density on molding temperature for WORM material prepared with 10% DBP. The optical density before molding was  $0.101\text{ cm}^{-1}$ .*

We have studied the effect of humidity on background coloration of WORM materials containing Rhodamine B base (RBb) and Rhodamine 700 base (RDP) dye precursors. The molded WORM disks were placed in environmental chamber and kept for about 200 hrs at room temperature and 95% relative humidity. As shown in Figure 2.1.11 and Figure 2.1.12, the materials with RBb dye precursor start to develop background color with time due to diffusion of water molecules in the polymer matrix, followed by reaction with RBb. The materials with RDP were not affected by high humidity.



*Figure 2.1.11 OD vs. time at  $20^{\circ}\text{C}$  and 95% rel.humidity for RBb containing WORM disk.*

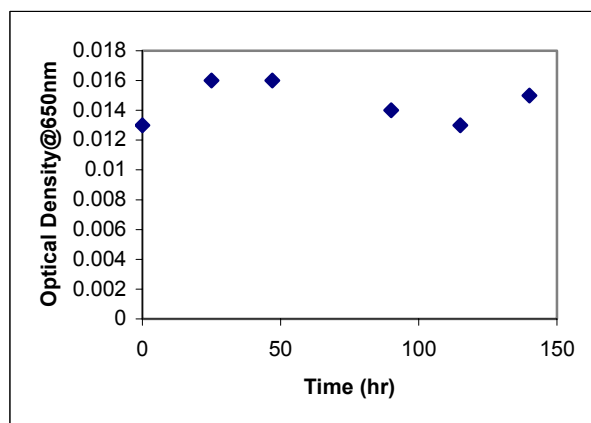


*Figure 2.1.12 OD vs. time at  $20^{\circ}\text{C}$  and 95% rel.humidity for RDP containing WORM disk.*

### **2.1.5 Fatigue.**

The fatigue resistance to readout light was measured for WORM materials containing Rhodamine B base and Rhodamine 700 base dye precursors. The Ne-Ne laser with green output

1.5 mW at 543 nm was used as a light source for Rhodamine B material and the CW diode laser, which emits at 658 nm, 50 mW/cm<sup>2</sup> for Rhodamine 700 material. Using a telescope a light beam with cross section of 0.2 x 5 mm was form. The fluorescence from the image, recorded by two-photon absorption inside the memory cube, was focused on a CCD camera and digitized. A cut off filter was used to block the scattered green or red light and ND filters were used to achieve a desired attenuation. The output power was measured with Molelectron power meter.

The fatigue resistance was measured for plasticized and nonplasticized WORM materials. The data presented in Table 2 show that plasticizer does not affect significantly the light stability of the written form.

*Table 2. Effect of plasticizer.*

Reading light Intensity mW/cm <sup>2</sup>	80	35	16	8
Nonplasticized material half lifetime, h	1	3.5	6	12
Plasticized material half lifetime, h	2.5	4	6.5	13

We have measured the stability of the written form for Rhodamine B (GWORM) and Rhodamine 700 (RWORM) materials. The fluorescence intensity emitted by the written bits of the GWORM and RWORM materials was recorded as a function of reading time. The RWORM disk was read by the 658 nm light emitted by diode laser, and GWORM was read by a 543 nm light emitted by He-Ne laser. The intensities of the reading light in both cases were 40 mW/cm<sup>2</sup>. The normalized fluorescence intensities plotted as a function of excitation time are shown in Figure 2.1.13. The data presented show that the RWORM material exhibits much better fatigue resistance to the reading light than GWORM material.

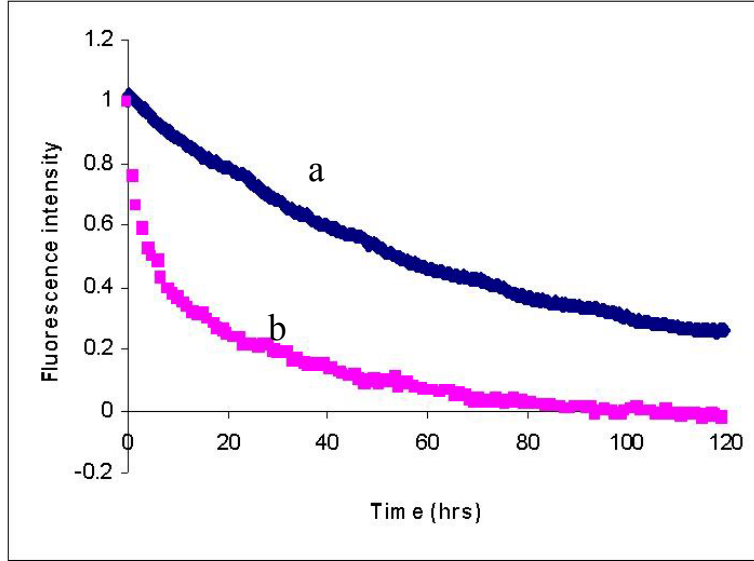
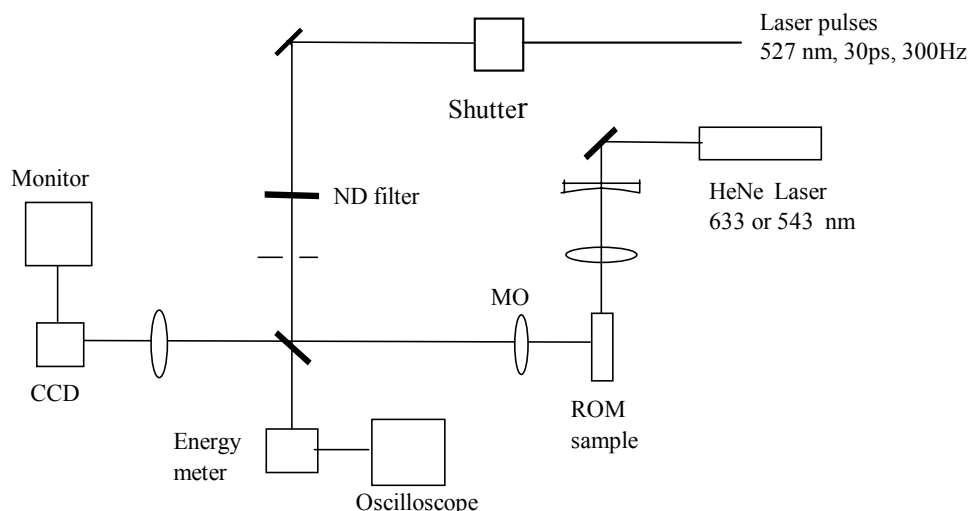


Figure 2.1.13 Written form fatigue measurements for: a) RWORM; and b) GWORM materials.

### 2.1.6 Writing efficiency

To characterize and compare the writing efficiency of different 3D memory optical materials, we devised and build the experimental system shown in Figure 2.1.14. In this system a Nd:YLF laser was used as the light source, generating 30ps, 527nm light pulses at repetition rate of 300Hz and average power of 100 mW. To avoid possible thermal effects caused by high repetition rate pulses, a single pulse or burst of pulses were separated, by means of a mechanical shutter, and used in these experiments. The laser radiation after passing through a microscope objective (10X, NA 0.25) was focused onto the optical memory disk. The diameter of the spot at the focus of the microscope objective was calculated to be about 6 $\mu$ m. The intensity of the recording pulse in the focus was between 50 and 100 GW/cm<sup>2</sup> and the pulse energy was monitored by a reference pyroelectric energy meter. The energy of every pulse was recorded in a storage oscilloscope, Tek DSA 602. The position of the sample was determined with 10 $\mu$ m accuracy. The fluorescence emitted from the written bits was collected by the microscope objective and detected by a CCD camera equipped with 205 mm lens. A red filter in front of the CCD was used to block the reading excitation light. For reading, we used cw HeNe lasers (633 nm or 543 nm) to illuminate the sample, or 527 nm, 100 ns low power laser pulses at 300 Hz, generated by the same laser. In this case the optical paths of recording and reading beams were the same.



*Figure 2.1.14 Experimental system for damage threshold and writing intensity.*

We have measured the dependence of fluorescence intensity emitted by the written bits on the writing light intensity. The results of the experiment shown in Figure 2.1.15, where the log of the written bits fluorescence intensity is plotted as a function of the log of the writing light. In this case the theoretical slope of this curve should be equal to 1 for the single photon absorption process and 2 for the two-photon absorption. The data show that the slope measured for GWORM material is 1.5, which means that there are both single and two-photon processes involved in the writing mechanism. For RWORM material the equivalent slope measured was found to be equal to 2.1 that confirms the two-photon absorption process. In agreement with previous studies, the Rhodamine B base dye precursor alone has a weak absorption band in the region of 530 nm that may contribute to the single photon absorption process and explain the background observed and the 1.5 slope. Measurements of the written bit size indicate that the GWORM bit size is bigger than that for RWORM, which corresponds to the theoretical one calculated for two-photon writing process.

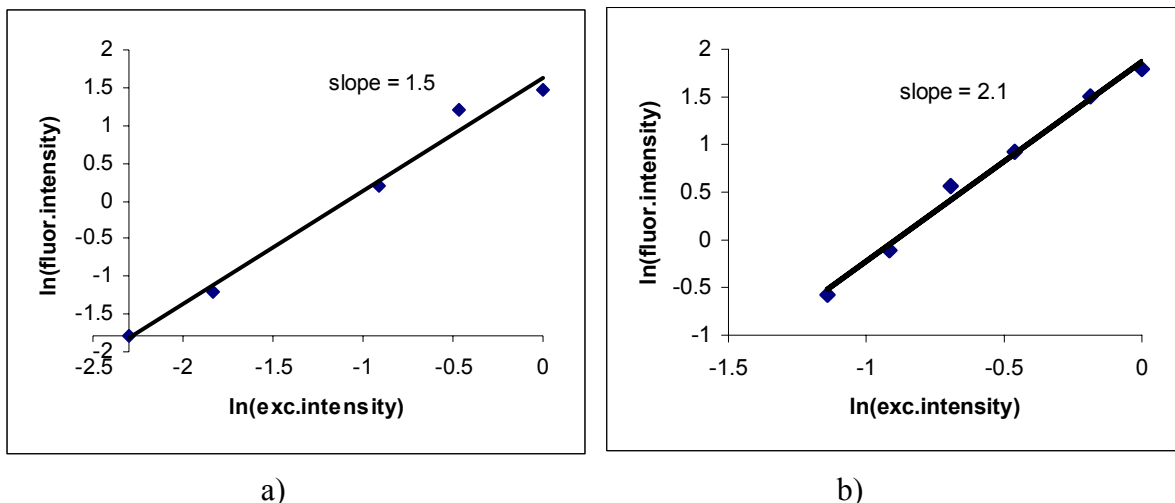
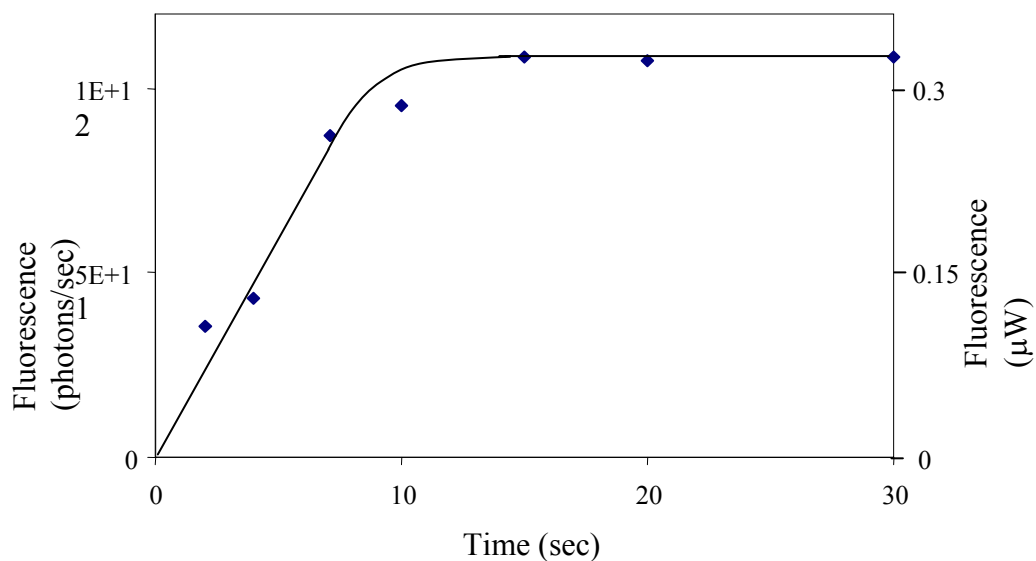


Figure 2.1.15 Written form fluorescence intensity vs. writing light intensity: a) GWORM; b) RWORM. Information written by 527 nm light.

To characterize the writing efficiency of the WORM materials we have measured the dependence of fluorescence intensity, emitted by the written bits, as a function of writing time. To measure the absolute number of photons, emitted by the written bits, we have calibrated the CCD with a 676 nm light emitted by the diode laser, which intensity was measured by means of a calibrated energy meter. The 676 nm laser diode was chosen because this wavelength corresponds to the fluorescence maximum of the written form.

The optical quality polished 10mm x 10mm x 1.6mm sample of WORM material was written by two-photon excitation with 527 nm light. The writing beam was shaped in 1 mm x 30  $\mu\text{m}$  plane by means of cylindrical lens. The same size plane beam, emitted by 633 nm He-Ne laser, was used for illumination of the written plane. Based on the optical design of our experimental system, we calculated that 2% of the fluorescence emitted by the written area was collected on the CCD detector. Figure 2.1.16 shows the fluorescence intensity, emitted by a 1mm x 1.6 mm x 20 $\mu\text{m}$  written area, plotted as a function of writing time. The average power of the reading beam was 3.6  $\mu\text{W}$ . The curve shows the saturation in written bit fluorescence intensity, which corresponds to the maximum of the written form concentration.



*Figure 2.1.16 Written plane fluorescence intensity vs. writing time*

The relative writing efficiency and fatigue resistance were measured for WORM materials containing various acid generators. The results of the experimental measurements are shown in Figure 2.1.17 for triphenylsulfonium salt and modified salt with long chain attachment. Both materials show about the same slope. Because the concentration of the modified acid generator in this experiment was 3 times lower than the original, the writing process efficiency of the new WORM material by two photon absorption of 527 nm beam, is 3 times higher. The measurements of fatigue resistance, shown in Figure 2.1.18, show that both materials are equally stable under these experimental conditions.

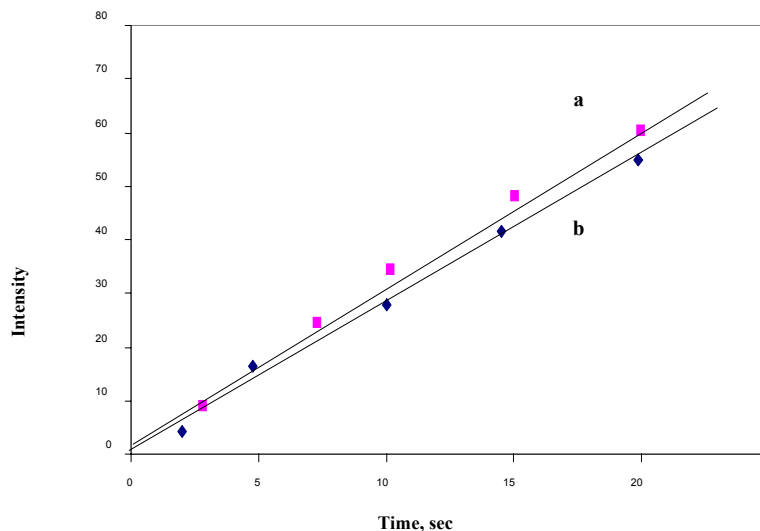


Figure 2.1.17 Writing efficiency measurements: *a* – original material; *b* – modified material

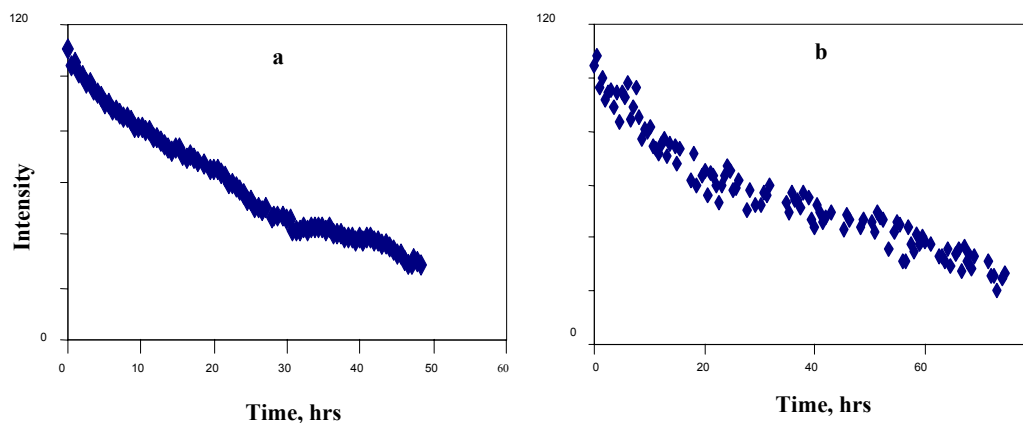


Figure 2.1.18 Fatigue measurements: *a* – original material; *b* – modified material

### 2.1.7 Fabrication of WORM disks.

The WORM materials, which involve a new, effective acid photogenerator, were prepared by polymerizing methyl methacrylate (MMA) monomer solutions of onium salt and dye precursor, which was initiated by AIBN. The solubility of the onium salts in nonpolar solvents like MMA is not high enough to create the concentrations required for efficient two-photon writing. To increase the concentration of the onium salt in PMMA matrix we added polar plasticizer additives, to the above monomer solutions.



1" WORM disks were fabricated by molding PMMA based plastic into which we have embedded WORM photochromic materials. The surfaces of the disks were polished to optical quality sufficient to be used in the experimental WORM system. The molding temperature was kept at 110° C and the dwell time at 10 min. We have found that, under these molding conditions, the fabricated disks had relatively low background color. The optical density at 650nm, the written form absorption band maximum, was less than 0.02. Molding WORM disks at higher temperatures or prolonged dwell time leads to increased background coloration that may reach unacceptable levels. This increase in background color, formed in the molded disks at high temperatures, remains a major problem for fabrication methods that require high temperatures and prolonged dwell times.

Based on our experimental data for newly synthesized acid generator we were able to fabricate WORM disks with 3 times higher writing efficiency. 1" WORM disks were prepared by molding of polymer material contained new acid generator in concentration 1.5 times higher than was used for original acid generator. Because the absorption crosssection at 266 nm of modified molecules 2 times higher than the original ones, the total sensitivity of obtained WORM material was expected to be 3 times higher. The results of measurement of writing efficiencies for this and original materials are shown in Figure 2.1.18. To compare the writing efficiencies the fluorescing bits were written in both materials by two photon absorption of 527nm, 35ps, 180  $\mu$ J/pulse, 300 Hz repetition rate light pulses, generated by SHG Nd:YLF laser. The intensity of fluorescence emitted by the written bits was measured also as a function of the writing time. The writing efficiency of the WORM material characterized by the slope of the linear part of the sensitivity curve, before it reaches the saturation limit. The data show that the modified WORM material has 3 times higher sensitivity (slope=68.2) than the original one (slope=21.4). The saturation level is the same for both materials, because it depends on the available concentration of dye precursor, which is the same for both materials.

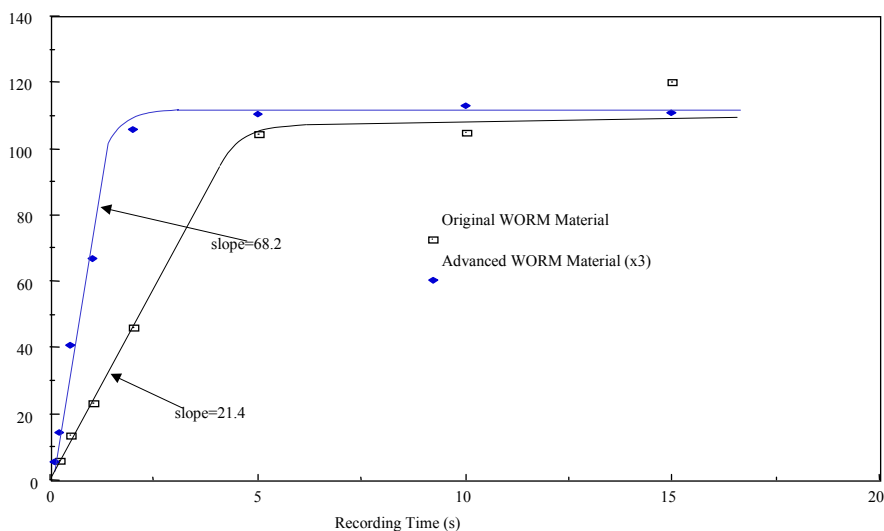


*Figure 2.1.19 Writing efficiency of original and modified WORM materials.*

To achieve 3x sensitivity of the WORM material the amount of acid generator should be 35 mg/cm<sup>3</sup>. This relatively high concentration of the modified acid generator in PMMA can be easily achieved without adding plasticiser to the polymer, owing to the high solubility of the acid generator molecules in PMMA. However, our experiments show that certain amount of the plasticiser is required to enhance the sensitivity of the material. *Figure 2.1.20* shows the written form growth kinetics measured for these materials that also contained 10% plasticiser and without plasticizer. The samples were illuminated, with UV light, for 10 sec under the same conditions and then the change in absorption, at the 650nm absorption maximum of the written form, was measured as a function of time. The data suggests that accumulation of the written form occurs faster and reaches a higher absorption value for the sample containing plasticizer than the one without. The increase in writing efficiency for the sample containing plasticizer is due to faster diffusion processes and stabilization of the polar dye molecules by the polar plasticizer.

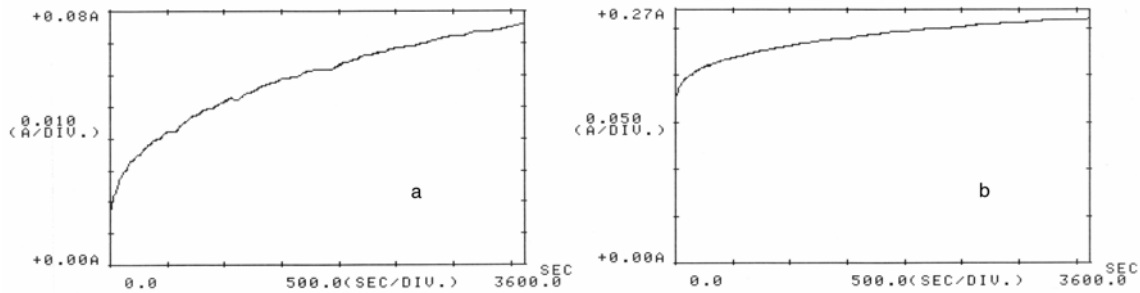


*Figure 2.1.20 Written form accumulation kinetics: a – without plasticizer; b- 10% plasticizer.*

We have fabricated optical quality 1" diameter WORM3x disks by molding PMMA based polymer to which 35mg/cm<sup>3</sup> of modified acid generator and 5% of ethyl acetoacetate plasticizer were added. The disks were molded at 110° C for 10 min, under these conditions the background absorption at 650 nm was less than 0.02 OD.

We have conducted fatigue tests of WORM disks, which show that the fatigue resistance during readout remained the same, *Figure 2.1.21*.

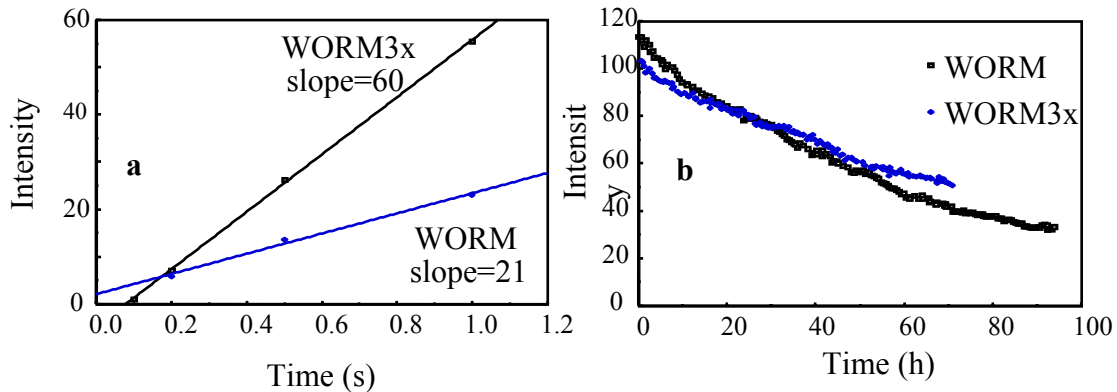


*Figure 2.1.21 Sensitivity (a) and fatigue (b) measurements for WORM and WORM3x*

To fabricate 3.5" diameter WORM disks we polymerized monomer solutions of WORM components in specially designed polymerization cell, shown, schematically, in Figure 2.1.22. The ¼" thick teflon spacer that has the shape, shown in Figure 2.1.22, was squeezed and sealed between two flat metal plates. A hole in one of the metal plates and in the spacer allows us to fill the cell with the mixture to be polymerized. In addition this allows us to conduct the polymerization reaction under nitrogen pressure that reduces the possibility of bubble formation. The inner diameter of the cell was made slightly bigger than 3.5" to allow for the formation of 3.5" disks even assuming the polymer may shrink. The cell has also an additional area on the top filled with the excess of the polymerization mixture to compensate for the decrease in the volume during polymerization. We were able to fabricate optically clear polymer blocks, which were cut and molded into 3.5" disks with the required optical quality.

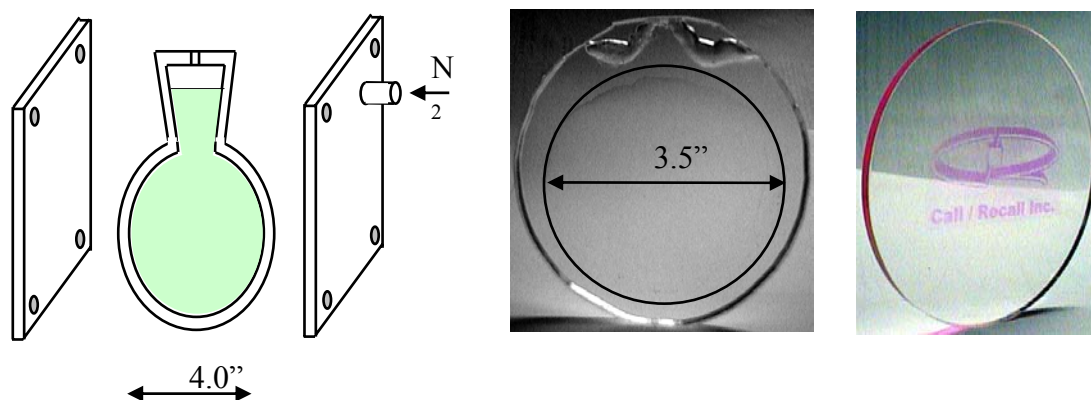


Figure 2.1.22 Polymerization cell with teflon spacer (left) and 3.5" WORM disks (right).

### 2.1.8 Optical quality

Surface profiles of disks after lapping/polishing with various grades were compared in order to determine the improvement of the surface with each step, and to evaluate the quality of the surface after the final polish. Also, the surface of a 3.5" molded disk without polishing was compared to a fine polished disk. This comparison is shown in Figure 2.1.23.

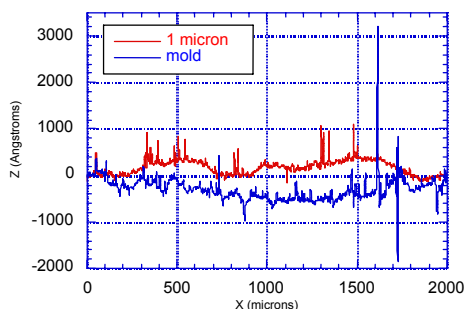
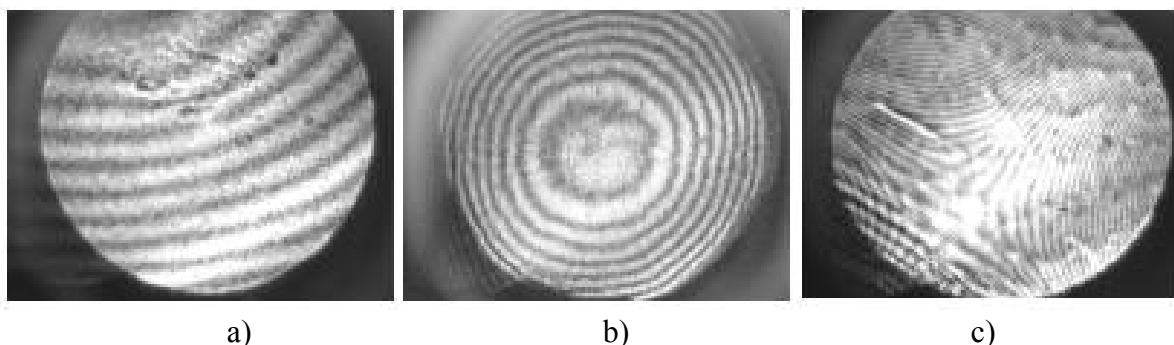


Figure 2.1.23 Comparison of polished and molded surfaces.

The surface qualities of the 3.5" diameter plastic disks produced by our molding process were measured using a laser interferometer, operating at 543 nm. Figure 2.1.24 (a) shows the interferogram of the mold surface, which we use for the molding plastic disks. The average flatness of the mold surface is about a half wavelength over 10 mm distance. Figure 2.1.24 (b) shows the interferogram of the surface of the molded plastic sample and its flatness is measured to be about one wavelength over 10 mm. We also compared the surface quality of our molded disks with the quality of a commercial optical CD, which is also made by molding. The interferogram of such a CD is shown in Figure 2.1.24 (c). The interferograms obtained with the CD ROM disk were taken with the same experimental system. It is obvious that the optical quality of our molded plastic disks is much higher than the one for the commercial CD ROM discs. Utilizing a better quality mold and appropriate molding conditions we can further improve the optical quality of our 3D molded disks.



*Figure 2.1.24 Interferogram of a) 3.5" mold; b) molded 3.5" disk; c) commercial optical CD*

### **2.1.9 Temperature stability**

In order to fabricate the memory material by extrusion or injection molding, the material should be stable at the temperatures required by these processes, which could be as high as 200°C. We have studied the thermal stability of the WORM disks, as well as the stability of the individual components. It was found that the molding of WORM disks at elevated temperatures, higher than 120°C, and prolonged dwell time causes an increase in background coloration. High temperature processing also was found decreases the material sensitivity to the photoreactions. To understand the mechanism of these undesirable processes we have performed thermal stability tests of the individual components of the WORM material. These include the polymer host, acid generator, dye precursor and plasticizer. It was found that acrylic polymers, commonly used in extrusion and injection molding, do not produce any decomposition products up to 200°C, which may cause the background coloration of the WORM material. The newly developed high solubility acid generator was found stable even at much higher temperatures than required by injection molding, no decomposition of this material was detected up to 370 °C.

The thermal stability of various plasticizers was tested in molding experiments, where characteristics of the fabricated disks, such as light sensitivity and background coloration, were

measured as a function of the molding temperature and dwell time. Figure 2.1.25 shows the effect of some plasticizers on background coloration.

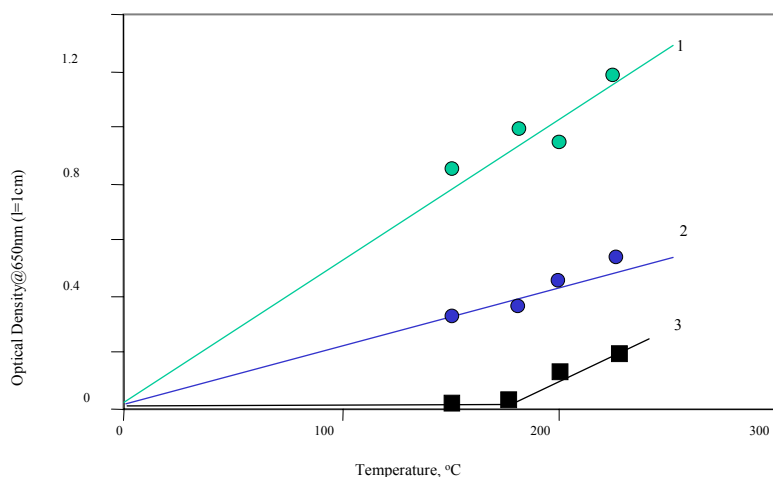


*Figure 2.1.25. Temperature stability of various plasticizers and their effect on background coloration of the molded disks: 1 – methyl-cyanoacetate; 2 – sulfolane; 3- ethyl-acetoacetate.*

Analysis of the accumulated data suggests that ethyl-acetoacetate is the best plasticizer for use with WORM material, because it improves the writing characteristics and thermal stability of the memory disks.

The thermal stability of the dye precursor used in WORM disks was tested in high boiling point solutions and the crystalline state. The dye precursor molecules were heated to various temperatures from 100 to 200 °C, or the time period held at these temperatures varied from 10 to 30 min. The temperature treated materials were analyzed for decomposition and its ability to be transferred into the written, colored form. It was found that the dye precursor molecules are stable up to 150 °C, higher temperatures induce decomposition reactions, which result in decreasing light sensitivity of the WORM material, as shown in Figure 2.1.26.

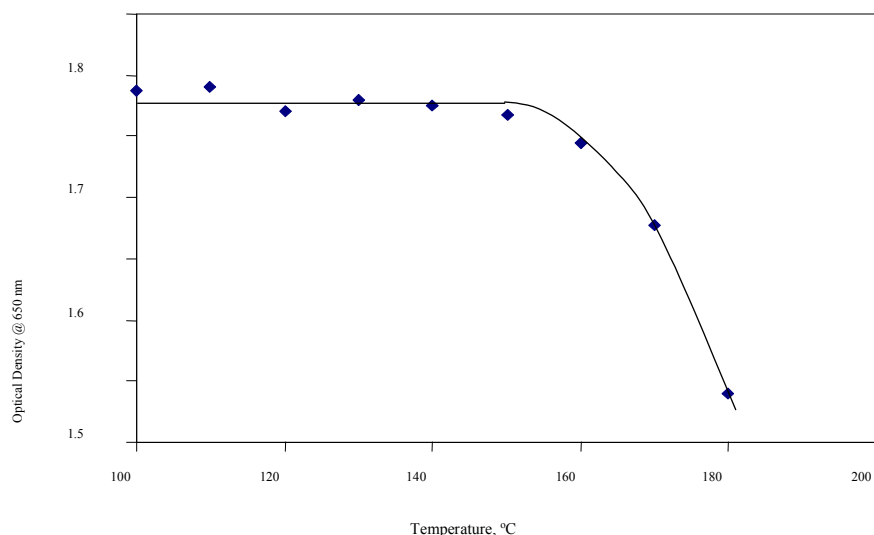


*Figure 2.1.26. Effect of temperature on dye precursor write-read form transformation ability*

These results show that the temperature stability of the present dye precursor is not high enough to be used for fabricating WORM disks with this material using either extrusion or injection molding processes. Therefore, more stable molecules should be developed for extrusion and/or injection molding.

### **Summary of accomplishments in Materials and disk formation**

- 3.5 inch diameter, 5mm thick disks fabricated
- 3X Higher writing efficiency
- 10X Lower background noise
- 3X Higher readout fatigue resistance
- Higher temperature stability

## **2.2 Recording Optics**

In our quest to demonstrate a WORM volumetric optical disk system based on two photon recording and fluorescence readout, we have completed the modeling of the recording process, experimentally validated this model and used it to optimize our recorder systems. We will first present the model and later discuss the recorders that we have built and discuss their performance.

### 2.2.1 Analysis Model for Recording Speed and Experimental Validation

A pictorial model is presented in Figure 2.2.1 to aid in understanding of the recording data rate of two-photon recording. Influence of important parameters such as the concentration of recorded molecules, peak laser power, pulse width, and repetition rate are included in the analysis.

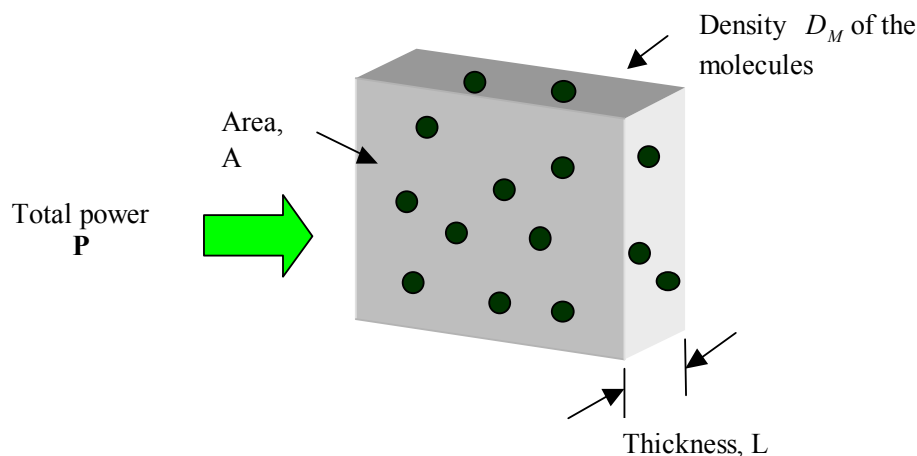


Figure 2.2.1 The two-photon recording analysis model

In Figure 2.2.1 the recording laser is assumed to be diffraction-limited plane-wave illumination, the media sample thickness is  $L$  and the cross-sectional area of the sample is  $A$ ,  $D_M$  is the density of the molecules. The two-photon cross section,  $\sigma$ , is the two-photon cross section of this type of molecule and is a constant. Equation 1 describes how much energy per unit time (or the power) is absorbed by one molecule during the two-photon absorption process,  $\Delta P'_{\text{abs}}$ . The laser beam irradiance,  $I$ , is the power per unit area.<sup>2</sup>

$$\Delta P'_{\text{abs}} = \sigma I^2 = \sigma \left( \frac{P}{A} \right)^2 \quad \text{Equation 1}$$

Equation 2 considers all the molecules inside a unit volumetric sample of dimensions  $AL$ , where  $\Delta P_{\text{abs}}$  is the total amount of energy absorbed at a unit time by all the molecules inside the sample during the two-photon absorption.

$$\Delta P_{\text{abs}} = D_M AL \sigma I^2 = D_M AL \sigma \left( \frac{P}{A} \right)^2 = D_M L \sigma \frac{P^2}{A} \quad \text{Equation 2}$$

A pulsed laser is used for recording as the two-photon absorption has a characteristically small cross section,  $\sigma$ , where  $\Delta P_{\text{abs}}$  scales as the recording laser irradiance squared. During each laser pulse an amount of power,  $\Delta P_{\text{abs}}$ , is absorbed within the time of the laser pulse and can be expressed as the number of recorded molecules  $M_P$  from each laser pulse, multiplied by  $2h\nu$  the two-photon energy divided by the pulse width as shown in equation 3 ( $\nu$  is the recording laser

frequency). The laser power  $P$  can be expressed as the number of photons  $N_p$  in each laser pulse multiplied by  $h\nu$  divided by the pulse width  $t_p$ .

$$M_p 2h\nu = \frac{D_m L t_p \sigma}{A} \left( \frac{N_p h\nu}{t_p} \right)^2 \quad \text{Equation 3}$$

Multiplying  $M_p$  (the number of recorded molecules in each pulse) by  $f_{\text{rep}}$  (the laser repetition rate) is proportional to the recording speed  $V_r$ .

$$V_r \propto M_p f_{\text{rep}} = D_M L \left( \frac{\sigma N_p^2 f_{\text{rep}} h\nu}{2 t_p A} \right) \quad \text{Equation 4}$$

Equation 4 is based a simplified model without considering some complicated chemical processes. But it still expresses closely how the laser and media properties impact the recording speed.

From equation 4 it is observed that with higher peak power,  $N_p/t_p$ , the recording will take place faster. The recording speed limit is also directly proportional to the repetition rate of the recording laser, if it is assumed that one pulse can record one bit. In practice it may take several exposures of a pulsed laser to record a bit sufficiently to a level of recorded molecules that is sufficient to cause enough fluorescence on readout for acceptable signal quality. Also, if the focused laser beam can be made smaller this reduces the area,  $A$ , allowing even faster recording. When using one laser beam for two-photon recording, the recording location inside the media is controlled by the laser intensity profile. These equations are applicable not only to the single-beam recording, but also for the two-photon two-beam recording.

### Experimental Validation Experiments

WE have validated the above presented model using a diode pumped 532nm wavelength Nd:Vanadate laser having pulse width 6.5pSec at a repetition rate of 76MHz. The average power is 5W and peak power is 28KW. Focusing the high peak power laser inside the disk using 0.5NA (NA, numerical aperture) optics achieves a 20GW/cm<sup>2</sup> laser irradiance at focus. The recording speed is observed at over 1Mbits/sec.



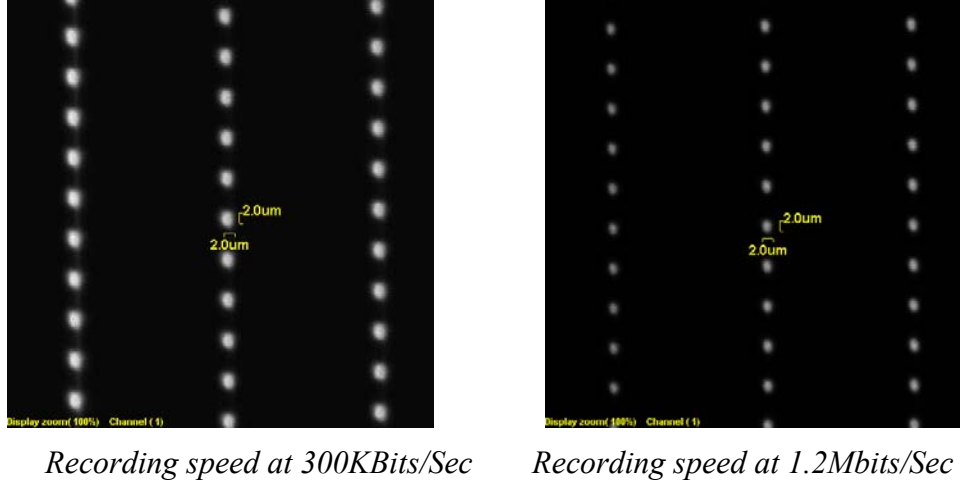


*Figure 2.2.2 Fluorescent confocal microscope image of data tracks recorded at different speeds with  $2 \times 2 \mu\text{m}^2$  fluorescence bits*

The raw data channel recording speed is specified as how many data bits per second. As described in our model above the recording speed is also related by the size of one data mark and the minimum amount of recorded molecules per bit required for detection. The user recording data rate depends on which channel modulation method is used and is always less than the raw data channel rate (typically 50%). Figure 2.2.2 shows fluorescent confocal microscope images of data tracks recorded at different recording data rates. The tracks with the faster recording rate are observed to have weaker fluorescent signal amplitude due to less cumulative laser pulse exposure at a particular bit location. For instance, if the disk is spinning at 60Hz (for 1Mbit/s recording) there are  $1.26 \times 10^6$  pulses in one revolution, and assuming a 16kbit single track capacity, there are 79 laser pulses per bit. Alternatively, if the disk is spinning at 15Hz (for 300Kbit/s recording) there are  $5.06 \times 10^6$  pulses in one revolution, and assuming a 16kbit single track capacity, there are 316 laser pulses per bit. The recording speed achieved is close to 1Mbits/Sec with a 2um mark length along the data track, (In Figure 2.2.2, we give the recording speed for each case assuming one 2um mark representing one bit). Serial data channel recording is used throughout the demonstrations and experiments. Parallel recording was not investigated due to the unavailability of suitable lasers with sufficient recording power to record many channels simultaneously.

### 2.2.2 Disk test-stand

Using the model presented above and the figures measured during experimental verification of the model we have designed and built a recorder diskstand. The Figure 2.2.3 shows the structure

of our single-beam two-photon recording system. The system also includes a readout path and detector for recording evaluation.

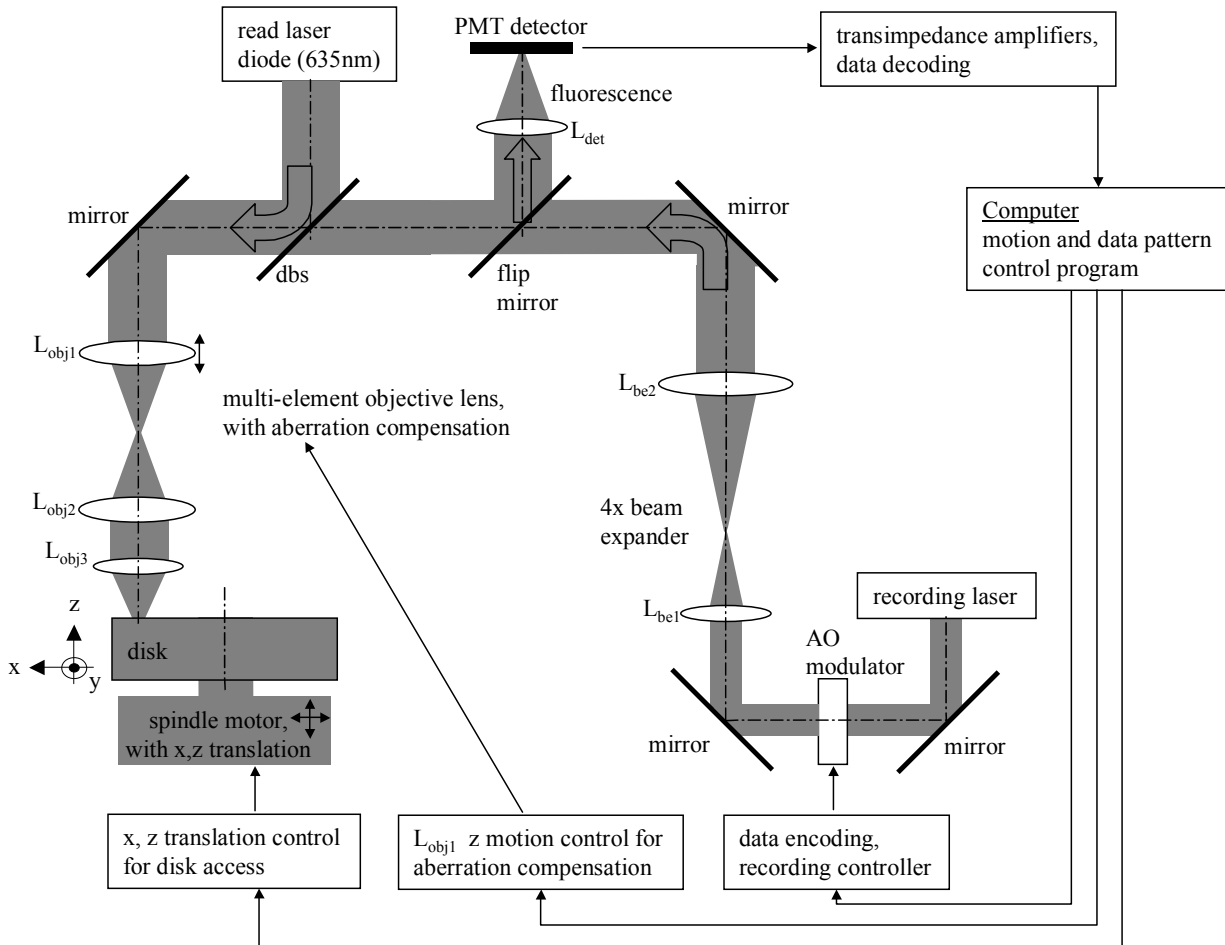


**Figure 2.2.3** Single-beam two-photon recording system diagram

The recording laser is the 532nm HighQ diode pumped Nd:Vanadate system described previously. An Isomet Acoustic-Optic modulator modulates the recording laser in accordance to the desired data pattern that is sent from the computer through a RS232 controller. The recording laser then passes through a beam expander on its way to the objective lens assembly that will be described in the next section. The objective lens then focuses the recording laser inside rotating disk media and data is recorded. The motor used to spin the disks is a Seagull high precision air-bearing spindle. After recording a 635nm laser diode is collimated and focused by the objective lens inside the disk to excite fluorescence from recorded data bits. The fluorescence is then picked up by the same objective lens and focused onto a PMT detector.

### 2.2.3 Spherical aberration compensation

2-photon absorption techniques are used to record data tracks at different layers within a monolithic thick plastic disk. Readout of the 2-photon recorded marks is by fluorescence of

written molecules excited by single photon absorption.<sup>3,4</sup> High NA optical systems for both recording and readout are desired in order to resolve finer detail and increase areal density. This leads to the highest possible total storage capacity for single layer and multilayer media. One challenge to high NA multilayer systems is the change in spherical aberration that is introduced when focusing the objective lens from layer 1 to layer N. This change in spherical aberration if left uncompensated results in adverse changes to the MTF by lowering contrast, and reduced Strehl ratio with redistribution of the energy from the central core into the sidelobes. High Strehl ratio and small spot size is very important for single beam 2-photon recording systems in order to achieve the smallest data bit size possible, and increased 2-photon writing efficiency through the virtue of increased irradiance within the central core of a properly compensated focused spot.<sup>5</sup>

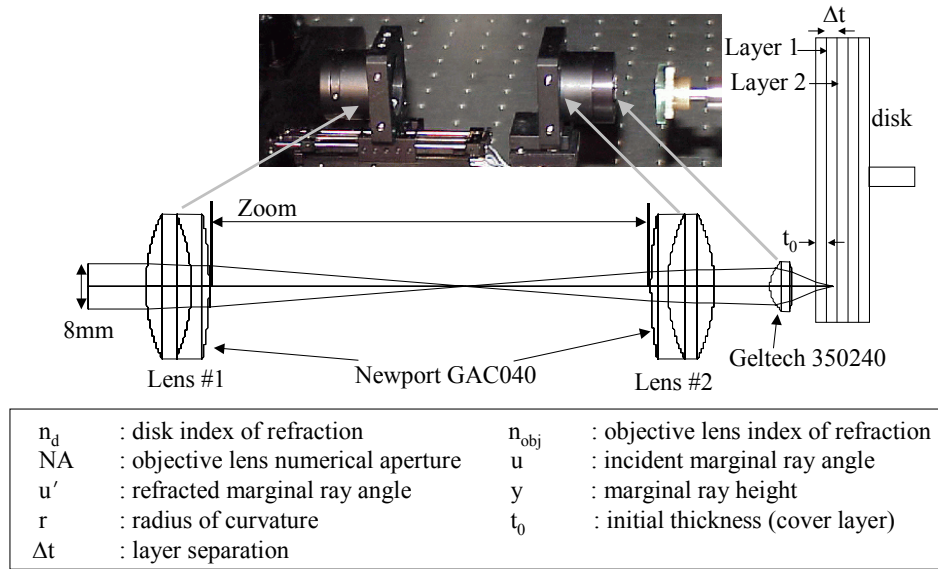


*Figure 2.2.4 Optical system layout for two-photon recording and readout using a Keplerian conjugate compensation system to offset the spherical aberration introduced by the disk during layer addressing having layer separation  $\Delta t$ .*

The following describes an optical system that compensates the spherical aberration introduced when writing and reading at different layers within our multilayer media. This is based upon a conjugate changing optics technique.<sup>6</sup> The conjugate changing optics technique is adopted, as it is more cost effective than currently available adaptive (deformable mirror) devices. Figure 2.2.4 shows the Zemax layout of the experimental system that is currently being used. The configuration of the conjugate changing optics is a Keplerian telescope system where lens #1 of the telescope is adjusted longitudinally to change the angle of incidence upon the highly curved surface of the Geltech 0.5NA objective lens that is corrected for infinite conjugates and 0.25mm of coverglass material. The action of changing the angle of incidence upon this surface results in the generation of spherical aberration of the opposite sign of that introduced when focusing into the thick media. This results in diffraction-limited performance throughout the entire depth of the disk. One disadvantage to this approach is that as deeper and deeper layers are recorded the effective working NA of the objective lens is reduced slightly resulting in larger spot sizes at the deep layers as compared to layers near the surface. However, the

Strehl ratio, or the peak power in the focused spot is much higher with the compensating optics than without them

A multilayer optical disk can be modeled as a plane parallel plate. Equation 1 describes the spherical aberration,  $W_{040}$ , introduced by a plane parallel plate where  $n$  is the index of refraction (typically 1.48 for PMMA based materials),  $NA$  is the numerical aperture, and  $t$  is the disk thickness.<sup>7</sup>

$$W_{040} = -\frac{1}{8} \frac{n^2 - 1}{n^3} NA^4 t \quad \text{Equation 5}$$

Equation 2 describes the initial spherical aberration introduced at a particular depth inside the disk, such as the cover layer thickness that the objective lens is designed for.

$$W_{040_{ini}} = -\frac{1}{8} \frac{n_d^2 - 1}{n_d^3} NA^4 t_0 \quad \text{Equation 6}$$

Equation 3 describes the incremental spherical aberration introduced by layer addressing.

$$\Delta W_{040} = -\frac{1}{8} \frac{n_d^2 - 1}{n_d^3} NA^4 \Delta t \quad \text{Equation 7}$$

Equation 4 describes the spherical aberration of a refracting surface as a function of marginal ray properties.

$$W_{040_{rs}} = -\frac{y}{8} \left( n_0 u - \frac{n_0 y}{r} \right)^2 \left( \frac{u'}{n_{obj}} - \frac{u}{n_0} \right) \quad \text{Equation 8}$$

Equation 5 describes the goal of minimizing the sum of equations 2-4.

$$W_{040_{rs}} + W_{040_{ini}} + \Delta W_{040} = 0 \quad \text{Equation 9}$$

To experimentally verify the performance of the system in Figure 2.2.4, a 532nm wavelength modelocked laser is collimated with a beam diameter of ~8mm. The beam is then launched into the telescope, made with Newport gradium achromats, and focused by the 0.5NAGeltech objective lens having focal length of 8mm. Since spot sizes must be measured externally from the disk material, different thickness coverglass are inserted into the converging beam providing an equivalent amount of material thickness for focusing to a particular layer depth. Lens #1 moves an appropriate Zoom distance for material compensation. The spot size is measured with a BeamMap® spot scanner using a knife-edge method and a video microscope through material thickness from 0.5mm – 3.0mm. Table 3 shows the simulated and experimental spot sizes for coverglass thickness ranging from 0.5mm - 3mm. The simulated and experimental spot sizes agree very well.

*Table 3:* Table of material thickness and knife-edge measurements of  $1/e^2$  spot size diameters as measured with the BeamMap® spot scanner.

Material Thickness (mm)		0.5	1.0	1.5	2.0	2.5	3.0	4.0
Spot size ( $1/e^2$ ) (μm)	Experiment	1.2	1.3	1.4	1.5	1.3	1.3	1.3
	Simulation	1.3	1.4	1.4	1.4	1.4	1.5	1.5

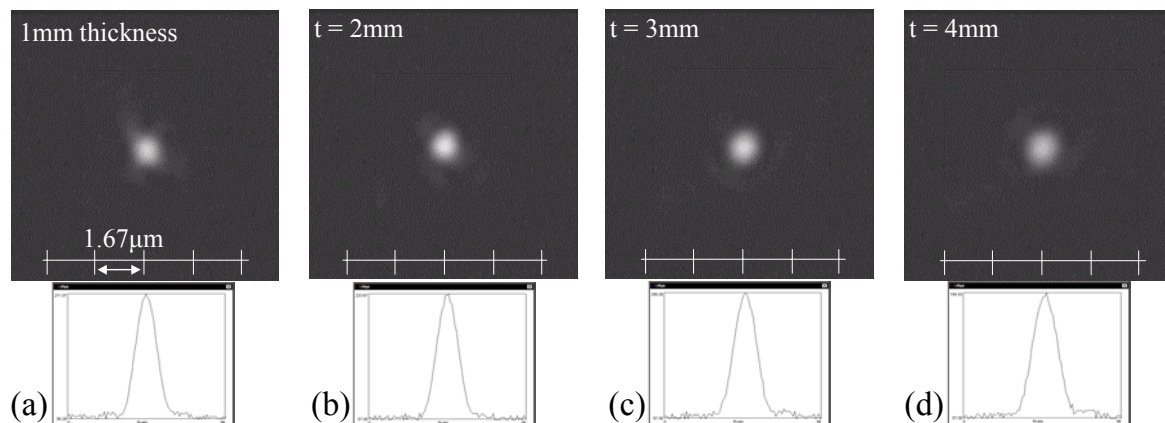


Figure 2.2.5 Video microscope images and ccd profiles of the focused spot through a) 1mm of material, b) 2mm of material, c) 3mm of material, and d) 4mm of material.

The video microscope uses of a 0.9NA microscope objective at a magnification of  $\sim 150\times$ . This is used to image the spot being focused by the conjugate changing optical system to a ccd camera for observation. Figure 2.2.5 shows the CCD images, and profiles, of the focused spot when using a 543nm HeNe as the collimated input to the system. The CCD images confirm the measurements made with the knife-edge measurement, and show very good spot size control through 4mm of material.

Next the conjugate compensation system is used for recording and readout of our 2-photon disks. Figure 2.2.3 shows the schematic of our recording and readout system. The recording laser is a 532nm Nd:Vanadate laser with a 6.5pSec pulse width, 76MHz repetition rate, and an average power of 5W (peak power of 28KW). The recording laser is modulated with an AO modulator, expanded, and then focused to a given layer by the conjugate compensating optical system. Single-tone data tracks are recorded with compensation at layer depths of 0.5mm-2.5mm in depth in layer steps of 0.5mm with the disk spinning at 30 Hz. A 635nm laser diode with 0.5mW of power is used to excite the fluorescence within the recorded volume. The fluorescence is relayed to a Hamamatsu R7400U-02 PMT and the resulting signal is observed on an oscilloscope. The peak-to-peak value of the readout signal is compared at each layer when using the spherical aberration compensating telescope, and without compensation where only the Geltech 350240 objective lens is used.

Table 4: Material thickness and readout signal levels with and without spherical aberration correction.

Material Thickness (mm)	0.5	1.0	1.5	2.0	2.5
Readout signal with telescope p-p (V)	0.72	0.78	0.73	0.72	0.72
Readout signal without telescope p-p (V)	0.56	0.48	0.32	0.22	0.19

Table 4 shows the voltage level of the readout signal with and without spherical aberration compensation for the given layer. The data shows that the variation in signal level with the compensated system is less than 8% while the variation in signal level without spherical aberration compensation is over 65%. This shows that the conjugate changing optical system is balancing the accumulating spherical aberration from deep layers.

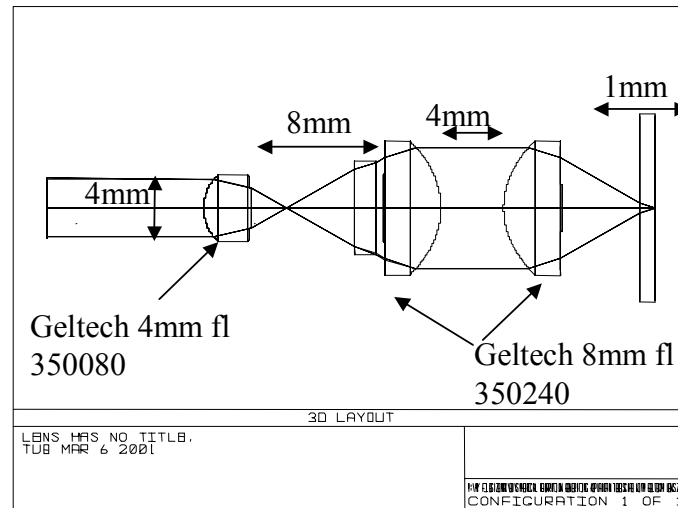


Figure 2.2.6 compact compensation system, using 0.5NA optics

For the compensating system shown in Figure 2.2.4 lens#1 must move 30mm axially to compensate for 10mm of disk thickness. Figure 2.2.6 shows an alternative system based on commercially available lenses where lens#1 moves only 1.3mm to compensate for 10mm of disk thickness. This reduction in axial movement is due to the numerical apertures of the compensating lenses and the effect of a fast system causing more rapid changes in marginal ray angles. Also the NA reduction in the system of Figure 2.2.4 changes from 0.5 to 0.3 over the 10mm of disk thickness, while that of the system in Figure 2.2.6 only changes from 0.5 to 0.4. By using an even higher NA compensating optical system the axial movement of lens #1 is further reduced.

Spherical aberration compensation is demonstrated in 2-photon recorded monolithic multilayer media. This shows that diffraction limited performance can be maintained throughout 10mm of disk thickness using a conjugate compensator system.

### 2.2.4 Recording experiment

Recording experiments to examine bit size using a 532nm green and 460nm blue laser are performed, and compared to simulation. Theoretical analysis of recorded bit size and cross-talk are presented and experimentally verified. Influence of NA on the recorded bit size, readout and recording efficiency in a 3-D multi-layer optical data storage system is analyzed. Using the 532nm laser experimental recording setup, layer pitch has been decreased. An integrated 16-

channel readout and recording system together with FPGA based signal-processing unit was demonstrated. Storage capacity of the 3-D multi-layer optical data storage system is analyzed.

At the present time the layer separation can be as close as 30 $\mu\text{m}$  without any significant crosstalk present in the readout signal from adjacent layers.

#### 2.2.4.1 Recorded bit size

The two-photon recording efficiency is scaled with the square of local laser irradiance. Because of this nonlinear response and sharp changing irradiance along the focused beam, the recording takes place only within a small volume around the focus of the laser beam. In the recording, the excited molecular distribution can be simply considered to be proportional to the square of the irradiance distribution of the recording laser beam. The recorded bit shape is modeled as:

$$P(x, y, z) = \alpha \times I^2(x, y, z) \quad \text{Equation 10}$$

$\alpha$ , a constant, is different from one type of molecule to another.  $I(x, y, z)$  is the laser beam irradiance. At focus, the laser is Gaussian-shaped, giving:

$$I(x, y, z) = \frac{I_0}{\omega_0^2 [1 + (\frac{\lambda z}{n\pi\omega_0^2})^2]} \exp\left\{ \frac{-2(x^2 + y^2)}{\omega_0^2 [1 + (\frac{\lambda z}{n\pi\omega_0^2})^2]} \right\} \quad \text{Equation 11}$$

where,  $I_0$  is the peak irradiance,  $\omega_0 \approx 0.5\lambda/NA$  is the radius of beam waist,  $\lambda$  is the wavelength and NA is the numerical aperture. An OPTISCAN<sup>8</sup> simulation shows the irradiance squared,  $I^2$ , distribution of a  $\lambda=460\text{nm}$ ,  $NA=0.5$  system to have bit dimensions of  $0.6*0.6*6\mu\text{m}^3$  as shown in Figure 2.2.7(a). Bit size is valued at the dimensions of  $1/e^2$  of the peak fluorescence. Figure 2.2.7(b) is the image of a real experimental recorded bit obtained with an Olympus fluorescence confocal microscope having dimensions of  $0.6*0.6*6.5\mu\text{m}^3$ . This particular bit was recorded with a frequency doubled Ti:Saph mode-locked laser (76MHz repetition rate, 200fs pulsewidth) with wavelength of  $\lambda=460\text{nm}$  and 0.5NA recording optics. Bit dimensions observed agree very well with the simulated value of the irradiance squared axial point spread function of the 0.5NA optical system.

From the bit shape model, we know that the recorded bit size depends on the wavelength and the NA. Figure 2.2.7(c) shows the experimental recorded bit with the 532nm laser and 0.5NA objective lens and the bit size is about  $0.7*0.7*7\mu\text{m}^3$  as expected. Figure 2.2.7(d) is the recorded bit with the 532nm laser and 0.75NA objective lens and the bit size is about  $0.5*0.5*4.5\mu\text{m}^3$  as expected. The bit density for this recording is 3.3Tb/in<sup>3</sup>. The recorded bits using the 532nm laser also agree well with the simulation. Figure 2.2.8 shows an axial cross-section of a multiple layer recording where several layers are recorded having layer separation of 12 $\mu\text{m}$ . Figure 2.2.8 shows clearly defined layers at the layer pitch of 12 $\mu\text{m}$ . Bleaching has been found to be significantly smaller using Blue laser recording laser also. The recording sensitivity using the 460nm wavelength blue laser is also  $\sim 10$  times more sensitive than the 532nm green laser based on the absorption spectra of the unwritten form. However, for all upcoming system

demonstrations the 532nm recording laser will be used as it has sufficient power to be able to record at 1Mb/s.

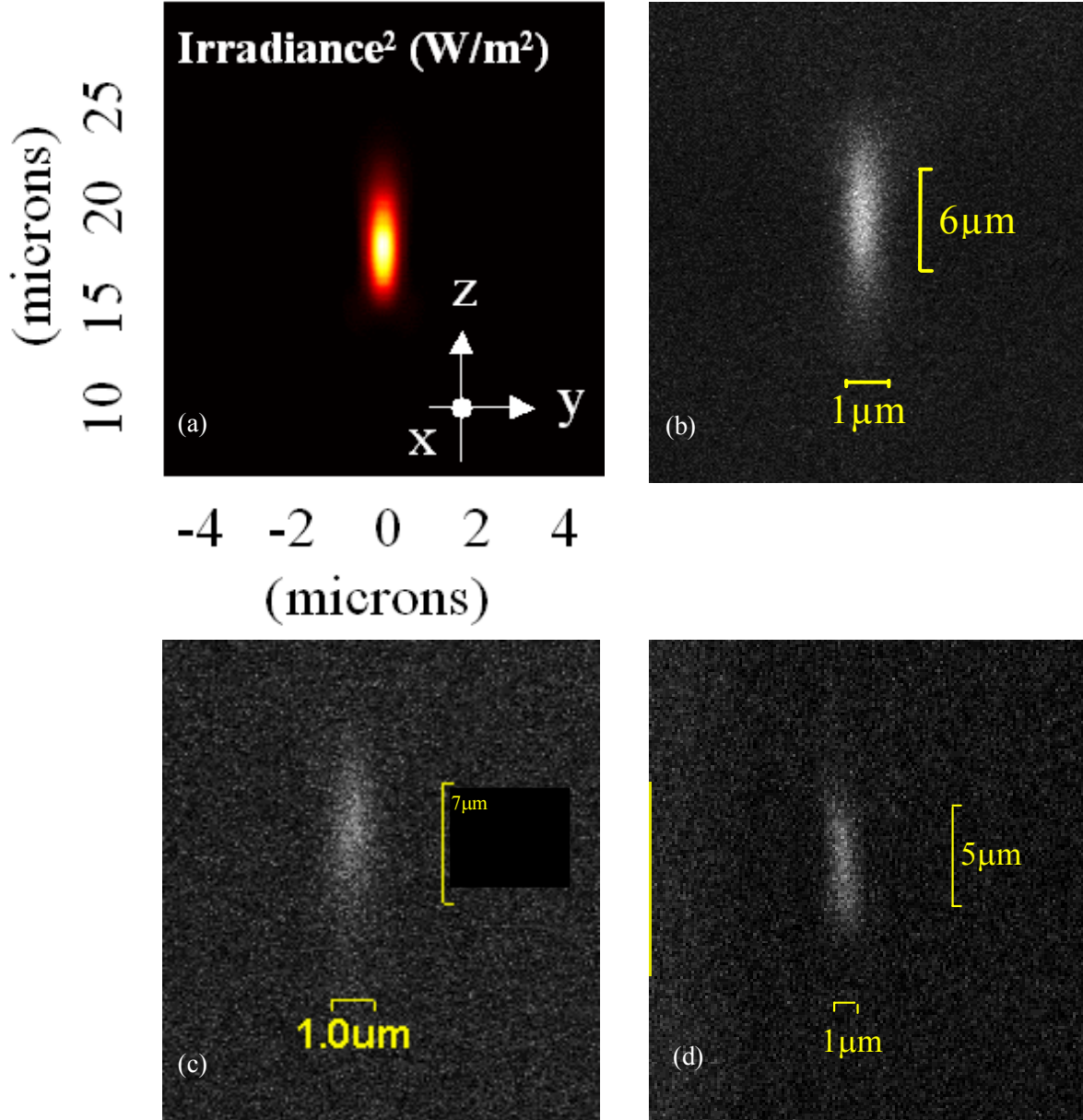


Figure 2.2.7. (a) physical optics simulation of 0.5NA axial PSF Irradiance<sup>2</sup> : 460nm@ 0.5NA, bit size: 0.6\*0.6\*6 μm<sup>3</sup>; (b) Recorded bit: 460nm@ 0.5NA, bit size: 0.6\*0.6\*6.5 μm<sup>3</sup>; (c) Recorded bit: 532nm@0.5NA, bit size: 0.7\*0.7\*7 μm<sup>3</sup>; (d) Recorded bit: 532nm@0.75NA, bit size: 0.5\*0.5\*4.5 μm<sup>3</sup> wavelength blue laser is also ~10 times more sensitive than the 532nm green laser based on the absorption spectra of the unwritten form. However, for all upcoming



system demonstrations the 532nm recording laser will be used as it has sufficient power to be able to record at 1Mb/s.

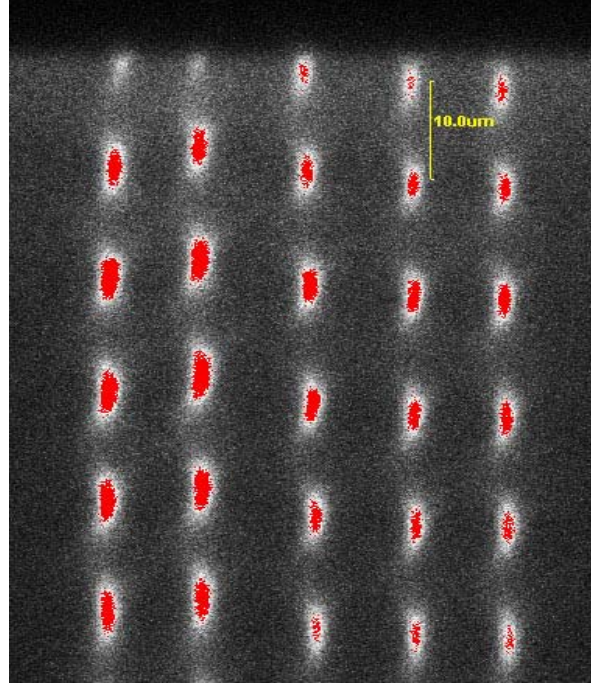


Figure 2.2.8. Blue(460nm) laser multi-layer recording

#### 2.2.4.2 Track pitch and aerial capacity

The fluorescence generated inside the disk is proportional to the convolution of the recorded bits volume and the illumination beam. The resolution of the readout system is related to the diameter of the illumination airy disk as well as the recorded bit dimensions, as cross talk from adjacent tracks and layers may cause errors. A confocal pinhole helps to decrease cross talk.<sup>3</sup> Figure 2.2.9(a) shows simulation results of cross talk between adjacent tracks in a 1X optical magnification system as a function of confocal pinhole size. Figure 2.2.9(b) is an experimental result with the 532nm and 0.5NA system. Different single tone patterns are recoded on adjacent tracks at a track pitch of 3µm. A 15µm pinhole is used in readout with a system magnification of 2.5X, corresponding to a 6µm pinhole in a 1X magnification system. The simulation and experimental results show that the cross talk is about 5% (-26dB).

The total areal capacity is expressed as:

$$C_{areal} = \frac{\pi(r_{max}^2 - r_{min}^2)}{l_{bit} \times w_{pitch}} \quad \text{Equation 12}$$

$r_{max}$ ,  $r_{min}$  are max and min recording radius of the disk,  $l_{bit}$  is the bit length and  $w_{pitch}$  is the track pitch. If a 1µm pinhole is used, the areal capacity of 5.25" 2-photon disk is approximately 0.7GB with 1.5µm track pitch.

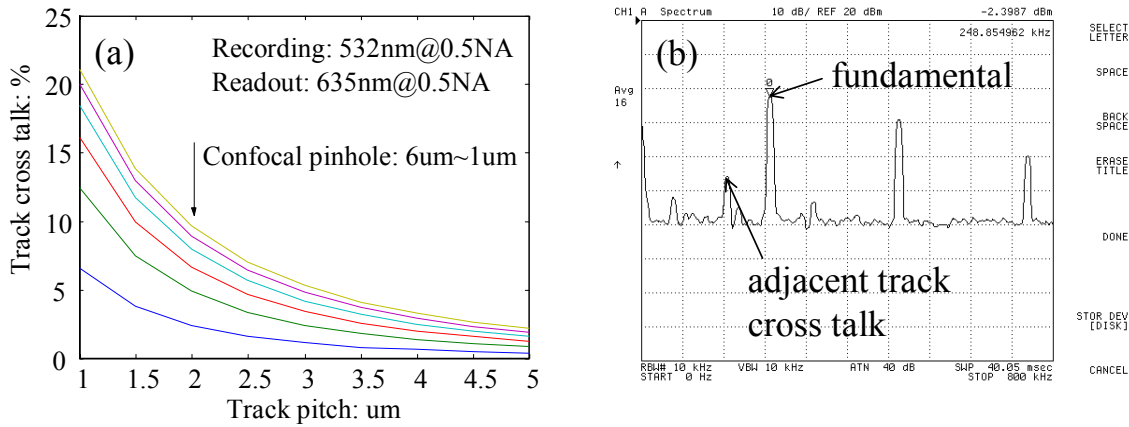


Figure 2.2.9.(a) Simulation of the tracks cross talk: recording  $\lambda=532\text{nm}$ ,  $NA=0.5$ ; readout  $\lambda=635\text{nm}$ ,  $NA=0.5$ ; (b) Experimental result

### 2.2.4.3 Layer separation and volume capacity

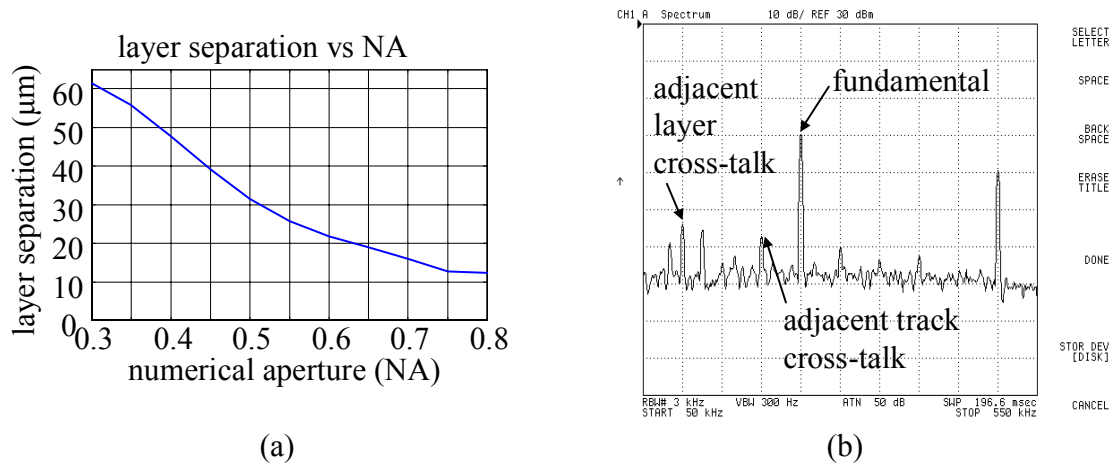


Figure 2.2.10. (a) Layer separation vs. NA (b) Experiment result

In a 3-D multi-layer optical data storage system, layer separation is another factor that influences the volume capacity. From analysis and experiments, the depth of the focus of the recording beam affects the length of the recorded bits and will influence the layer separation: the shorter the depth of the focus, the smaller the layer separation. A confocal pinhole also helps to decrease the adjacent layer cross talk. Figure 2.2.10(a) shows the experimental results of layer separation with different NA. The cross talk is set as 5%. Figure 2.2.10(b) is the spectrum plot from a spectrum analyzer of a multi-layer readout result. The recording

condition is: 532nm laser with 0.5NA objective lens, layer separation of 30μm and track pitch of 3μm. For readout, there is a 4X optical magnification, a DOE to achromatize the fluorescence<sup>4</sup> and a 5μm pinhole placed before the detector. The cross talk from the adjacent layer is ~5% (-26dB).

The number of layers that can be recorded is expressed as:

$$N_{\text{layer}} = \frac{T_{\text{disk}}}{S_{\text{layer}}} \quad \text{Equation 13}$$

$T_{\text{disk}}$  is the thickness of the disc;  $S_{\text{layer}}$  is the layer separation.

The volume capacity of a 2-photon 3-D optical data storage disk is:

$$C_{\text{total}} = C_{\text{areal}} * N_{\text{layer}} \quad \text{Equation 14}$$

For a 5.25" diameter 3mm thick disk, the capacity could be 70GB. In the experiments, a Hamamatsu R4900-02 PMT is used to detect the fluorescence. A custom designed CMOS 2-D detector array will be available soon for 2-D parallel readout experiments. This detector has nW sensitivity and MHz frame rate. The 2-D Detector layout architecture is carefully designed to increase the signal quality and decrease cross talk. A 3-D coding scheme will further decrease the cross talk.<sup>9</sup> By using these techniques, 140GB capacity is possible for a 5.25" diameter 3mm thick disk. Currently, a 1.5μm track pitch and 15μm layer separation is being tested.

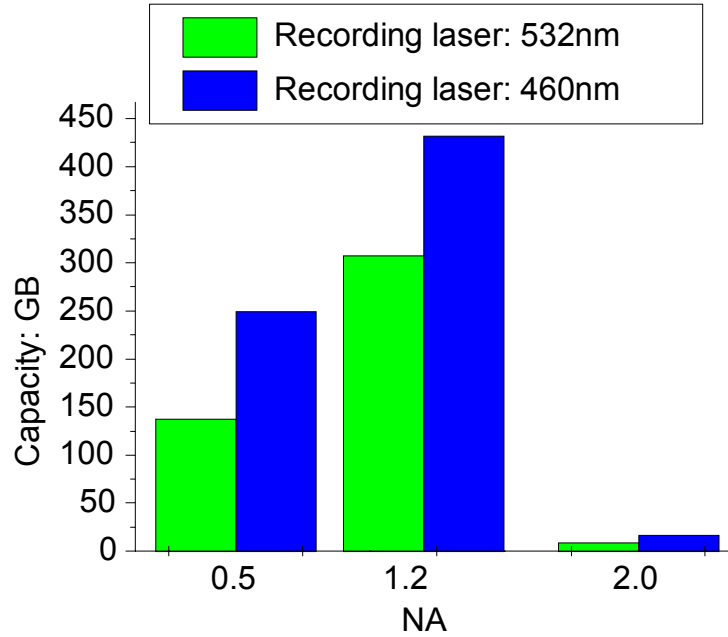


Figure 2.2.11. Capacity vs. NA

NA directly influences the capacity by virtue of the point spread function dependence on NA. A high NA objective lens reduces the track pitch and layer separation. The working distance

of the high NA lens should also be considered, as it will determine the total number of recorded layers possible. Figure 2.2.11 shows the capacity vs. NA. After depth compensation, the working distance of Geltech 0.5NA lens can be 3mm. Therefore, total volume capacity is about 140GB for 532nm recording and about 250GB for 460nm recording. For an Olympus MplanApo 1.2NA oil immersion lens, a smaller bit can be recorded, the working distance of this lens is 630 $\mu$ m; an estimated volume capacity is about 308GB for 532nm recording and 430GB for 460nm recording. If the NA is even shorter (such as 2.0NA), the working distance is too short to be multi-layer recording; the volume capacity is only about 10GB for 532nm recording and 17GB for 460nm recording. In order to increase the volume capacity, a tradeoff between high NA and working distance needs to be considered

### 2.2.5 Recording laser power dependence on NA

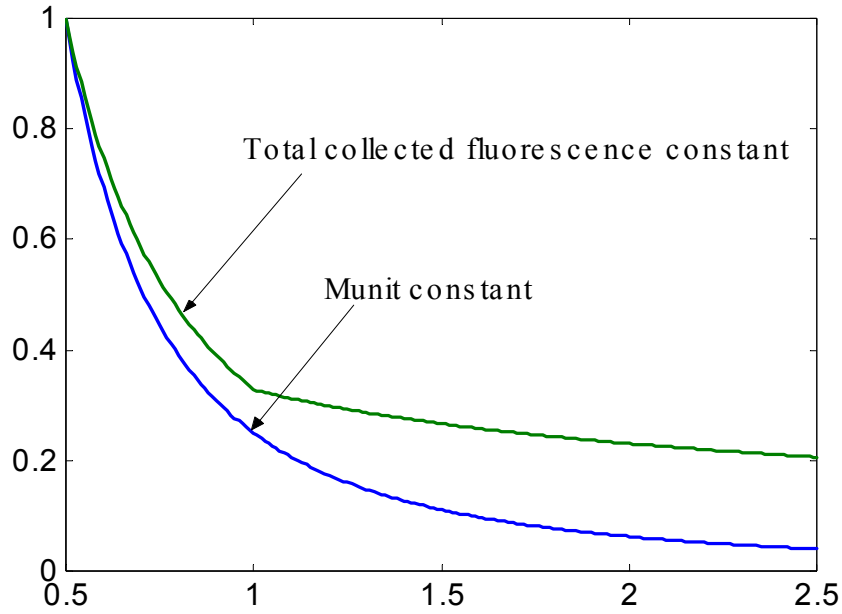


Figure 2.2.12. Normalized recording power vs. NA

The numerical aperture influences not only the recorded bit size and the collected fluorescence, but also the recording power. For 2-photon recording, the required peak power,  $P_{peak}$ , of the laser can be expressed as:

$$P_{peak}^2 = \frac{\pi^2 2h\nu \cdot M_{unit} \cdot (0.5\lambda)^4}{D_M \sigma T \cdot t_p f_{rep}} \cdot \frac{1}{NA^4} \quad \text{Equation 15}$$

here,  $h\nu$  is photon energy,  $M_{unit}$  is recorded molecules per unit volume,  $\lambda$  is recording wavelength,  $D_M$  is density of the original unrecorded molecules,  $\sigma$  is 2-photon cross section,  $T$  is recording time,  $t_p$  is the pulse width of recording laser,  $f_{rep}$  is the repetition rate of recording laser. Now consider that the recorded molecules per unit volume and recording time are constant when using the same repetition rate and pulse width laser a relationship between recording power and NA only is shown as Figure 2.2.12(blue curve). Now if the collection efficiency is considered to

maintain the total collected fluorescence constant at the detector, then the recording power vs. NA as shown in Figure 2.2.12(green curve) is obtained. All of the data are normalized at the recording power with the 0.5NA objective lens. This shows that by increasing the NA, the recording power may be reduced. For example, if a 1.0NA objective lens is used only 25% of the recording peak power is required relative to 0.5NA recording system.

## 2.2.6 Fluorescence collection efficiency

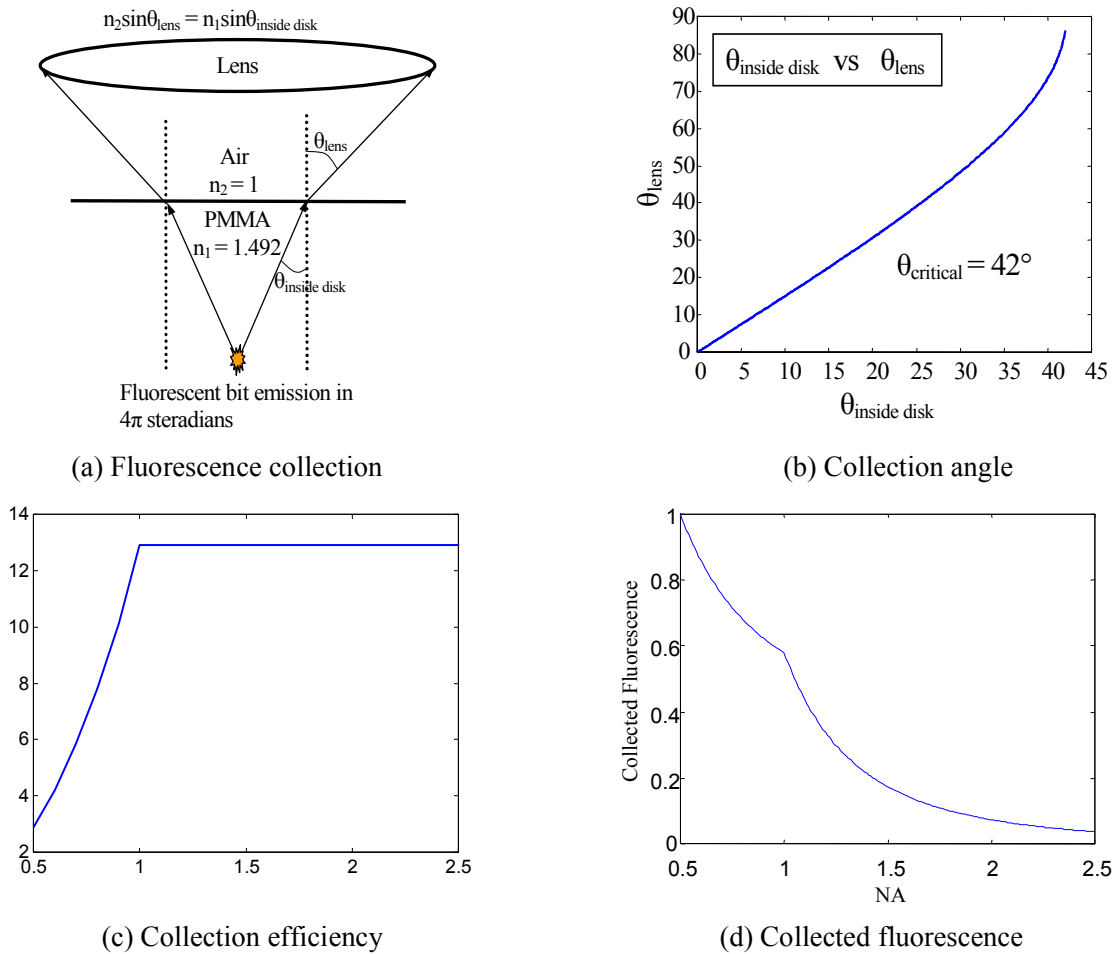


Figure 2.2.13 Fluorescence collection

During readout fluorescence is emitted in  $4\pi$  steradians. The objective lens collects only a small portion of the fluorescence, as shown in Figure 2.2.13(a). The substrate of the disk is PMMA,  $n_1=1.492$ , Figure 2.2.13(b) shows the relationship of the collection angles in the interface of the disk and air. The critical angle affects the maximum solid angle that can be collected. Total collection efficiency is the ratio of the collected solid angle to  $4\pi$ :

$$\eta_{Collection} = (1 - \sqrt{1 - (\frac{NA}{n_1})^2}) / 2 \quad \text{Equation 16}$$

here,  $NA = n_2 \sin \theta_{\text{ens}}$  is the numerical aperture of the objective lens. Figure 2.2.13(c) shows the collection efficiency for different NA. To first order we assume the collection efficiency is the same when  $NA \geq 1$ , neglecting any evanescent field coupling that would actually increase the coupling efficiency. Total collected fluorescence is defined as:

$$F = \eta_{collection} \cdot V_{bit} \quad \text{Equation 17}$$

here,  $V_{bit}$  is the recorded bit size. Figure 2.2.13(d) shows the collected fluorescence vs. NA. The data is normalized with the data at 0.5NA. After normalization, the relationship is approximately the same for 532nm and 460nm recording wavelengths. This analysis assumes the fluorescence emitted per unit volume is the same. When  $NA \leq 1$ , the collected fluorescence is affected by the increasing of the collection efficiency and the decreasing of the bit size. When  $NA > 1$ , the decreasing of the collected fluorescence is mainly caused by the smaller bit size without taking into account evanescent field coupling.

## 2.2.7 Data formatting, readout and signal processing

The disk formatting and signal processing have been implemented and demonstrated in several demos and the portable Disk Reader 3 and most recently the portable Worm reader. Most recently a 16-channel parallel readout system was demonstrated that included a software demodulation with a computer interface. Figure 2.2.14 shows the typical one-channel signal-processing diagram. Figure 2.2.15 shows the signal quality measurements based on single tone and (2,7) RLL (Run Length Limited) modulated random data tracks. The measurement results show comparable performance to other conventional optical memory.

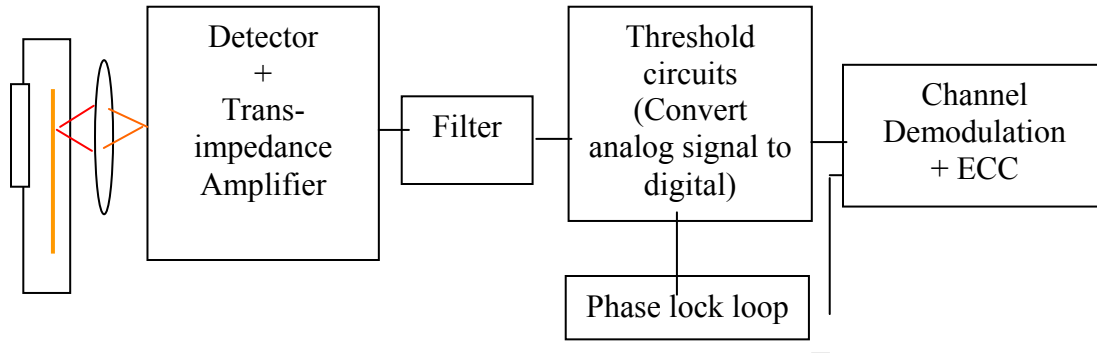
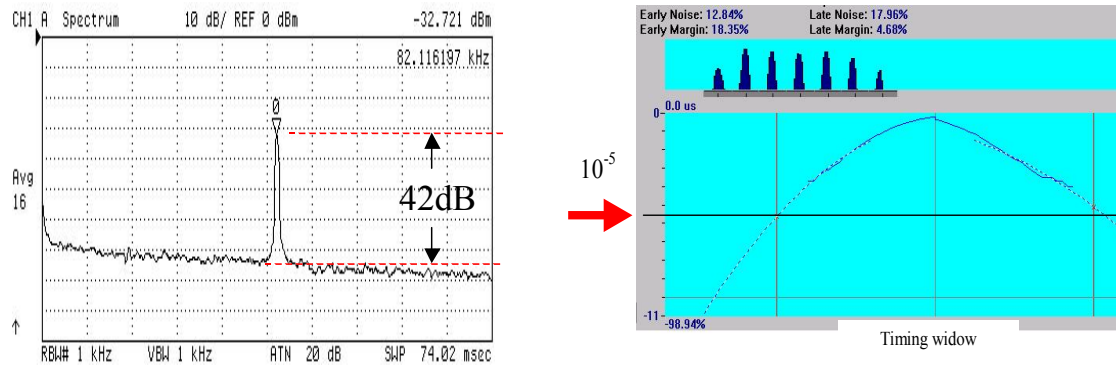


Figure 2.2.14 The readout channel function diagram



Reed-Solomon (15,9) ECC (error correction coding has been selected and implemented to minimize the data errors).

### 2.2.8 System integration

The recording, a 1 x 16 in-plane parallel readout system, and an FPGA based encoding circuit with a computer interface has been integrated together as a demo. The system is a table demo capable of a 1Mb/s recording rate and a 16Mb/s readout rate.

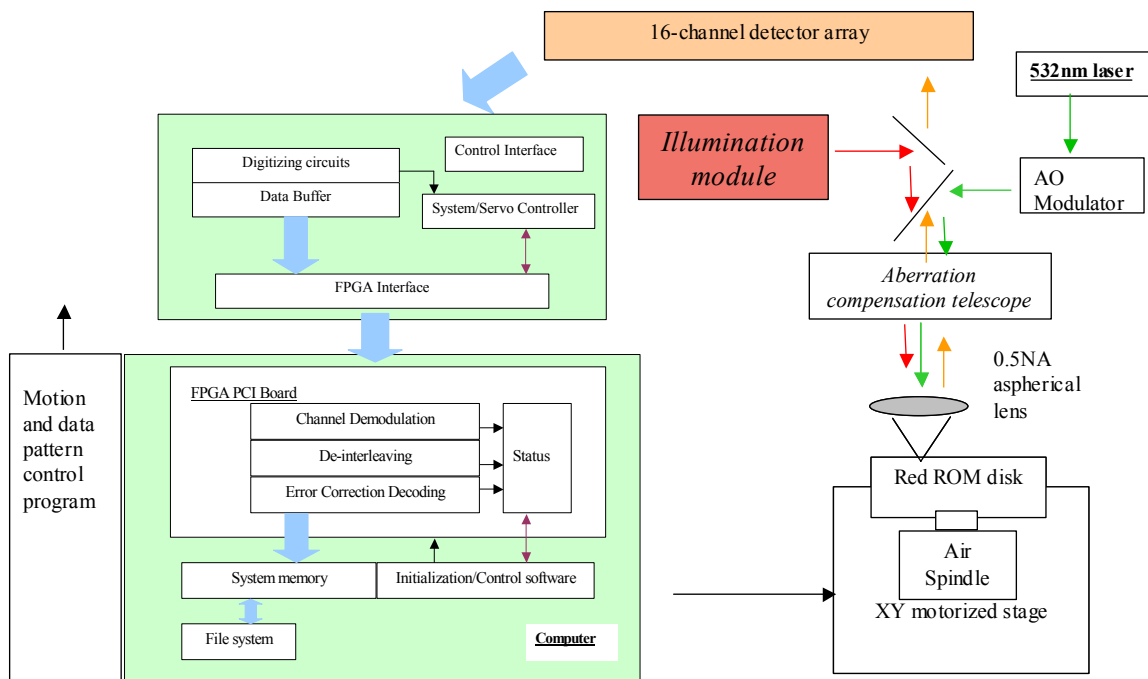


Figure 2.2.16. Block diagram of WORM system.

The detector data signals are demodulated by a FPGA based decoding circuitry and then interfaced to a computer to display the output data and then compared to what was actually recorded to observe any errors. This characterization is ongoing. Integration of a 64 channel parallel readout system is presently underway that will be capable of a 1Mb/s recording rate and a 64Mb/s readout rate.

### **Summary of accomplishments: for Recording optics**

- Experiments show feasibility to record 100 data layers into a 3mm thick disk, 5.25" diameter, with 140GB capacity. With the 3.5" diameter disks that are being made a 22GB Capacity is reached.
- material supports sub-micron size bits
- Two-photon recording has achieved 1.2 $\mu$ m bit radial size with 15 $\mu$ m bit depth using green 532nm recording, also achieved is 0.7 $\mu$ m bit radial size with less than 10 $\mu$ m bit depth using blue 460nm recording.
- recording speed is  $\sim$  1Mbits/Sec/channel (532nm) recording laser requirements, 6ps pulsewidth, 75MHz repetition rate, 10kW peak pulse power ( $\sim$ 1.5W average power).

## **2.3 Readout Optics**

In this section, we present the theory, simulations, and experimental results of in-plane parallel readout diskstand systems that we have built and used in our WORM system demonstration. The experimental result presented is from a 16 parallel data channel readout system that reads 16 radial data tracks in parallel from a two-photon recorded monolithic multilayer disk.

The recorded bits by two photon absorption in the multilayer disk are read by fluorescence when excited by single photons absorbed within the written spot volume. The conventional approach to achieve high readout data rates in single-layer disk media data storage systems is to decrease the physical bit size and increase the velocity at the head/media interface. Further increase in data throughput may be achieved by parallel readout architectures that read information across a number of data tracks simultaneously within a given data layer.

Design, development and prototyping of advanced recording and playback optical systems that exploit the parallelism available in volumetric media and utilize more of the limited FOV of inexpensive optics is a topic of active development.<sup>10,11,12</sup> In conventional CD and DVD optical data storage systems the data channel is serial. Exploiting the potential of parallelism that exists in optical systems can increase data throughput. One way is to fan the readout beam into several beams by using a diffraction grating.<sup>13</sup> This results in a linear  $1 \times N$  array of focused illumination spots oriented radially, increasing the total data throughput by N times that of a serial channel device. An astigmatic line of illumination may also be used to read out  $1 \times N$  multi-tracks.<sup>14</sup> An alternative to the arrangement of  $1 \times N$  focused spots in a radial line is to arrange them in a two dimensional spot array. This will not increase data throughput, but can reduce crosstalk and aid in matching the illuminated data tracks to a detector array by increasing the center-to-center pitch of the illumination spots. Employing a large number of laser beams using a lenslet array or a single high NA annular-field objective lens can generate a two dimensional spot array.<sup>15</sup> All of



these architectures achieve parallel readout within a single layer. However, there is a limit as to how large N can be due to the limited object field of the objective lens. Call/Recall, Inc. has developed and demonstrated a parallel readout architecture where data tracks are read in parallel across multiple layers in depth, as well as across a number of radial tracks.<sup>16</sup> The concept is to arrange the bit oriented 2-D data page array on a tilted plane with respect to the optical axis so that multiple tracks (1×N) within multiple layers (M) are readout simultaneously. The data plane format is organized with 1×N multiple tracks being read out at a given layer inside the material with M more data layers being readout at the same radial location. Parallelism offers the potential for much higher data rates compared to serial readout. For example, if each individual data channel within a 1 x 16 array format is operating at 1Mb/s a total data rate of 16Mb/s is achieved. Following this direction a 1×16 readout system is designed and built to simultaneously excite fluorescence of 16 data tracks on a single layer for a 16Mb/s data channel.

The readout of multiple data channels increases data throughput. The illumination optics generates light that is coupled inside the disk to excite fluorescence from written data bits across parallel data channels. The collection optics gathers the fluorescent emission of the parallel data channels and converts the fluorescent photons to a voltage signal to be processed by the read channel electronics. An experimental evaluation of a 1 x 16 in plane parallel readout system is demonstrated.

### 2.3.1 Numerical aperture tradeoffs

A higher NA is desired in order to resolve finer detail. This also leads to the highest possible total storage capacity for the disk and the most fluorescence photons collected. The drawback of a high NA is the increased aberration introduced when focusing through the thick media, which in turn adversely changes the MTF by lowering contrast when compared to the unaberrated system.

$$W_{040} = -\frac{1}{8} \left( \frac{n^2 - 1}{n^3} \right) NA^4 t \quad \text{Equation 18}$$

Equation 18 describes the spherical aberration,  $W_{040}$ , introduced by a plane parallel plate where n is the index of refraction (typically 1.48 for PMMA), NA is the numerical aperture, and t is the disk thickness. Observe the 4<sup>th</sup> power dependence upon the numerical aperture that is characteristic of spherical aberration, and the linear dependence upon the disk thickness.

$$\eta_{\text{lambertian}} = \frac{\sin^2 \theta}{2} = \frac{NA^2}{2} \quad \text{Equation 19}$$

$$\eta_{\text{spherical}} = \frac{1 - \cos \theta}{2}$$

Equation 19 describes<sup>17</sup> the collection efficiency of the objective lens for the fluorescent data modeled as a lambertian emitter,  $\eta_{\text{lambertian}}$ , and modeled as a spherical emitter,  $\eta_{\text{spherical}}$ . The lambertian model has a quadratic dependence upon the numerical aperture and the spherical model is slightly more complicated.

NA	$\eta_{\text{lambertian}}$	$\eta_{\text{spherical}}$	$W_{040}$
0.3	4.5%	2.3%	6.4waves
0.5	12.5%	6.7%	49.4waves

Table 5

Table 5 illustrates the tradeoff for the increased collection efficiency with increased NA for an increase in spherical aberration for a 10mm thick disk.

### 2.3.2 Linear spot array illumination and experiments

As the basis of spot array illumination, it is important to know how many channels could be illuminated by a linear spot array and read out in parallel. Figure 2.3.1 shows the real system Zemax unfolded layout that is being used in the experiment.

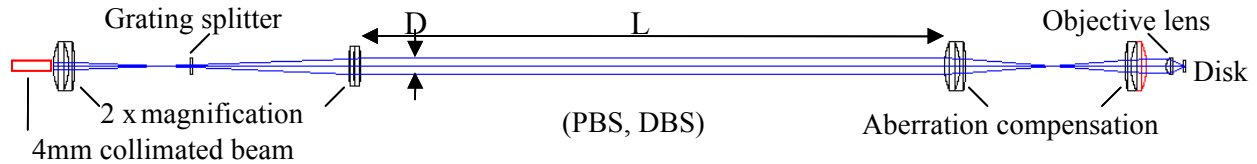


Figure 2.3.1 Zemax layout of experimental linear spot array illumination system

A 5mw, 635nm Blue Sky Research's CircuLaser™ laser diode module is used as the illumination light source. The 4mm collimated beam is expanded to 8mm by a 2× telescope to match the aperture of the objective lens. A diffractive grating is placed in the telescope for linear spot array generation and the spot pitch is adjustable by moving the grating back and forth. The split beams pass through a 1× aberration-compensation telescope and are focused into the disk by a 8mm Geltech 350240 aspheric lens to illuminate data tracks. Figure 2.3.2 shows point spread functions and spot diagrams of the illumination spots at different diffraction orders simulated by Zemax. The spot pitch is 5μm and the disk thickness is 1mm.

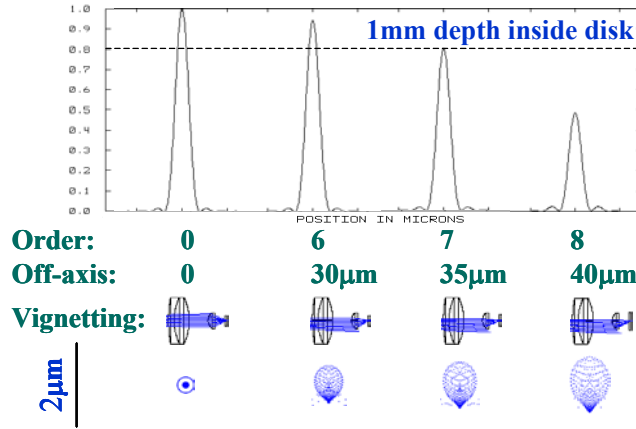


Figure 2.3.2. Illumination spots at different diffraction orders

As shown in Figure 2.3.2, vignetting and coma dominate how many channels could be achieved in line. At higher orders (more off-axis), coma becomes bigger resulting in lower Strehl ratio, vignetting becomes dramatic as well. So readout signals at higher orders are a little worse than those at lower orders as shown in Figure 2.3.3. With bigger than 80% Strehl ratio and more than 80% power passing through the stop, the maximum linear channel number that can be illuminated in the current system is sixteen.

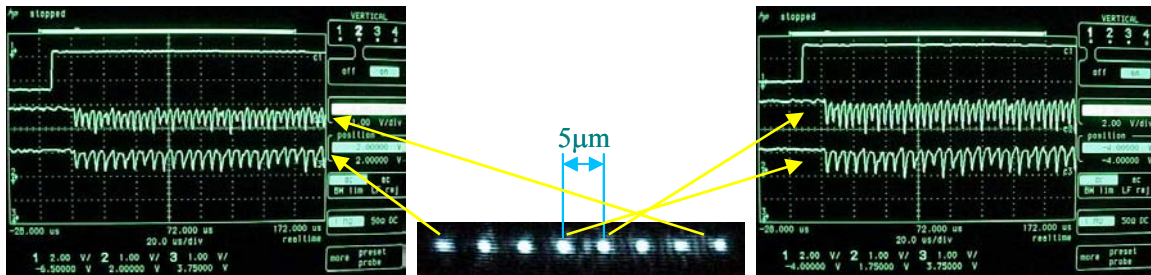


Figure 2.3.3. Readout signals at different diffraction orders

Table 6. Channel numbers achieved with different system parameters

Disk thickness (mm)	D (mm)	L (mm)	Field view (μm)	Channel number (5 μm pitch)
1	8	300	70	15
1	8	80	90	19
1	6	80	110	23
0.3	6	80	140	29

Adjusting system structure will reduce vignetting and improve channel number. Table 6 shows channel numbers that could be achieved with different system parameters. By reducing L, the distance from the multiple beam generator to the multi-element objective lens(described in the writing optics section), more possible data channels are accommodated. Alternatively, another method to improve channel number is to reduce the track pitch, as long as there is enough system

magnification to match the detector array. For example, 36 channels could be achieved when the field view is 140 $\mu$ m and the track pitch is 4 $\mu$ m.

Figure 2.3.4a) shows the mechanism of the collinear point-by-point illumination module that uses a diffractive grating to split a collimated input beam into a  $1 \times 16$  array of beams having approximately equal power and different transmission angles. These beams are focused by the objective lens inside the disk generating 16 illumination spots. A high degree of uniformity of optical quality among all the focused spots is achieved for keeping the readout characteristics as uniform as possible. The spot pitch is determined by both parameters of the grating and the focal length of the objective lens. In the experiment, a diffractive grating (Thorlabs G100K  $1 \times 16$  fanout) and a high NA aspheric lens (Geltech 350240 8mm focal length) are used to generate a  $1 \times 16$  spot array with  $10\mu\text{m}$  pitch.

Figure 2.3.4(a) Schematic drawing of in-plane parallel illumination showing experimental CCD image of  $1 \times 16$  illumination spot array (b) a parallel readout system based on in-plane illumination and a PMT array

The same objective lens used to generate the focused spot array collects the emitted fluorescence. Next the data tracks are imaged to match the pitch of the PMT array. The pitch of the 1 x 16 channel parallel PMT array (Hamamatsu) in the experiment is 1mm. If the pitch of the data bits is 10  $\mu\text{m}$ , a 100 $\times$  magnification is required. The 100X magnification is split into 2

imaging steps. With a magnification  $m_1$  obtained at the focal plane of the first imaging lens. The second imaging lens provides another magnification of  $m_2$ .  $m_1$  and  $m_2$  are 2 and 50 respectively resulting in a net magnification of 100.

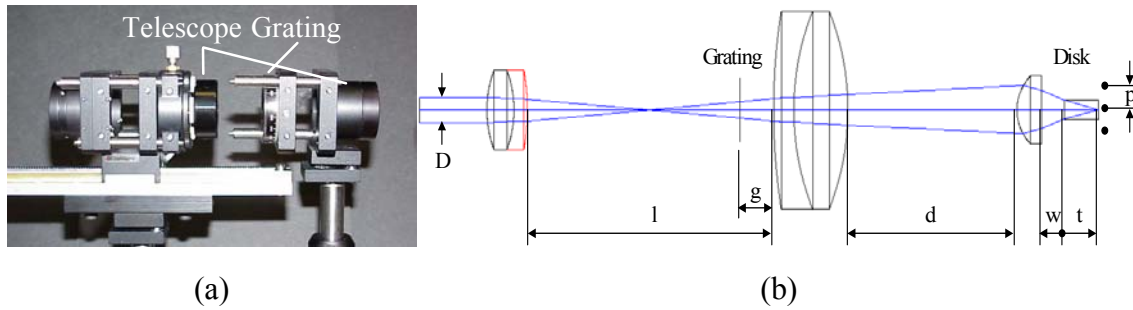


Figure 2.3.5(a) In-plane illumination module and (b) its schematic drawing

Figure 2.3.5 shows the illumination module and its schematic drawing. The diffractive grating (MEMS Optical G100K) is placed in the divergent or convergent beam path between the two lenses (Newport GAC020 and GAC040) of the telescope.

Figure 2.3.6(a) shows a CCD image of the  $1 \times 16$  fluorescent spots at the pmt detector plane corresponding to the  $1 \times 16$  illumination spots shown in Figure 2.3.4. The fluorescent spots are very well defined and match the pmt detector pitch of 1mm. Figure 2.3.6(b) shows typical ppm encoded signals from four of the detectors. The signals show very good uniform quality across the 16 channels.

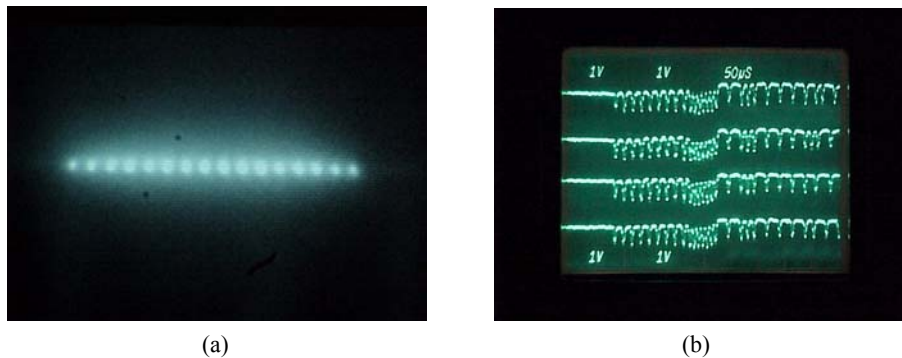


Figure 2.3.6. (a)  $1 \times 16$  fluorescent spot array at the detector plane as imaged by a CCD camera (b) 4 typical signal outputs from the  $1 \times 16$  pmt detector array.

The recording and a  $1 \times 16$  in-plane parallel readout system have been integrated together as a demo. The system is a table demo capable of a 1Mb/s recording rate and a 16Mb/s readout rate. This optical system is the basis for the portable worm demonstration unit that is a deliverable of this program.

## **Summary of accomplishments: Readout Optics**

- Fluorescence signal readout requires high sensitivity detectors, but readout signal quality is acceptable for channel speeds at  $\sim 1\text{Mb/Sec}$ .
- FPGA decoding system for 16channel readout is operational
- Track and layer crosstalk for given layer and track pitch have been shown to be  $< 30\text{db}$ .
- Channel readout speeds of  $2\text{Mb/Sec}$  have been demonstrated

## **2.4 Servo**

Experimental testing of a servo error signal detection technique for 2-photon recorded monolithic multilayer material is realized. A standard CD voice-coil actuator follows a fluorescent data track based on an error signal generated from the fluorescence itself. A review of relevant servo techniques is discussed. Spindle motor characteristics are reviewed and selection of spindle motors for experiments and demonstrations is discussed. Layer and track addressing is reviewed as well as a servo while writing architecture.

### **2.4.1 Outline of problem**

The servo task can be broken up in to categories:

- 1) generation of the error signal
- 2) signal processing
- 3) Actuation

To generate an error signal a dedicated servo detector is used that monitors some distribution of light reflected from the disk. The servo detector can be a quadrant detector that enables the photo-generated signal current from each quadrant to be combined algebraically and form an error signal. The error signal is then processed and electronically fed back to an actuator that moves accordingly to minimize the error signal. The response of the actuator must be able to follow the errors encountered in the system or the actuated element will not move to compensate and errors will result. If the error bandwidth falls within the servo bandwidth the actuator will compensate for these errors, however any errors outside the bandwidth of the servo will not be compensated for.

Another aspect is the addressing of tracks and layers and physically finding them in the disk. This could be done either in a closed loop or open loop fashion. In a closed loop fashion there is prerecorded information at varying depths and radial locations that identify the radial and depth position to the channel electronics. An open loop scenario could be a look up table in the servo electronics that tells the actuators to move to the desired depth and radial position based on deterministic quantities.

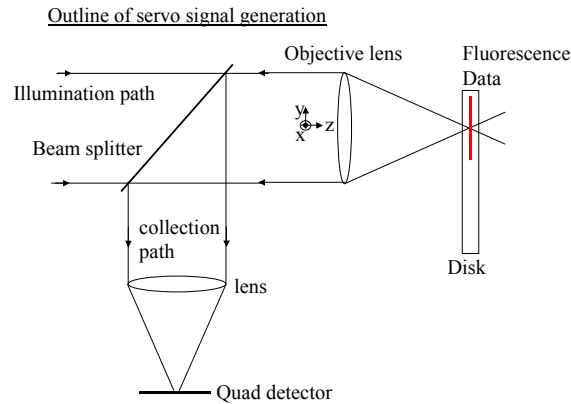


*Figure 2.4.1 Optical system showing the objective lens collecting the light and lens focusing to a segmented detector (typically a quadrant detector) that provides signals that may be algebraically combined to form an error signal for controlling the position of the objective lens*

## 2.4.2 Review of relevant servo techniques

Figure 2.4.1 shows a generic optical system consisting of the fluorescent data line object, objective lens, a beam splitter, and a lens to focus to a segmented detector that is typically a quadrant detector. Schemes for focus and push-pull tracking servo signal generation were analyzed. The two schemes are astigmatic focus, and wax-wane focus.

Astigmatic focus uses a lens with astigmatism built in so that as the objective lens moves to either side of focus the light distribution on the quadrant detector becomes a line as shown in Figure 2.4.2. The line rotates by  $90^\circ$  from one side of focus to the other. The focus error signal (FES) is obtained algebraically by subtracting the diagonal sums. The tracking error signal (TES) is obtained by subtracting the left and right halves of the quad detector. Astigmatic focus is straightforward to implement experimentally. Disadvantages include the need of an astigmatic lens in front of the servo detector, and the loss of light in the gaps of the quadrant detector.

Wax-wane focus uses a standard lens so that as the objective lens moves to either side of focus the light distribution on the quadrant detector becomes either a larger or smaller circle as shown in Figure 2.4.3. The FES is obtained by subtracting the upper and lower halves of the quad detector, and the TES is obtained as stated above. Wax-wane focus is straightforward to implement experimentally and is a good standard method. There is no need for the additional astigmatic lens, however the circle of light on the detector does need to be decentered.

### Astigmatic focus and push-pull tracking

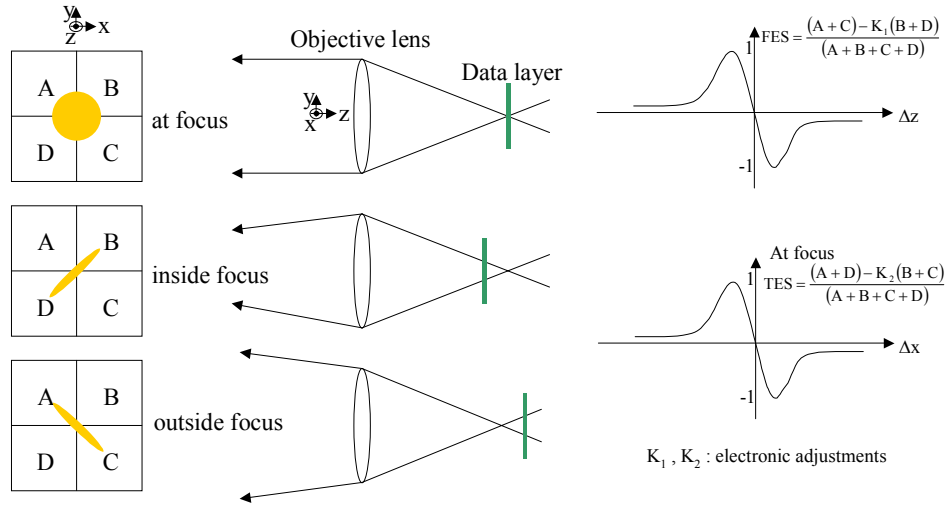


Figure 2.4.2 Outline of astigmatic focus and push-pull tracking. The light distribution on the quad detector is shown when the lens is in focus and on either side of focus. The focus error signal (FES) is obtained by subtracting the diagonal sums and the tracking error signal (TES) is obtained by subtracting the left and right halves.

### Wax-wane focus and push-pull tracking

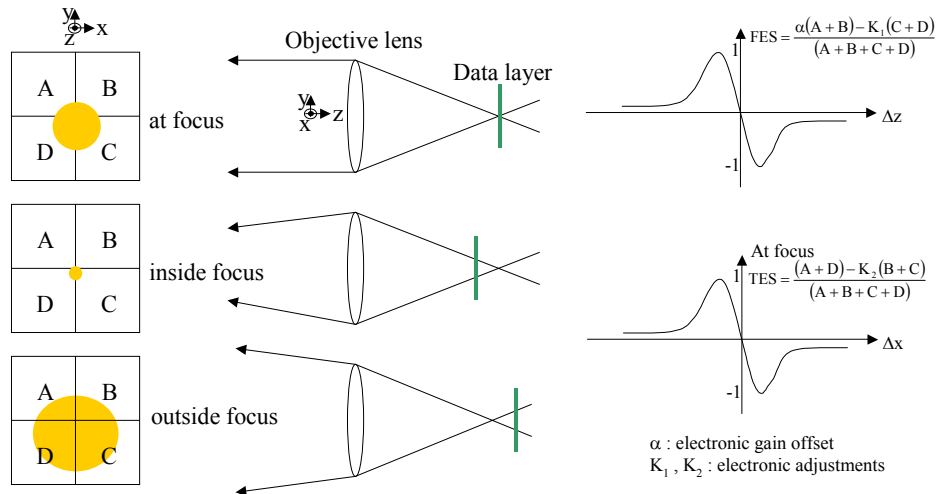


Figure 2.4.3. Outline of wax-wane focus and push-pull tracking. The light distribution on the quad detector is shown when the lens is in focus and on either side of focus. The focus error signal (FES) is obtained by subtracting the upper and lower halves and the tracking error signal (TES) is obtained by subtracting the left and right halves.



### 2.4.3 Servo error signal generation for 2-photon recorded monolithic multilayer optical data storage

A servo teststand was built that allows different servo signal generation methods to be tested. Voice coil actuators were used in these experiments. Standard CD type voice coil actuators available from replacement part distributors provide both fine focusing and tracking movements. The depth and radial addressing task will need to be done with lead screws, or motorized stages, as the focus range on these CD actuators is only  $\sim 2\text{mm}$  and the tracking range  $\sim 1\text{mm}$ .

A high capacity volumetric optical storage approach being developed at Call/Recall, Inc. uses 2-photon absorption techniques to record marks and layers at arbitrary locations throughout a monolithic thick plastic disk, which are subsequently read by single photon excitation and fluorescence (see Figure 2.4.4<sup>2</sup>) While this approach offers the potential of high effective areal densities and high per-disk capacities in low cost removable disks, unique challenges exist for the servo control of the objective lens. In the thick isotropic homogeneous media being used for multi-layer readout<sup>18,4,19</sup> each data layer has a zero background reflectance and no land/groove structure. This makes the use of standard servo error signal generation techniques that use spot shape features and groove structures (i.e.- astigmatic focus, and push-pull tracking<sup>6,20</sup>) difficult to implement. One promising technique that may be used in 2-photon-recorded fluorescent media is to directly use the readout signal strength in a push-pull focus and push-pull tracking architecture shown in Figure 2.4.5.

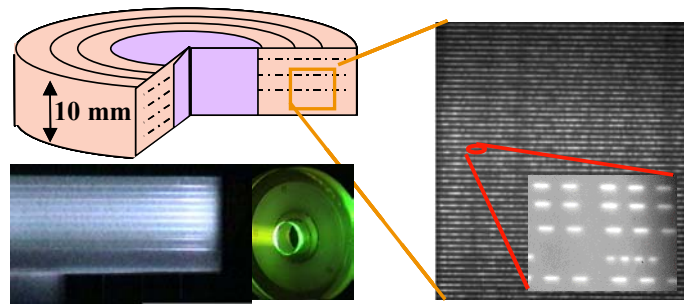


Figure 2.4.4. Two-Photon-recorded monolithic multilayer disk concept.

The lateral dimension and longitudinal dimension of the recorded bit depends upon the recording optics.<sup>8</sup> The fluorescent spot shape and power level changes more slowly in the focus direction due to the longitudinal dimension of the recorded mark. Two fluorescent spots are used to generate the FES in order to provide a bipolar electrical signal used for directional sensing of the voice-coil actuator position. The two illumination spots are slightly defocused from each other straddling the middle of the recorded mark as shown in Figure 2.4.2, this is similar to outrigger tracking common in optical tape systems. The fluorescent light distribution on two detector cells is shown when the lens is in focus and on either side of focus. When the lens is in focus the same amount of fluorescent power is incident upon both detector #1 and detector #2. When the lens is inside focus the fluorescent power level on detector #1 is reduced relative to the fluorescent power level on detector #2, and the situation is reversed when the lens is outside focus. The FES is obtained by subtracting the two individual detector signals. The associated focus servo electronics compensates the current in the voice-coil actuator to maintain the power

balance between the detectors. A similar approach is used for tracking error signal (TES) generation, where the left and right halves of the bi-cell detector #1 are subtracted. When the lens is on track the power levels on the two halves of detector #1 are equal, and the levels become unbalanced when the lens moves off track. Tracking servo electronics adjust the voice-coil actuator current to reestablish the power balance between the two detector #1 cells. Some disadvantages to this approach are that a large detector magnification is needed if the gap size of the bi-cell detector is large. Also, errors may accumulate if using this technique for writing where a track is recorded and then the next recorded track is slaved to this previously recorded track being used for servo. Another disadvantage is the illumination spots may not be in the plane of best focus resulting in slight decrease in signal resolution and/or level. Some advantages are that the disk does not need to be preformatted as in a sampled servo approach where the entire disk volume is preformatted with wobbled marks in depth and radially. Also, the data layers do not need any special groove structures which simplifies fabrication of massively multilayer (hundreds of layers) media.

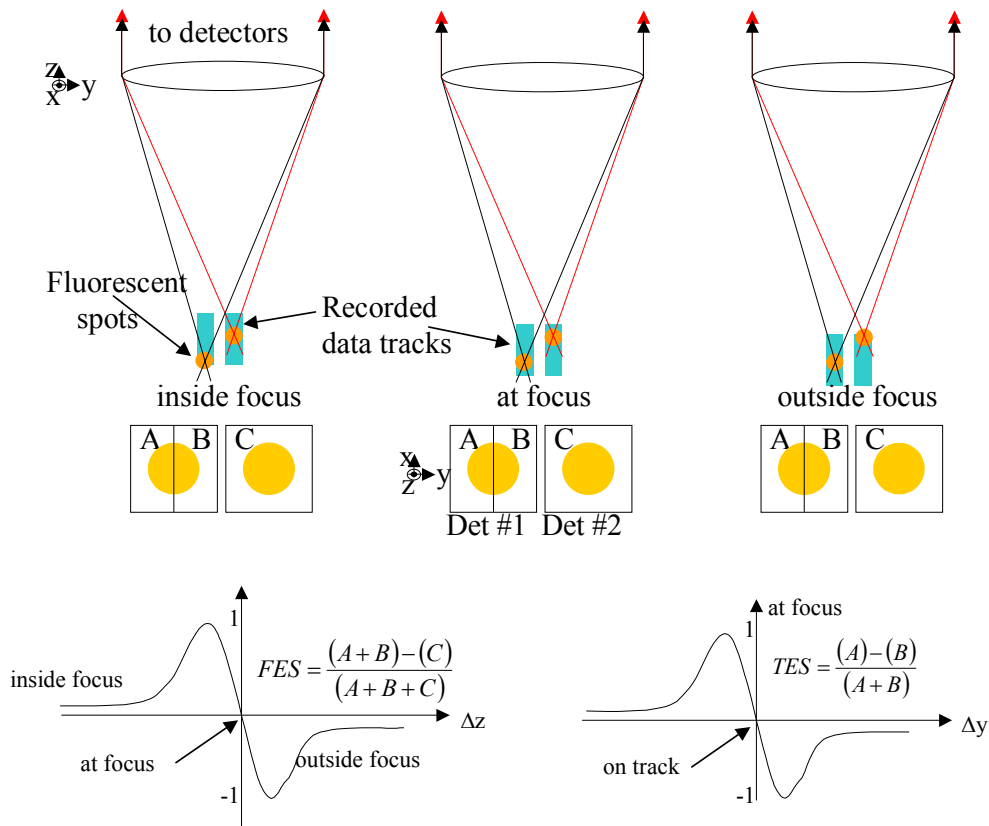


Figure 2.4.5 Outline of push-pull (out-rigger) focus and push-pull tracking error signal generation. Fluorescent light distribution on two detectors shown when lens in focus and on either side of focus. Focus error signal (FES) obtained by subtracting two individual detector signals, tracking error signal (TES) obtained by subtracting left and right halves of bi-cell detector.

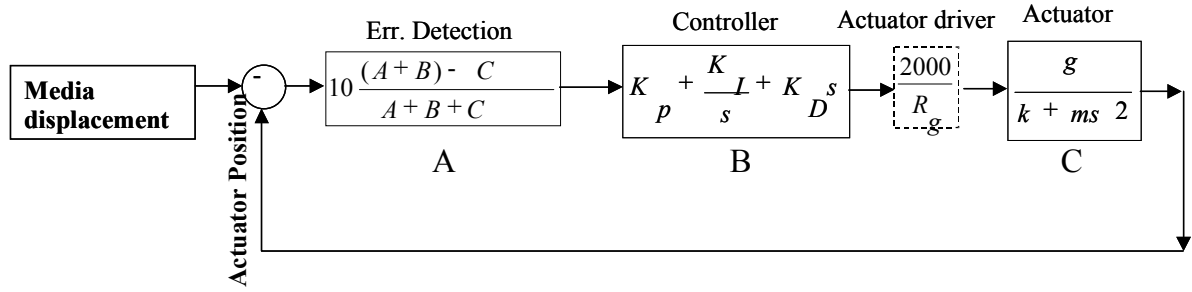


Figure 2.4.6. Block diagram of the closed-loop focus servo system

The flow chart in Figure 2.4.6 shows the composition of a closed-loop servo system in the absence of any noise sources. The sensor generates the error signal proportional to the residual positional error from the algebra circuits. The electronic control circuit and actuator driver chip (Allegro A8932clwa voice coil driver) translate this signal into motion of the actuator that minimizes residual error.

The residual error of this system can be simply expressed as,

$$\varepsilon = \xi / (1 + H) \quad \text{Equation 20}$$

where  $\xi$  is either the axial or radial run out, and  $H$  is the system gain given by  $H_A \cdot H_B \cdot H_C$ .  $H_A$  is the contribution to the system gain from the error signal generation and is proportional to the slope of the “S” curve in the linear region. From equation 1, if the gain  $H$  is increased the residual error is minimized.  $H_B$  is the contribution to the system gain from the lead/lag controller circuit. Care needs to be taken to select the  $|H|_{\text{cross}}=1$  crossover frequency where the phase of  $H$  at that point is  $< 180^\circ$ , otherwise the denominator value goes to zero with the result that the servo becomes violently unstable. The design of the servo circuitry has three major tasks; 1) algebra circuit to generate s-curve error signal (implemented with algebra ICs(AD734, AD830), 2) achieve high enough gain in low frequency region (gain margin), and 3) provide phase shift at cross-over frequency (phase margin). A typical lead-lag circuit used to provide phase margin at the crossover frequency is shown in Figure 2.4.7

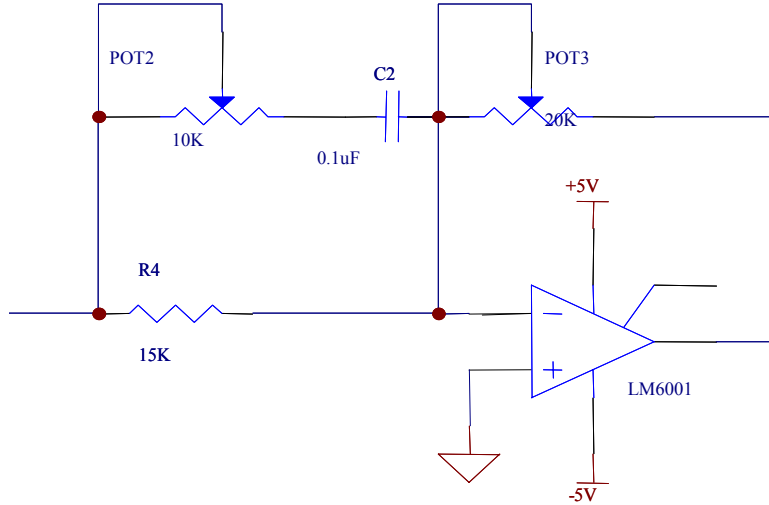


*Figure 2.4.7. Typical lead-lag circuit used for phase shift at crossover point*

#### 2.4.3.1 Experiment

To evaluate this T/F servo approach, the experimental system shown schematically in Figure 2.4.8 was constructed. A 635nm laser diode is split into two beams by a 50:50 beam splitter to form the two illumination spots required for the push-pull focus servo. The laser beams are then launched through two separate paths with a half-wave plates and beam expanders in each path. The half-wave plates are used to adjust the power levels of the illumination spots. The beam expanders are used to adjust the relative focal positions of the two illumination spots. The beam expanders may also be adjusted such that each spot is on a different layer leading to simultaneous readout of two-layers. The two beams are recombined by a polarizing beam splitter and reflected by a dichroic beam splitter, that reflects 635nm and transmits the fluorescence band (655nm-715nm, 685nm  $\lambda$  peak) into the CD objective lens voice-coil assembly. The objective lens forms two illumination spots that are controlled in lateral and longitudinal position by steering mirrors and the beam expanders. The illumination spots are placed upon data tracks, generating fluorescence that is collected by the objective lens and relayed by a magnification system to the detectors. The data bits in this experiment have dimensions  $1.5\mu\text{m}$ (radial)  $\times$   $1.5\mu\text{m}$ (in track)  $\times$   $15\mu\text{m}$ (in depth) that are recorded using the single beam two-photon recording architecture. The illumination power level for this experiment is  $\sim 300\mu\text{W}$  for each spot, and the fluorescence signal power level is nW level in this experiment. The disk is spinning on a servo controlled Design Sciences fluid bearing motor that has less than  $0.1\mu\text{m}$  repeatable runout. In the detection path, the first knife-edge prism separates the two imaged fluorescent spots by reflecting one fluorescent spot to detector #1 and allowing the other fluorescent spot to pass unobstructed to the second knife edge prism. The combination of the second knife edge prism with detector #2 and detector #3 behaves as a bi-cell detector. The effective gap width between the hybrid bi-cell detector elements is limited by the quality of the

knife edge that is measured to be  $\sim 2\mu\text{m}$ . This allows the use of other PMT detectors that are more compact than currently available quadrant PMT detectors such as the Hamamatsu R5900-00-M4 quadrant detectors that have a  $200\mu\text{m}$  element gap. The detectors being used at the moment are the Hamamatsu R7400U-02. Hi-sensitivity silicon detectors have been fabricated and will be used in future work. The induced fluorescent spot becomes an approximately uniform distribution in the pupil with no phase information recorded. The tracking control requires an imaging step after the pupil to relay the fluorescent spot/track image to the hybrid bi-cell tracking detector. The focus control does not require the imaging step as this only depends upon the power levels incident on the two detectors.

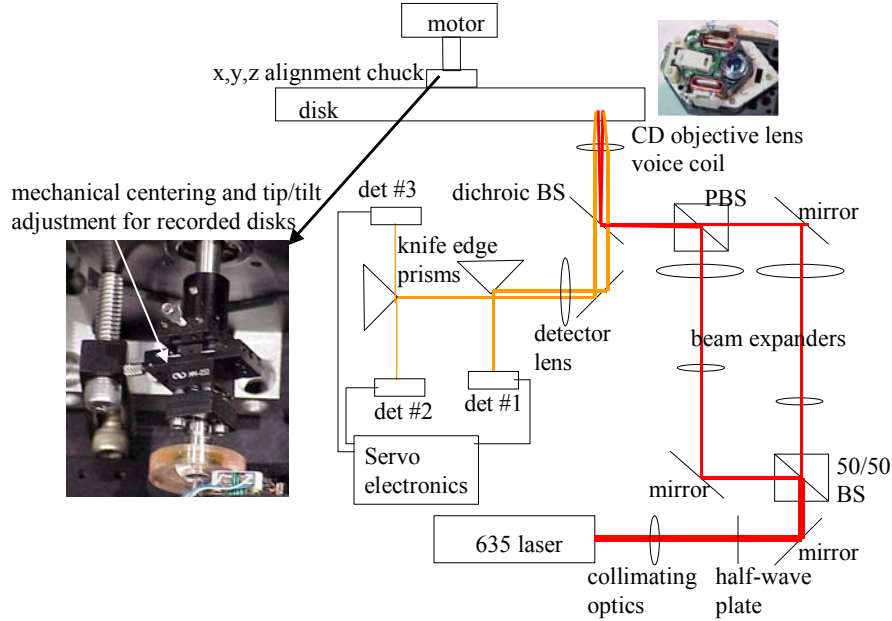


*Figure 2.4.8 Experimental system for testing push-pull focus and push-pull tracking with collinear illumination*

The inset of Figure 2.4.8 shows a coupling mechanical system between the disk and the motor shaft that allows tracks recorded on a different spindstand to be aligned to this spindstand's motor spindle. Using a straightforward alignment procedure the track eccentricity and disk wobble may be removed/minimized (within the motor runout), or a specified amount added. Insertion of specific amounts of eccentricity, wobble, and defocus enables the characterization of tracking and focus acquisition ranges and following errors.

Figure 2.4.9 (a) shows an experimental open loop focus error signal (FES), generated from two fluorescent spots that are on two separate tracks spaced  $\sim 80\mu\text{m}$  apart within the same layer. Experiments are currently underway where the FES is derived from not only two tracks separated radially, but also by  $\sim 100\mu\text{m}$  in depth. The oscilloscope trace closely resembles the predicted shape from Figure 2.4.5. There is modulation on the two peaks due to imperfect filtering of the data signal in the tracking servo electronics, however the effect of this data modulation on the FES is not significant as it is outside the bandwidth of the voice-coil actuator.

Preliminary tests with custom servo electronics (typical lead-lag circuits) showed that the control loop circuits closed on this FES waveform and are able to follow tracks with axial runouts of  $\sim 200\mu\text{m}$ . The disk is spinning at 20Hz at a radial location of 10mm on a 12.5mm radius disk. Figure 2.4.9(b) shows an experimental open loop tracking error signal (TES). The oscilloscope trace also closely resembles the predicted shape from Figure 2.4.5. Preliminary tests with custom servo electronics (typical lead-lag circuits) showed that the control loop circuits closed on this TES waveform and are able to follow tracks with radial runouts of  $\sim 20\mu\text{m}$ . The disk is spinning at 20Hz at a radial location of 10mm on a 12.5mm radius disk. Additional testing is currently underway.

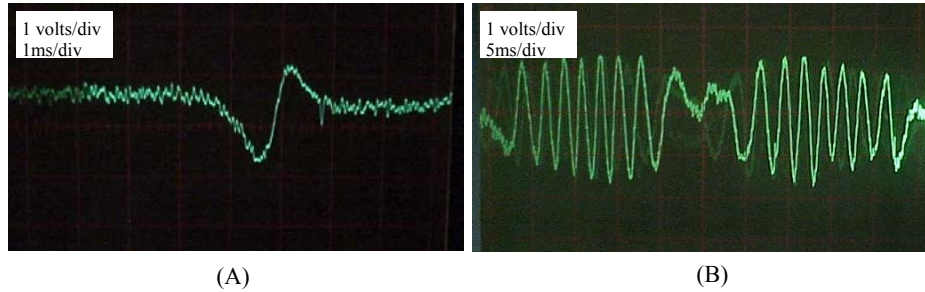


Figure 2.4.9 (a) Experimental focus error signal (FES) using collinear illumination, (b) Experimental tracking error signal (TES) using collinear illumination.

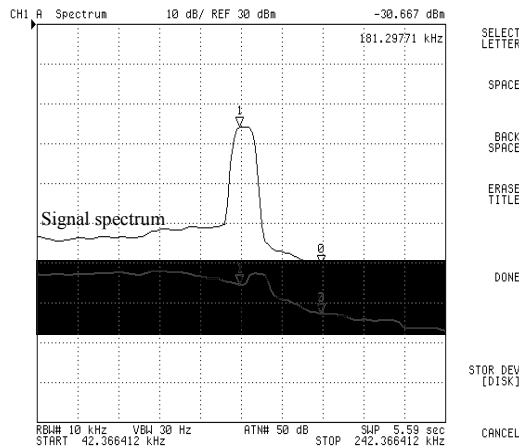
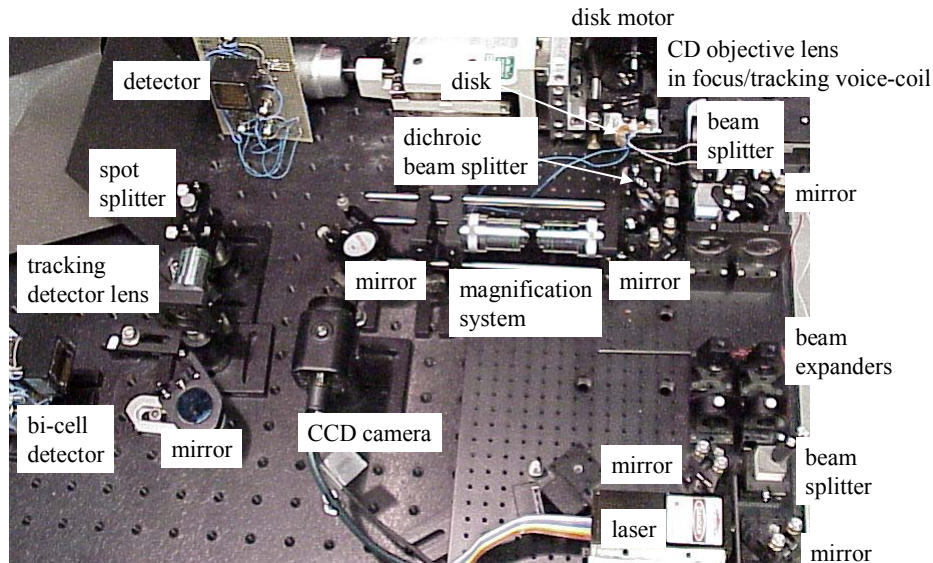


Figure 2.4.10. Carrier-to-noise-ratio (CNR) of about 35dB from a single tone data track with bit dimensions  $1.5\mu\text{m}(\text{radial}) \times 1.5\mu\text{m}(\text{in track}) \times 15\mu\text{m}(\text{in depth})$  with both tracking and focus servo loops closed, and the electronic noise floor of the transimpedance amplifier/detector combination with no light incident upon the detector.

Figure 2.4.10 shows the Carrier-to-noise-ratio (CNR) of a data track with the focus and tracking servos locked. The disk is spinning at 20Hz while the focus and tracking servos are locked on a single tone data track with bit dimensions of  $3.5\mu\text{m}(\text{radial}) \times 3.5\mu\text{m}(\text{in track}) \times 20\mu\text{m}(\text{in depth})$  at a radial location of 10mm on a 12.5mm radius disk. The electronic noise floor is observed to



be  $\sim 10$ db below the signal spectrum noise floor. The CNR is observed to be  $\sim 35$ dB. This signal is representative of the signal from either the sum of detector #2 and #3, or from detector #1. Figure 2.4.11 shows the experimental system for testing push-pull focus and push-pull tracking.



*Figure 2.4.11. Experimental system for testing push-pull focus and push-pull tracking.*

### 2.4.3.2 Experimental collinear tracking servo characterization

The goal of the servo is to keep the illumination beam and the collection optics focused and centered on a recorded data vector by generating an appropriate error signal that is then processed by a control algorithm for feedback to an actuated element. Other servo tasks include layer/track addressing, and spindle speed control.

A coupling mechanical system between the disk and the motor shaft that allows track eccentricity and disk wobble to be removed/minimized (within the motor runout), or a specified amount added is used to experimentally characterize the tracking servo. Insertion of specific amounts of eccentricity enables the characterization of tracking acquisition ranges. Figure 2.4.12 shows a plot of the spindle speed versus the tracking eccentricity at which the tracking servo can successfully follow a track. Below the line the tracking loop can close successfully and follow a track with a given eccentricity and spindle speed. Above the line the tracking loop cannot be closed.

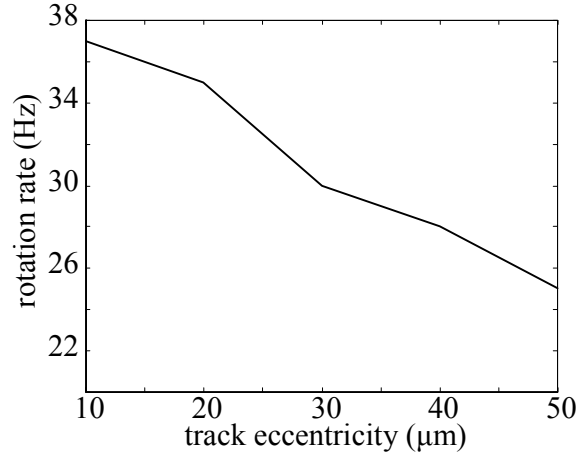


*Figure 2.4.12. Experimentally obtained tracking servo loop limit. Below the line the tracking loop can close successfully and follow a track with a given eccentricity and spindle speed. Above the line the tracking loop cannot be closed.*

Closed-loop focus and tracking control using fluorescent signal power is demonstrated on 2-photon recorded data tracks. This is the first demonstration, to the authors' knowledge, of an operational focus and tracking servo in 2-photon recorded media, or in a monolithic photochromic disk in general. The disk does not need to be preformatted as in a sampled servo approach, or the data layers do not need any special groove structures.

#### **2.4.4 Spindle rotation speed**

Another parameter to be actuated is the rotation speed of the spindle. It is desirable to use constant linear velocity (CLV) (where the spindle rotation speed is varied in order to keep the linear velocity constant at different disk radii) because the storage capacity of a CLV disk is greater than a constant angular velocity (CAV) disk <sup>21</sup>. However, CLV typically has slower access times than CAV, due to lower rotation rates.

Keeping the linear velocity constant can be understood from equation 1

$$v = r\omega = 2\pi df_{\text{data}} \quad (1)$$

Where  $v$  is the linear velocity,  $r$  is the disk radius,  $\omega$  is the angular velocity and  $\omega=2\pi f_{\text{spindle}}$  where  $f_{\text{spindle}}$  is the spindle frequency,  $d$  is the mark size and  $f_{\text{data}}$  is the desired data rate for this mark size.

Now consider an example of how the spindle speed will change from an inner radius of 10mm to an outer radius of 44mm with a 2μm mark at a data rate of 4Mbit/s for 1 serial channel. The velocity  $v = 16\text{m/s}$  for this data rate and mark size. At the 10mm radius the spindle frequency is



$f_{\text{spindle}} = 254\text{Hz}$  or a rotation rate of 15240 RPM and at the outer radius of 44mm the spindle frequency is  $f_{\text{spindle}} = 58\text{Hz}$  or a rotation rate of 3472 RPM.

The system may also be formatted in a zoned CAV fashion where the linear velocity is a constant for certain annular regions of the disk. A zoned CAV is a compromise between storage capacity and access time.

#### **2.4.5 Readout addressing system.**

One way to address layers within the disk is to move the entire lens and detector assembly in depth. This is unattractive since it is more practical to leave the detector and recording/readout optical head fixed. Moving the objective lens only while leaving the remaining elements fixed for layer addressing introduces complications into the optical system design. A solution for the addressing question is to move the spindle motor stage by motorized stages radially and longitudinally for radial and depth access. This is chosen to allow the flexibility of interchanging optical head components as needed on a prototype bench format.

#### **2.4.6 Spindle Selection**

Spindle motors have different relevant specifications that can impact the Servo systems under development. For instance, the repeatable run-out and non-repeatable run-out specifications will influence the final spindle choice.

The repeatable run-out specification of a motor describes the non-circular rotational motion of the motor shaft. Ideally this is zero, and for high-end spindles such as air bearing motors and fluid bearing motors this is specified to be  $<0.1\mu\text{m}$ . Lower-end motors, such as ball-bearing motors, or dc brushless motors may specify this to be a few  $\mu\text{m}$ 's to 10's of  $\mu\text{m}$ 's. We have developed the capability to qualify the motors that we purchase by observing the path that a point on the mechanical motor shaft traces out under a calibrated microscope. The air bearing motor had no measurable run-out while DIH28-25-TBD BEI ball bearing motor has  $\pm 10\mu\text{m}$  of repeatable run-out and DIS14-20-001z-9946 BEI ball bearing motor has  $\pm 5\mu\text{m}$  of repeatable run-out

The non-repeatable run-out of a motor describes the high frequency variations of the motor shaft along the repeatable motion of the shaft. This non-repeatable run-out is sub-micron for all of the spindles being considered.

The nominal tracking range for the servo system and the tracking and focus servo bandwidth will be dominated by the motor run-out, along with any de-centering introduced when mounting and remounting disks. For all servo experiments and tabletop system demonstrations either the air bearing spindle or fluid bearing spindle is used due to their superior mechanical properties.

### 2.4.7 Servo while writing architecture

A technique to servo while recording is now presented. The servo while reading data tracks, as described above, is extended to include recording also. Initially there are no tracks recorded inside the disk. The focus addressing system finds the front surface of the disk and then moves in to the initial recording depth of  $\sim 250\mu\text{m}$  inside the disk. A servo or data track is initially recorded open loop at the inner radius of the disk at this first depth. Layer and track information is encoded into the data track.

Figure 2.4.13 shows a top view of the disk indicating the first recorded track. The writing and reading lasers are separated laterally by one track width inside the disk. The radial addressing of the disk now moves one track so that the read laser is now above the newly recorded track. The read laser locks servo on this track, then the write laser records on the adjacent track while the read laser is locked servo on the adjacent track. The read laser then locks on new recorded data track and this is repeated for a few hundred tracks or until error propagation after so many removals from drive requires the recording of a new unlocked servo recording. This recording of new dedicated servo tracks at radial zones and at different layers helps to minimize error propagation in unformatted removable media. This technique requires no real need to pre-format entire disk except for initial servo track and subsequent radial and layer zones.

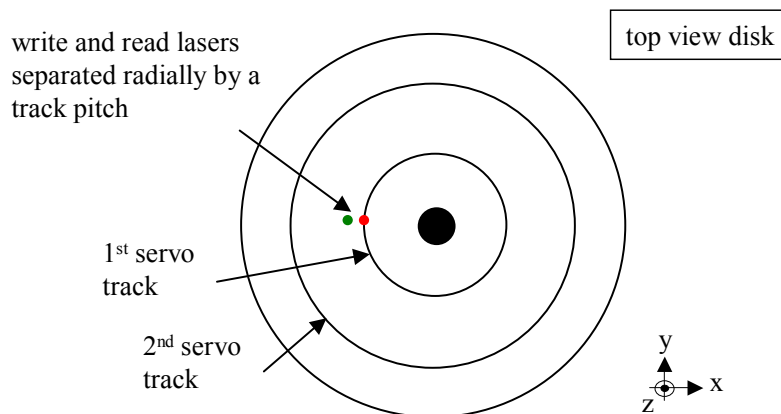


*Figure 2.4.13. Top view of disk showing servo tracks and write and read lasers separated radially by one track pitch.*

### Summary of accomplishments

- Closed-loop focus and tracking control developed for two-photon media.
- Closed-loop focus and tracking control optimized and can follow focus and tracking runouts up to  $30\mu\text{m}$  at spindle speed of 30Hz with following accuracies better than  $0.5\mu\text{m}$
- Servo extended to parallel format
- No pre-formatting of media required
- Illumination and recording servo developed.

### 3 WORM DEMONSTRATOR

---

#### 3.1 Worm portable readout system

A spinning disk readout system was designed with the following goals in mind:

- Provide a volumetric optical disk readout system integrating subsystems (optics, lasers, detectors, motors, channel and control electronics, user interface),
- Provide as fast a readout speed as possible
- Store as much data as practical.
- Use low risk components.
- Package the system in a box so it can be shipped.



*Figure 3.1.1 Fully assembled system with laptop computer interface.*

The result of work on this system is shown in Figure 3.1.1, where the optics, optomechanics, motors, and electronics are housed in a 24" x18"x15" box, with laptop computer providing the graphical user interface and displaying the decoded imagery read from the disk.

##### 3.1.1 Optical system

The optics, optomechanics, and motors are assembled on a compact optical bench within the box, under and around which are placed the 25 electronic circuit boards and power supplies. This optical bench and the various light paths are shown in Figure 3.1.2. A 635nm laser diode is split into 16 beams by a diffractive optical element (doe). The sixteen beams are eventually focused by the objective lens to illuminate sixteen tracks within a data layer. The dichroic beam splitter

reflects the sixteen 635nm beams and transmits the fluorescent wavelength band (peaked at 685nm). The objective lens thus forms sixteen illumination spots that are controlled in lateral and longitudinal position by steering mirrors and a beam expander. When the illumination spots are placed upon data tracks, data marks generate fluorescence that is collected by the objective lens and relayed by a magnification system to the detectors. The disk is spinning on a Design Sciences Inc. fluid bearing motor. On the way to the detectors the 16 imaged fluorescent spots are magnified to match the pmt 1mm detector pitch.

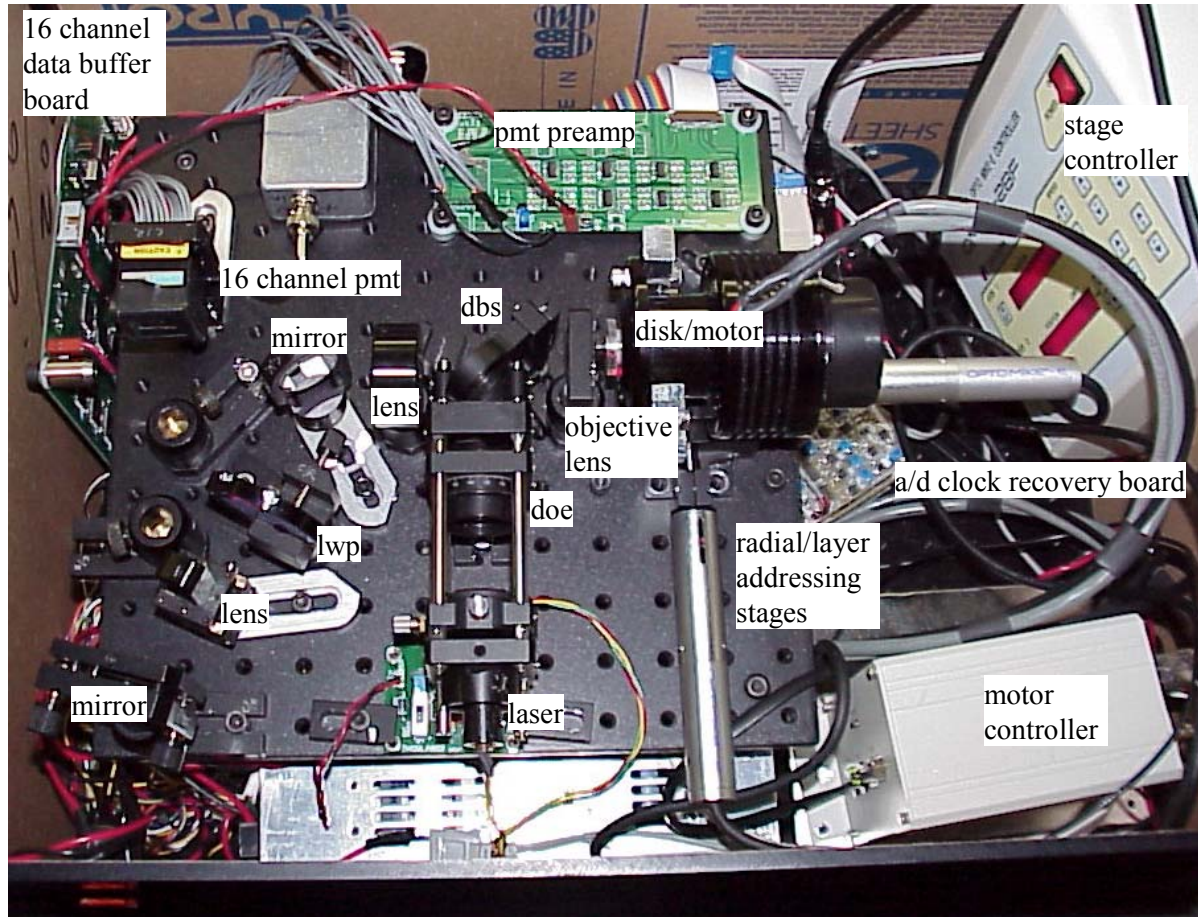


*Figure 3.1.2 Photograph of the optical bench with illumination and readout paths.*

Figure 3.1.3(a) shows the mechanism of the collinear point-by-point illumination module that uses a diffractive grating to split a collimated input beam into a  $1 \times 16$  array of beams having approximately equal power and different transmission angles. These beams are focused by the objective lens inside the disk generating 16 illumination spots. A high degree of uniformity of optical quality among all the focused spots is achieved for keeping the readout characteristics as uniform as possible. The spot pitch is determined by both parameters of the grating and the focal length of the objective lens. In the experiment, a diffractive grating (Thorlabs G100K  $1 \times 16$  fanout) and a high NA aspheric lens (Geltech 350240 8mm focal length) are used to generate a  $1 \times 16$  spot array with  $10\mu\text{m}$  pitch.

A parallel readout system based on a PMT array (Hamamatsu 1×16 channels, 1mm pitch) is realized. A telescope in the illumination system provides for spot pitch adjustment by moving the diffraction grating axially in the converging or diverging beam, as shown in **Figure 3.1.4**. The 2× magnification matches the 4mm collimated beam from the laser (Blue Sky Versalase laser module) to the 8mm diameter of the objective lens (Geltech 350240 0.5NA).

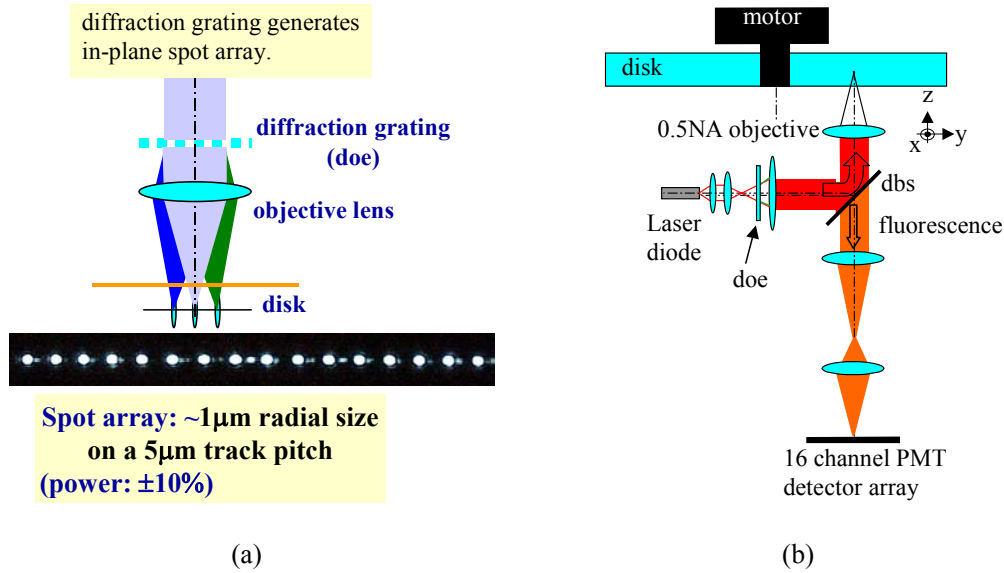


Figure 3.1.3(a) Schematic drawing of in-plane parallel illumination showing experimental CCD image of 1 x 16 illumination spot array (b) schematic of experimental system of Figure 3.1.2 parallel readout system based on in-plane illumination and a PMT array

Next the data tracks are imaged to match the pitch of the PMT array. The pitch of the 1 x 16 channel parallel PMT array (Hamamatsu) in the experiment is 1mm. The pitch of the data bits is 10 μm requiring a 100× magnification. The 100X magnification is split into 2 imaging steps. With a magnification  $m_1$  obtained at the focal plane of the first imaging lens. The second imaging lens provides another magnification of  $m_2$ .  $m_1$  and  $m_2$  are 2 and 50 respectively resulting in a net magnification of 100.

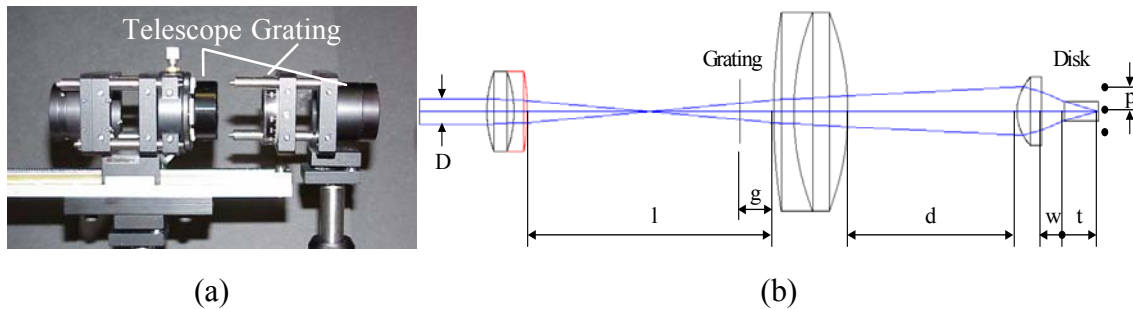
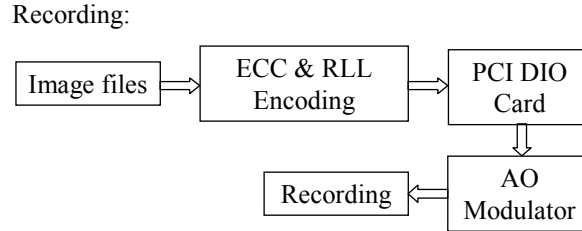


Figure 3.1.4 (a) In-plane illumination module and (b) its schematic drawing

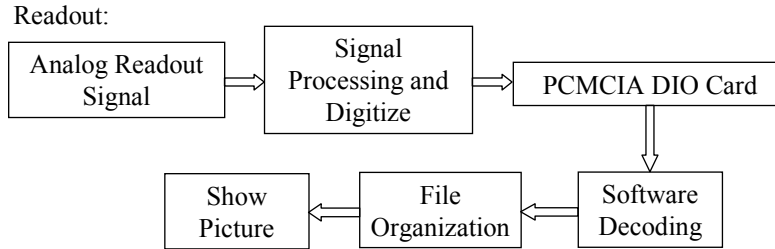


Figure 3.1.4 shows the illumination module and its schematic drawing. The diffractive grating (MEMS Optical G100K) is placed in the divergent or convergent beam path between the two lenses of the telescope.

### 3.1.2 Disk format



**Figure 3.1.5** Flowchart of data formatting during recording.



**Figure 3.1.6.** Flowchart of data formatting during readout.

The 23 mm diameter by 6 mm thick disk stores 12 JPEG encoded images, formatted as 1 data layer, containing 192 concentric data tracks. The track pitch is 10  $\mu\text{m}$ . To eliminate the need for a tracking servo, the disks are recorded and readout on the same fluid bearing motor spindle without removal of disk, and the track width is increased to 3  $\mu\text{m}$  to accommodate any repeatable lateral runout that may be introduced by mechanical drift of the disk mount, and seek motor errors. Each track contains 16384 bits of raw pulse position modulated (PPM) data. In addition to the user data, these 16384 bits/track are used for sector addressing information, synchronization and clock recovery, (2,7) data run-length limited (RLL) encoding, and Reed-Solomon error correction encoding (ECC). The level of RS code we adopted is (15,9) with a symbol length of 4 bits. Within every 15 symbols (4 bits each symbol), 3 symbol errors may be corrected. A flow chart of the data formatting is shown in Figure 3.1.5 and Figure 3.1.6. Each of the 12 jpeg images is stored in a group of sixteen tracks as shown in Figure 3.17(a). Figure 3.17 (a) is a confocal microscope image of recorded data. Figure 3.17(b) shows the resultant loss of data recorded at a depth of 0.7mm inside the disk due to a surface defect on the disk surface. If such an error exists as in (b) the image will not be successfully decoded due to the size of the error (well over 100microns).

### 3.1.3 Spindle and seek control

To read the data, the disk spins at 360RPM and sixteen 100kb/s data streams are generated. The

spindle servo control circuit box, shown in Figure 3.1.2, controls the rotation rate of the spindle. The disk /motor assembly are mounted on a radial access stage, and to seek from one track to the next, the stage is moved while the signal level is monitored by a custom track seek control board. When the edge of the next track is detected, the stage is stepped to the center of the track by signals generated from this board in conjunction with monitoring software running on the laptop.

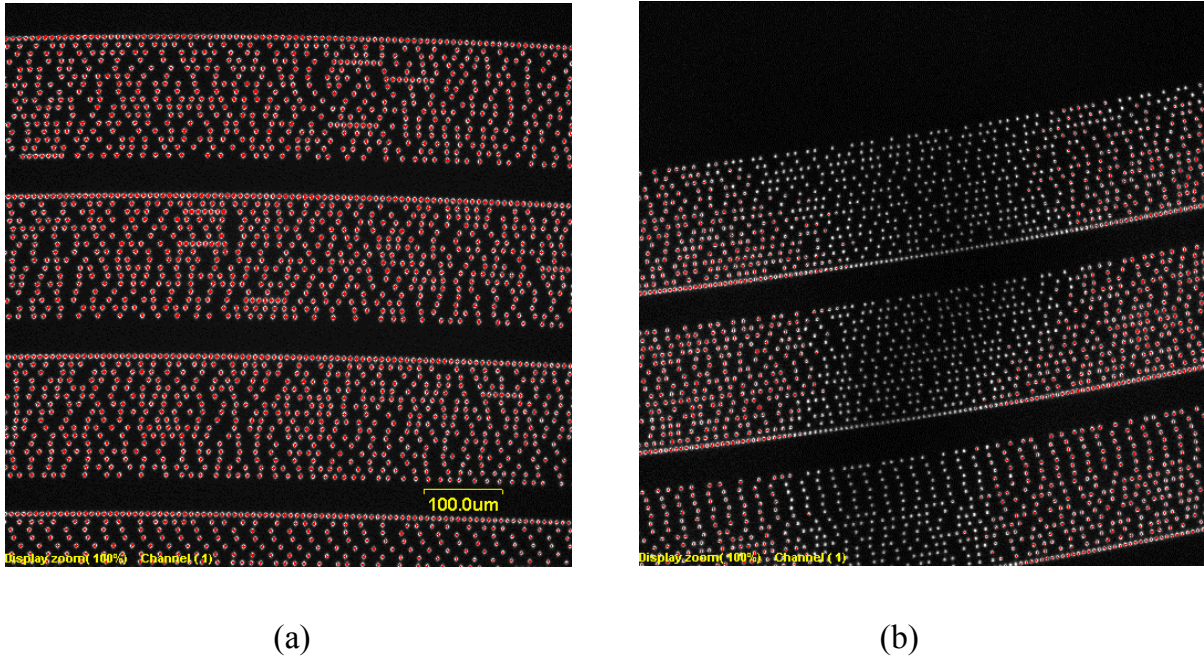


*Figure 3.1.7. confocal microscope images (a) shows 3 groups of 16 data tracks where each group of sixteen contains one of the jpeg images to be displayed, (b) shows the effect of a surface defect on the disk (such as a scratch) and the resultant loss of data.*

### **3.1.4 Read channel signal processing**

The read channel electronics of the custom 16 read-channel circuit boards have the following structure. The analog waveforms from the PMT detectors are amplified and low-pass filtered and then fed to a peak detection circuit. The TTL signal from the peak detection output is fed to clock extraction circuitry. The peak detection decision circuit uses a differentiator, automatic gain control (AGC), level comparators, and a one-shot circuit. The differentiator is active 2nd order band-pass filter using a single opamp. The AGC removes the amplitude variation (or the envelop) of the differentiated signal. The level comparators do zero-crossing detection of the differentiated signal, which corresponds to the peak signal level of the original signal from the PMT. In addition, the comparators define the window of time interval during which the zero-crossing detection is valid. The one-shot circuit is used to adjust the duty cycle of the data so that the “ON” duty cycle matches center of the operating range of the clock extraction circuit.

To accurately decode the pulse-position modulated data stream, a clock signal that is precisely phase-matched to the data (even in the presence of residual rotational speed variations) is needed. The clock extraction circuit takes the TTL level output from the peak detector and outputs a clock signal that is phase-locked to the data. The period of the clock corresponds to the “ON” duty cycle of the data signal and the up transition of the clock signal falls approximately in the middle of it. The phase-locked loop circuit has VCO, phase comparator and a loop filter. The loop filter is set so that it can handle the range of frequency components contained in a 2,7 encoded data signal. Finally, the clock and the data signal are buffered (low impedance out) and sent to the laptop computer by a National Instruments Digital Interface PC card. The modulation decoding, de-interlacing, error correction decoding, and JPEG file reassembly and display operations are performed by custom software running under the LabView graphical user interface control/display process window.

### ***3.1.5 Lessons learned***

Each image takes ~ 15 seconds to be displayed. The majority of time is spent in two areas. The first 6 seconds is spent in radial addressing to the track group. The next 7 seconds is spent in bringing the data from the data buffer board into the computer. The remaining couple of seconds is spent in decoding/ecc and display of image. Using a faster stage controller and faster lead screw could make the 6 seconds in radial addressing faster. Adding a tracking servo would also allow faster radial access time along with improved stage motor controller and improved system reliability. The 7 seconds in bringing the data from the buffer to the computer could be made faster by using a desktop where a desktop labview dio card will not limit the data input speed and the full 1Mb/s channel readout speed would be realized as in our table top demos. Hardware decoding vs software decoding would not be that noticeable of an improvement at this time. Media defects need to be improved in order to increase reliability. Also a new media needs to be developed that is suitable for mass manufacture capability that can withstand the injection molding environment. At 1Mb/s the recording speed is still too slow due to suitable laser availability and the two-photon absorption cross-section.

## ***References***

---

<sup>1</sup> H. Zhang, A.S. Dvornikov, E.P. Walker, N.H. Kim, F.B. McCormick, “Single-beam two-photon-recorded monolithic multi-layer optical disks,” ODS 2000 Proc. SPIE 4090 pp. 174-178 (2000).

<sup>2</sup> Milonni, Peter W., Eberly, Joseph H. Eberly, “Lasers” , (Wiley), p. 680, 1988.

<sup>3</sup> D.A. Parthenopoulos and P.M. Rentzepis, Science 245, 843 (1989)

<sup>4</sup> F. B. McCormick, I. Cokgor, S. C. Esener , A. S. Dvornikov, and P. M. Rentzepis, “Two-photon absorption-based 3-D optical memories,” in High Density Data Recording and Retrieval Technologies, Ted A Schwartz, Martin Francis, Editors, Proc. SPIE 2604, 23-32 (1996).



- 
- <sup>5</sup> Haichuan Zhang, Frederick B. McCormick, Alexander S. Dvornikov, Curtis Chapman, Edwin P. Walker, Nam-Hyong Kim, "Single-beam two-photon-recorded monolithic multi-layer optical disks," in ODS 2000, Douglas G. Stinson, Ryuichi Katayama, Editors, Proc. SPIE 4090, 174-178 (2000).
- <sup>6</sup> Tom D. Milster, Robert S. Upton, and Hui Luo, "Objective lens design for multiple-layer optical data storage," Opt. Eng. **38** (2) 295-30
- <sup>7</sup> Welford, Walter T. "Aberration of optical systems", (Adam Hilger Ltd.), 1986
- <sup>8</sup> T. D. Milster, "A user-friendly diffraction modeling program", ODS Topical Meeting Conference Digest, Apr. 7-9, 1997, pp.60-61.
- <sup>9</sup> D. E. Pansatiankul, A. A. Sawchuk, "Multi-dimensional modulation codes and error correction for page-oriented optical data storage", ODS Topical Meeting Conference Digest, Apr. 22-25, 2001, pp.94-96.
- <sup>10</sup> E.P. Walker, X Zheng, F.B. McCormick, H. Zhang, N.H. Kim, J Costa, A.S. Dvornikov, "Servo error signal generation for 2-photon recorded monolithic multilayer optical data storage," ODS 2000 Proc. SPIE 4090 pp. 179-184 (2000).
- <sup>11</sup> E.P. Walker, J Duparre, H. Zhang, W Feng, Y. Zhang, A.S. Dvornikov, "Spherical aberration correction for 2-photon recorded monolithic multilayer optical data storage," ODS 2001 Proc. SPIE. (2001).
- <sup>12</sup> W. Feng, E.P Walker, Haichuan Zhang, Yi Zhang, A. Dvornikov, S. Esener, "Top illuminator design for 2-D parallel readout in a 3-D multilayer optical data storage system," Proceeding of SPIE, vol. 4459, pp. 334~343, 2001.
- <sup>13</sup> J. Dovic, J. Wals, T. Ikkink, T. Tukker, M. Rieck, J. V. D. Eerenbeemd, A. L. V. Voorst and R. Rijs, "Multi-track DVD-ROM," in ODS 2001, pp. 112~114, 2001.
- <sup>14</sup> T. Maeda and H. Koyanagi, "Semiconfocal optical disk readout with one linear-spread beam," *Applied Optics*, **37**(35), pp. 8167~8172, 1998.
- <sup>15</sup> J. M. Sasian and M. Mansuripur, "Design approaches with a lenslet array and a single, high-numerical-aperture annular-field objective lens for optical data storage systems that incorporate large numbers of parallel read-write-erase channels," *Applied Optics*, **38**(7), pp. 1663~1168, 1999.
- <sup>16</sup> E. P. Walker, W. Feng, Y. Zhang, H. Zhang, F. B. McCormick, S. Esener, "3d parallel readout in a 3d multilayer optical data storage system," ISOM/ODS meeting Hawaii (2002) paper # TuB 4.
- <sup>17</sup> Esener, Sadik C., Rentzepis, Peter M., "Two-Photon, 3-D memories," Final Technical Report AFRL-IF-RS-TR-1999-1, p.56-57.
- <sup>18</sup> F. B. McCormick, I. Cokgor, S. C. Esener, A. S. Dvornikov, and P. M. Rentzepis, "Two-photon absorption-based 3-D optical memories," in High Density Data Recording and Retrieval Technologies, Ted A Schwartz, Martin Francis, Editors, Proc. SPIE 2604, 23-32 (1996).
- <sup>5</sup> M. M. Wang, S. C. Esener, F. B. McCormick, I. Cokgor, A. S. Dvornikov, P. M. Rentzepis, "Experimental characterization of a two-photon memory," Optics Letters 22 (8), pp. 558-560, (1997).
- <sup>7</sup> G. Bouwhuis, J. Braat, A. Huijser, J. Pasman, A. Huijser, J. Pasman, G. Van Rosmalen, and K.S. Immink, "Principles of Optical Disk Systems," Adam Higler, Bristol and Boston (1985).
- <sup>21</sup> A.B. Marchant, *Optical Recording: A Technical Overview*, (Academic Press, USA, 1987), Chap. 10.